Stress-State Dependent Fracture Prediction

An Application in Numerical Analysis of Maritime Collision

by

F.W. Bijleveld

A thesis submitted to

Delft University of Technology

in Partial Fulfillment of the Requirements for the Degree of

Master of Science

in

Offshore Engineering

To be defended in public on

March 5, 2018

Supervisor:	prof. dr. ir.	M.L. Kaminski	TU Delft
Thesis committee:	ir.	R.W. Bos	TU Delft
	dr. ir.	P.T.L.M. van Woerkom	TU Delft
	dr. ir.	M. Janssen	TU Delft
	ir.	M.G. Hoogeland	TNO

innovation for life

Abstract

In the past decades the understanding of fracture of ductile material has increased substantially. Research has shown that the onset of fracture highly depends on the full state of stress inside the material. Better understanding of fracture resulted in more advanced and complex *fracture models* being conceived, allowing researchers to predict fracture in ductile solids with improved accuracy.

Nonlinear finite element analysis is a powerful tool at the disposal of researchers to predict the response of ship and offshore structures. When it comes to simulating accidental loads, such as collisions, often basic criteria are applied to include fracture in a finite element model. However, accurate fracture prediction is of great importance to determine the ice resilience of vessels, or to obtain reliable estimates of the sustained damage due to maritime collision. This research focuses on the latter.

This thesis is concerned with bridging the gap between the recent developments in fracture prediction and the application of failure criteria in finite element analysis of ship collision. A selection of recently published fracture models has been made and experiments have been conducted on S235 structural steel for calibration and validation of these models. Four small scale experiments have been conducted. These experiments serve a dual purpose: first, to gather information on the material behaviour during deformation. Second, to obtain information on the effect of different stress conditions on fracture. An iterative method has been employed to accurately model the material behaviour. For the calibration of the fracture models a method has been conceived and applied that takes into account the full histories of stress and strain during the deformation process up to fracture.

Before application as failure criteria for finite elements, the calibrated fracture models require a correction based on the size of the elements: a modification to an already existing theoretical framework has been proposed and applied to obtain element-size dependent failure criteria.

A large scale drop tower experiment has been designed to simulate a so called raking damage scenario. This experiment has been conducted on the same material as the small scale experiments and serves as a validation for a finite element model that has been created using the information on the material behaviour obtained from the small scale experiments. The different failure criteria have been implemented into the commercial finite element package LS-DYNA and have been applied to the finite element model. The results have been compared to the results of the raking damage experiment.

It was concluded that the application of complex multi-parameter failure models in analysis of maritime collision does not necessarily provide an improvement over conventional fracture prediction methods. The inability of shell elements to accurately describe strain concentrations and the effect of the element size introduce uncertainties that overrule the benefits of stress-state dependent prediction of element failure.

Preface

In front of you lies the thesis *Stress-State Dependent Fracture Prediction - An Application in Numerical Analysis of Maritime Collision* by Floriaan Bijleveld. This thesis was written in partial fulfillment of the requirements to obtain the degree of Master of Science in the field of Offshore Engineering at Delft University of Technology. The project was realized in cooperation with the Structural Dynamics department of the Dutch organization for applied scientific research, TNO.

First and foremost, I would like to thank my supervisors at TNO, Martijn Hoogeland and Carey Walters, without whom realization of this Masters thesis would not have been possible. My wholehearted thanks for investing so much time in me and for continuously sharing knowledge with me during my graduation process. Carey's theoretical knowledge and Martijn's more practical approach have aided me beyond words.

Secondly, I would like to express my thanks to both Mirek Kaminski, professor of Ship & Offshore Structures, and Reinier Bos, my daily supervisor at the TU. Both of whom truly inspired me during my Master of Science, encouraging me and leading me to this graduation project. Furthermore I am very grateful for their enthusiasm and constructive feedback during our meetings. This definitely contributed to making my graduation process a pleasant experience. I would also like to thank Michael Janssen and Paul van Woerkom for their efforts as members of my thesis committee and for investing their time to aid me in improving my thesis.

Furthermore, I am grateful to the colleagues and fellow interns at TNO for their cooperative attitude and the many informative and enjoyable conversations we had. And to my friends and roommates, for always being prepared to provide me with necessary distractions under the enjoyment of coffee, lunch or drinks.

Last, but not least, I thank my family for their continued support during my studies, having faith in me and encouraging me to achieve what I came to Delft for.

Due to the contributions of all previously mentioned persons, I could not possibly have wished for a more pleasant and informative graduation project.

Floriaan Bijleveld
Delft, February 2018

Contents

Nomenclature

Abbreviations

BWH	Bressan-Williams-Hill
CEFS	Constant Equivalent Failure Strain
DIC	Digital Image Correlation
EFS	Equivalent plastic Failure Strain
EPS	Equivalent Plastic Strain
FEA	Finite Element Analysis
FEM	Finite Element Method
FLD	Forming Limit Diagram
JC	Johnson-Cook
MK	Marciniak-Kuczynski
MMC	Modified Mohr-Coulomb
TNO	Netherlands Organisation for Applied Scientific Research
VLPC	Variable Load Path Calibration
VNGC	Void Nucleation, Growth & Coalescence

Greek symbols

α	True strain ratio $\frac{\varepsilon_2}{\varepsilon_1}$ (-)
β	Principal stress ratio $\frac{\sigma_2}{\sigma_1}$ (-)
ε	True strain (-)
$\varepsilon_1, \varepsilon_2, \varepsilon_3$	Plastic principal strains (-)
ε_e	Elastic true strain (-)
ε_p	Plastic true strain (-)

$\bar{\varepsilon}_F$	Equivalent plastic strain at fracture (-)
$\bar{\varepsilon}_f$	Equivalent plastic strain at failure (-)
$\bar{\varepsilon}_N$	Equivalent plastic strain at necking (-)
$\bar{\varepsilon}_p$	Equivalent plastic strain (-)
$\dot{\varepsilon}$	Strain rate (s^{-1})
η	Stress triaxiality (-)
γ	Failure locus scaling factor
σ	True stress (MPa)
$\sigma_1, \sigma_2, \sigma_3$	Principal stresses (MPa)
σ_m	Mean (hydrostatic) stress (MPa)
$\bar{\sigma}$	Equivalent Von Mises stress (MPa)
$\bar{\sigma}_F$	Equivalent Von Mises stress at fracture (MPa)
θ	Lode angle (rad)
$\bar{\theta}$	Lode parameter (-)
ξ	Normalized third invariant (-)

Latin symbols

D	Damage parameter (-)
E	Young's Modulus (GPa)
e	Engineering strain (-)
g	Gravitational acceleration (m s^{-2})
$[I]$	Identity Matrix
s_1, s_2, s_3	Principal deviatoric stress (MPa)

Chapter 1

Introduction

1.1 Motivation

As our understanding of mechanics progresses and computational resources increase over time, so does our interest in being able to predict fracture. Fracture is an important aspect, not only in the event of ship collision, but also in our everyday lives. Often fracture is associated with undesirable events, such as vehicular crashes and breaking objects. However, fracture may also often be a desired effect, for example in the event of opening a tin can or cutting paper.

In the light of the present work, fracture carries a negative connotation as it associated with the ultimate state beyond which the ship or offshore structure is critically damaged. At best, the loss of structural integrity due to fracture may affect the functionality of the vessel. At worst, the vessel, its cargo, and even lives may be lost due to fracture as a result of maritime crash, possibly also endangering the environment.

Up to this day vessels still perish as a result of collision with another vessel or by grounding. Recent examples of these events are the collision of the USS John S. McCain, a destroyer in the United States navy, with the Alnic MC, a Liberian oil tanker. In this event, which occurred on the 21st of August 2017 just off the coast of Singapore, ten lives of US sailors were lost, while the structure sustained severe damage (Fig. 1.1). On the 13th of January 2012, the cruise ship Costa Concordia collided with a submerged rock off the coast of Italy. Subsequently, the vessel capsized and sank (Fig. 1.2), resulting in the death of 32 passengers.

Unfortunately, accurate fracture prediction could neither have saved the victims, nor avoided these maritime crashes. However, improved fracture prediction might prove beneficial for engineers in the design of a vessel: A better prediction of fracture produces better estimates of the damage sustained in the event of collision and is therefore an invaluable in the analysis of the crashworthiness of vessels.

In the design process of ships and offshore vessels, the Finite Element Method

Figure 1.1: USS John S. McCain after collision with Alnic MC

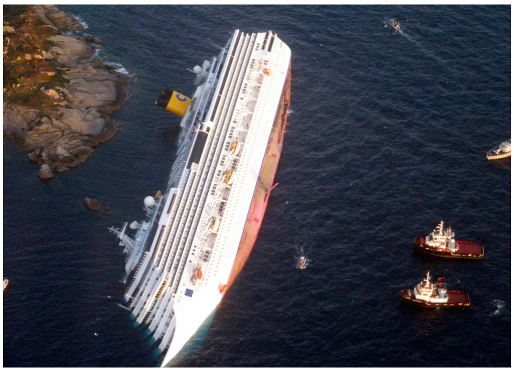

Figure 1.2: Costa Concordia capsized after suffering from severe grounding damage

(FEM) is an advanced and therefore invaluable tool at the disposal of present-day engineers. Normally these finite element analyses are performed implicitly in the linear-elastic domain. When it comes to simulating collisions using a finite element analysis, plasticity is to be dealt with, while using explicit time-integration. Typically, naval engineers are only interested in the ship's structural response to ordinary wave loads, and therefore do not require the latter approach. However, several specialists, research bureaus and classification agencies are interested in the crashworthiness of ships. When it comes to simulating collisions using a finite element model, often very basic fracture criteria are applied. As a result the effect of the state of stress inside the material on ductile fracture is ignored. Research has shown that ductile fracture is highly affected by the state of stress within the material (Rice and Tracey [1969]) and therefore the engineering approach is inherently deficient. Many models for the prediction of fracture that do account for the state of stress have been developed in the past few decades, however these are rarely used in ship collision analysis. Generally the increase in predictive capabilities of these *failure models* comes at the expense of the convenience using them: the increased required effort to use these models is preventing their application. However, accurate prediction of fracture is of vital importance for obtaining proper estimates of the amount of damage that is sustained in the event of ship collision.

1.2 Scope

Ship structures are typically large assemblies of components made of structural steel. These components two purposes that contribute to the serviceability of the vessel: structural components providing the strength of the structure or plate components providing both strength and the watertight shell that allows the vessel to float. In the event of a ship collision damage may be sustained to the components in both categories. Damage to the strengthening components has a potentially deteriorating effect on the vessel's structural integrity and serviceability. Failure of structural components does not necessarily result in the perishing of the vessel. Failure of the watertight shell, however, is far more critical: fracture in the ship's plating allows water to freely access the structure, resulting in flooding, and even potential instability or sinking of the ship. Finding a fracture-prediction method for fracture in the ships plating is therefore the main focus in this research.

The shell that causes the vessel's structure to be watertight consists of large structural steel plating, with typical lengths that far exceed the thickness of the plate material. When finite-element models are used in the design stage of vessels, the obvious choice is to use shell elements to model the ships plating due to their large computational advantage over solid elements. Typically, these models are extensive, therefore shell element side lengths far exceed their thicknesses to reduce the amount of required elements thus keeping the computational time at a minimum. However, fracture is a local phenomenon that cannot be accurately captured by large shell elements. Therefore an important prerequisite is that a fracture-prediction method is sought after, which bridges this inherent deficiency.

The type of structural steel that is commonly used in the proximity of the waterline of the vessel is mild steel, which shows ductile behavior, meaning that fracture is preceded by a large plastic deformations. However, the amount of plastic deformation up to fracture highly depends on the state of stress inside the material induced by the loading conditions. In the event of ship collision, the plating of the ship is dented inwards. During the indentation process the plating experiences bending deformation superseded by in-plane deformation due to the out-of-plane loading. The first causes compressive stress in the indented side of the plate and tensile stress at the opposite side. The latter causes high in-plane tensile stresses. As the plastic deformation progresses the bending stresses becomes negligible compared to the in-plane tensile stresses: the size of the indenter, i.e. the striking ship, rock, or iceberg, is far greater than the thickness of the plating. As a result, the stresses in the material up to fracture are dominated by tension in the plane of the plating. Therefore a fracture-prediction method is required that is applicable as a failure criterion in the finite element method to predict failure of shell elements, preceded by plastic deformation in tensile stress conditions.

In this thesis, the term *fracture* is related to crack initiation and propagation: local phenomena leading to separation of the material. In equations and figures referring to fracture the subscript 'F' is used. The term *failure* is employed to indicate the state where the structural integrity (global) is compromised due to fracture (local). Physical quantities related to failure are herein indicated using the subscript 'f'.

A *fracture model* describes the local conditions under which fracture occurs in a material. To include failure of elements in the FEM, a *failure model* is required that describes the state at which fracture is expected to occur within an element. Therefore a fracture model can be employed as a failure model for very fine solid elements that are able to accurately describe local conditions.

1.3 Objective

Towards the objective of this research, a selection is made of fracture models that are deemed to provide an increase in predictive capabilities over commonly used methods. This thesis focuses on providing a long overdue solution to employ stress-state dependent fracture models as failure criteria in finite element analysis of ship collision. Unfortunately, the effort to use a more complex fracture model is increased as more experiments are necessary for calibration and implementation into the finite element method requires expert knowledge of the used finite-element package. Therefore two restrictions are imposed on the selected fracture models that limit the required effort to calibrate and to implement the models:

- The fracture model requires no more than three experiments for calibration
- Only the built-in capabilities of the finite-element package are to be used; no user-defined subroutine is required to implement the fracture model in FEM.

To compare the several selected fracture models, a set of experiments is conducted. This set is sub-divisible into *main experiments*, which are drop tower tests designed to imitate raking damage of vessels as presented in Haag [2017]. These experiments were carried out by TNO on S235 structural steel in November of 2016 and are herein used to compare the predictive capabilities of fracture models. Besides the main experiments, several *additional experiments* are carried out on the same material that provide required information on the material behaviour. These experiments are used to obtain a material model and to calibrate the fracture models, allowing simulation of the large scale experiments in the finite element method. The first set of these additional experiments, a set of flat bar tensile tests, was conducted at the same time as the main experiments. As a supplement, three additional sets of experiments were conducted on the same material to obtain additional information required for the calibration of the fracture models. The ultimate goal is to apply different failure models (derived from the selected fracture models) to a finite element model of the large scale experiment and compare the obtained numerical results to the experimental data.

Based on a literature review of the theory behind stress-state dependent fracture prediction and its application in the finite element method a set of research questions is defined. An overview of the literature study is presented in Chapter 2. The main research question is supported by three sub questions.

Which stress-state dependent fracture prediction method yields the smallest error in terms of energy dissipation by plastic deformation of structural steel plating in the event of collision?

1. Which failure models satisfy the imposed restrictions?
2. For the application of the material model, a failure model and friction, what precautions can be taken to restrict the introduction of errors?
3. How can the failure models be applied to a finite element model consisting of shell elements?

1.4 Thesis Outline

This research provides a theoretical approach for the application of stress-state dependent fracture prediction in finite element analysis of ship collision. The chapters of this thesis contain descriptions of the different steps that are required for a comparative analysis of failure models.

Chapter 2 provides an overview of the theory behind fracture of structural steel plating and presents an approach to apply stress-state dependent fracture prediction in finite element analysis containing shell elements. The terminology and notations introduced in this chapter are used throughout the thesis.

Chapter 3 introduces the selected failure models and the associated considerations for their selection. The failure models are presented based on their categorization and a description of the details of each model is provided. Modifications to the models are included where necessary.

Chapter 4 introduces the small scale experiments that were conducted. Based on the theory presented in Chapter 2 a model is created for the material, using the results from these experiments in combination with finite element analysis. Ultimately, the information required for the calibration of the failure models is presented, preceded by a description of the required approaches to obtain this information.

Chapter 5 deals with the application of the failure models in the finite element method: the method for the implementation in the finite element package LS-DYNA is presented, along with the methods for the calibration of the failure models that enable their application.

Chapter 6 focuses on the large scale experiment. First, the experiment itself is described. Subsequently the associated finite element model is presented and the results from finite element analysis with the application of the different failure models are compared to the experimental results.

Chapter 7 is dedicated to presenting the conclusions drawn from the discussion of the results.

Chapter 8 provides several recommendations for future research and for the application of failure criteria in finite-element analysis of maritime collision.

The structure of this thesis is presented schematically in Fig. 1.3.

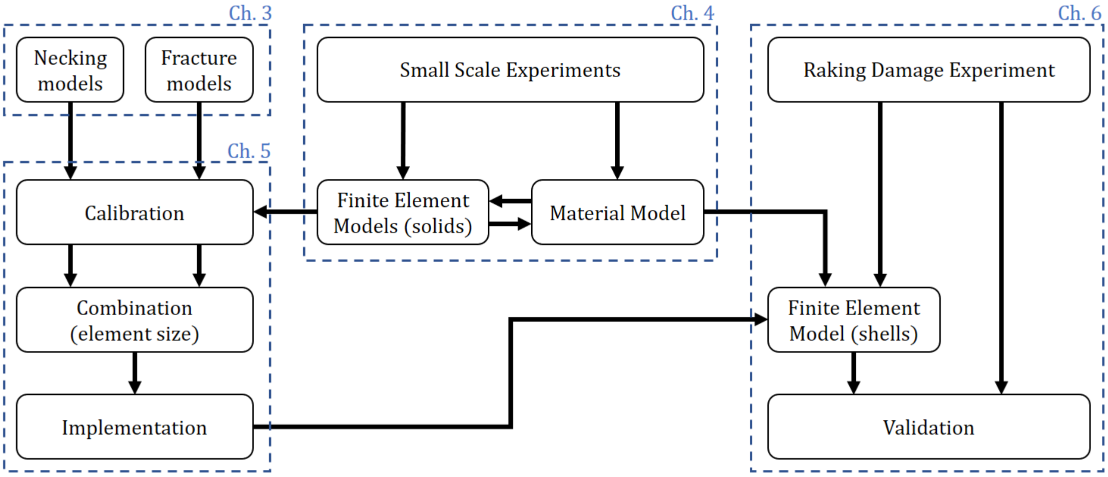

Figure 1.3: Schematic overview of the structure and contents of this thesis

Chapter 2

Failure Modelling Theory

This chapter is dedicated to giving an overview of the various aspects that play a part in the modelling of failure of steel plating during ship collision analysis. Firstly, several important concepts are introduced to provide the theoretical background for this thesis. A description of the material behaviour during deformation until fracture is presented to depict what should be taken into account in the modelling of failure.

2.1 General Concepts

In the current section several general concepts are introduced that are not specifically related to fracture, yet are required to be understood for the modelling of fracture. More importantly, the notation presented in this section is used throughout this thesis.

2.1.1 Stress-state

In this section descriptions of several concepts of solid mechanics and fracture modelling are presented. These descriptions aim to provide a sufficient background knowledge for the understanding of this thesis. As a base for the introduction of these concepts an arbitrary solid volume in an arbitrarily chosen Cartesian coordinate system is used as presented in Fig. 2.1. On this continuum solid several external point forces F and pressures p (forces per unit area) are acting which cause the body to deform. Motion of the solid is constrained by the boundary conditions denoted by b.

The solid volume experiences internal stresses as a result of the external loads and constraints. According to *Cauchy stress theorem*, considering an infinitesimal element A located at any point in the solid, the stresses on the faces of this element can be represented as *normal stresses* perpendicular to the faces and *shear stresses* parallel to the faces. The normal and shear stresses are denoted respectively by σ_{ii} and τ_{ij}, where i and $j \neq i$ indicate any Cartesian dimension. This yields nine stress components, which

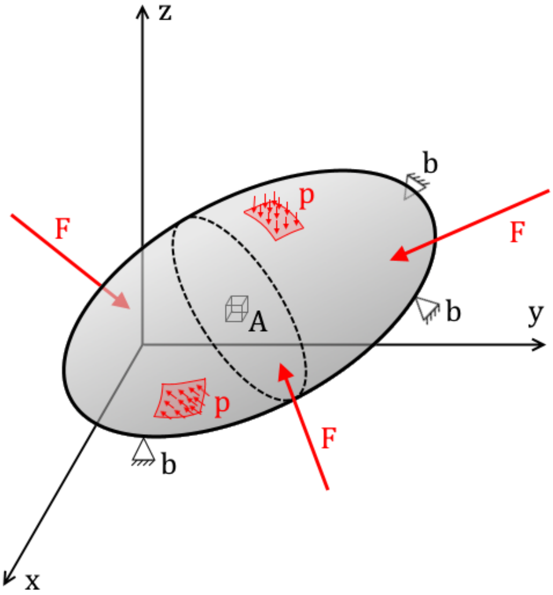

Figure 2.1: Infinitesimal element (A) in continuum solid

are depicted in Fig. 2.2a.

The *stress tensor* $[\sigma]$ is formed by organizing the nine stress components in a second order tensor, which completely describes the *stress-state* at any location within a solid (Eq. 2.1). As the load on the body changes, so does the stress-state in the infinitesimal element. The *load path* of an element is defined as the evolution of the stress-state during a deformation process.

$$[\sigma] = \begin{bmatrix} \sigma_{xx} & \tau_{xy} & \tau_{xz} \\ \tau_{yx} & \sigma_{yy} & \tau_{yz} \\ \tau_{zx} & \tau_{zy} & \sigma_{zz} \end{bmatrix} \tag{2.1}$$

To satisfy rotational static equilibrium of the infinitesimal element, it can be shown that coplanar shear stresses are necessarily equal to each other: $\tau_{ij} = \tau_{ji}$. As a result the stress tensor becomes symmetrical.

Changing the orientation of the coordinate system changes the individual components of tensor, but has no effect on the stress-state of the infinitesimal element. An orientation of the coordinate system exists where the shear stresses are all equal to zero. The remaining normal stresses are named the *principal stresses* and can be obtained by solving the Eigenvalue problem for the stress tensor. The principal stresses are denoted

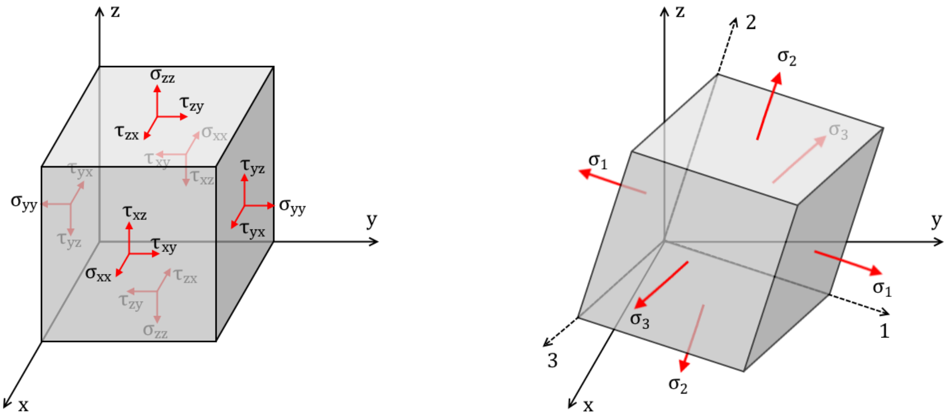

(a) Arbitrary Cartesian coordinates

(b) Principal directions

Figure 2.2: Orientations of infinitesimal element

by σ_i, where $i = \{1,2,3\}$ indicate the *principal directions* of the infinitesimal element (Fig. 2.2b). The order of the principal stresses is defined by $\sigma_1 \geq \sigma_2 \geq \sigma_3$, where positive stresses indicate tension.

The stress-state can be subdivided in two parts: The *hydrostatic stress* and the *deviatoric stress* (Malvern [1969]). The hydrostatic stress σ_m is defined as the mean of the normal stresses (Eq. 2.2), i.e. the component of normal stress equal in all directions and is equal to the negative hydrostatic pressure p:

$$\sigma_m = -p = \frac{1}{3}(\sigma_1 + \sigma_2 + \sigma_3). \tag{2.2}$$

The deviatoric stress s is the part of the stress-state that deviates from the hydrostatic stress. The deviatoric stress tensor $[s]$ is determined according to its definition:

$$[s] = [\sigma] - \sigma_m[I]. \tag{2.3}$$

Here $[I]$ indicates the identity tensor. The *principal deviatoric stresses* s_i with $i = \{1,2,3\}$ are necessarily co-directional with the principal stresses.

Von Mises [1913] proposed a yield criterion, based on the observation that plasticity is independent of the hydrostatic stress and purely depends on the deviatoric part. He defined the *equivalent stress* $\bar{\sigma}$ as a scalar representation of the magnitude of the deviatoric stress:

$$\bar{\sigma} = \bar{\sigma}([s]) = \sqrt{\frac{1}{2}[(\sigma_1 - \sigma_2)^2 + (\sigma_2 - \sigma_3)^2 + (\sigma_3 - \sigma_1)^2]}. \tag{2.4}$$

The hydrostatic and deviatoric parts of the stress-state are depicted in Fig. 2.3 in principal stress space. In this figure the stress-state is represented by the vector $\overrightarrow{OA}$. Hydrostatic part is represented by the vector $\overrightarrow{OO'}$ along the *hydrostatic axis* ($\sigma_1 = \sigma_2 = \sigma_3$), which are related by $|OO'| = \sqrt{3}\sigma_m$. The deviatoric part $\overrightarrow{O'A}$ is orthogonal to the hydrostatic axis and is related to the equivalent stress by $|O'A| = \sqrt{\frac{2}{3}}\bar{\sigma}$.

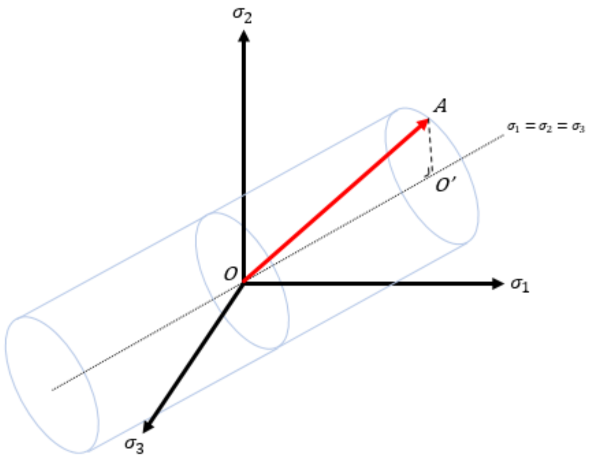

Figure 2.3: Hydrostatic and deviatoric stress components

Rice and Tracey [1969] have shown that an important parameter in fracture prediction is the *stress triaxiality* η, which is defined as the ratio of the magnitudes of hydrostatic stress and the deviatoric stress (Eq. 2.5). The application of triaxiality in fracture prediction is further discussed in Section 3.1.

$$\eta = \frac{\sigma_m}{\bar{\sigma}} \tag{2.5}$$

In Figure 2.3 the triaxiality is therefore proportional to the ratio of $|OO'|$ to $|O'A|$. If the deviatoric stresses are small compared to the hydrostatic stress, the stress state becomes close to equitriaxial, thus the triaxiality parameter reaches to $\pm\infty$, depending on the state being compressive or tensile. On the other hand, if the hydrostatic stress is small compared to the deviatoric stress, for example in pure shear, the triaxiality parameter reduces to zero.

The importance of the triaxiality parameter lies in its effect on the effective plastic strain to failure (Bao and Wierzbicki [2004]): the amount of plastic strain at fracture in a ductile material is dependent on the stress triaxiality as different fracture mechanisms occur for different triaxiality ranges. It can be stated, for example, that the ductility of a material depends on whether the stress-state is in shear, uniaxial or triaxial.

The triaxiality parameter holds information on the relation between the hydrostatic and the deviatoric stresses. However, the direction of the deviatoric stress (perpendicular to the hydrostatic axis) is absent in the formulation of the triaxiality parameter. Therefore the triaxiality parameter is non-unique for any state of stress. For example a triaxiality of zero is associated with pure shear as well as the stress state defined by $\sigma_2 = \sigma_3 = -\frac{1}{2}\sigma_1$. In order to describe the normalized stress state completely, a second parameter is required. This parameter is referred to as the *Lode parameter* (Bai [2008]). The Lode parameter complements the stress triaxiality by providing information on the ratios of the principal stresses. In literature many definitions of the Lode parameter exist (Moxnes and Frøyland [2016]). However, all of these formulations are in some way dependent on the *Lode angle* θ (depicted in Fig. 2.4), the angle between the projections on the deviatoric plane of the stress vector and the first principal stress.

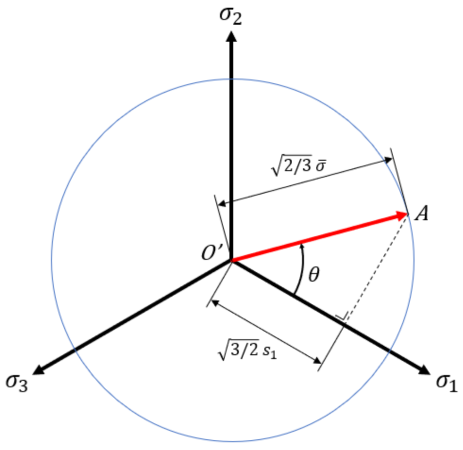

Figure 2.4: Indication of the Lode angle θ in the projection of the stress-state on the deviatoric plane

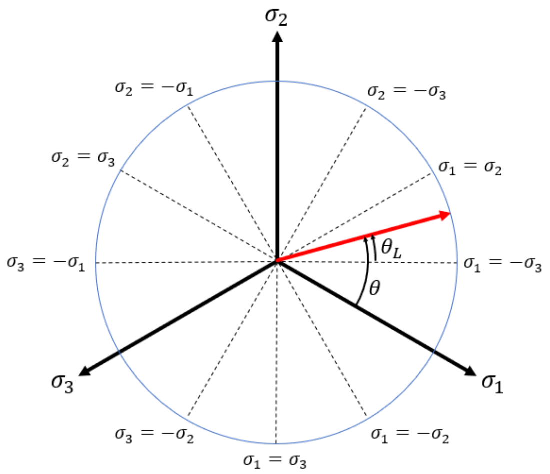

Figure 2.5: Lode angle and shifted Xue Lode angle

In Fig. 2.4 the Lode angle on the deviatoric plane is depicted. The deviatoric plane is the plane perpendicular to the hydrostatic axis (The dotted line in Fig. 2.3) and is coincident with the origin. The Lode angle is limited to the domain $[0, \pi/3]$ due to the principal stress relations $\sigma_1 \geq \sigma_2 \geq \sigma_3$. The Lode angle can be calculated in several ways using the principal and deviatoric stress components. The most straight-forward relation is given in Eq. 2.6 and is depicted by the components in Fig. 2.4.

$$\theta = \arccos\left(\frac{3}{2}\frac{s_1}{\bar{\sigma}}\right) \tag{2.6}$$

As mentioned earlier, several formulations of the Lode parameter exist in literature. Different failure models may use different formulations. The Lode parameters that are relevant for this research are hereafter presented. All formulations of the Lode parameter share the common domain $[-1, 1]$. However their relations to the Lode angle differ: The most common Lode parameter formulation, $\bar{\theta}$, is a linear mapping of the Lode angle on the previously mentioned domain:

$$\bar{\theta} = 1 - \frac{6\theta}{\pi}. \tag{2.7}$$

Another regularly encountered formulation in literature on ductility is the *Normalized Third Invariant* or *Deviatoric State Parameter* ξ. This formulation is important as it is used by the finite element package LS-DYNA, which has been used in this research.

$$\xi = \frac{27}{2}\frac{s_1 s_2 s_3}{\bar{\sigma}^3} = \cos(3\theta) \tag{2.8}$$

In the failure model discussed in section 3.1.1 a shifted version of the Lode angle is used. This Lode angle is herein referred to as the *Xue Lode angle* and depicts the angle between the stress vector and the first principal axis on the deviatoric plane (Fig. 2.5). The formulation of this angle is given in Eq. 2.9:

$$\theta_L = \arctan\left(\frac{1}{\sqrt{3}}\left[2\left(\frac{s_2 - s_3}{s_1 - s_3}\right) - 1\right]\right) = \theta - \frac{\pi}{6}. \tag{2.9}$$

Transformation between the different formulations can be done by intermediate transformation to the Lode angle. The required operations are listed in Table 2.1.

Figure 2.6 depicts the different Lode parameter formulations as a function of the Lode angle. No Lode formulation has any advantage over the others, however distinction between the different formulations is essential: confusing the Lode parameter formulations during the implementation of a fracture criterion in FEM has the potential of causing large errors.

Table 2.1: Lode transformation operations

	To Lode angle	To Lode formulation
$\bar{\theta}$	$\theta = \frac{\pi}{6}(1-\bar{\theta})$	$\bar{\theta} = 1 - \frac{6\theta}{\pi}$
ξ	$\theta = \frac{1}{3}\arccos(\xi)$	$\xi = \cos(3\theta)$
θ_L	$\theta = \theta_L + \frac{\pi}{6}$	$\theta_L = \theta - \frac{\pi}{6}$

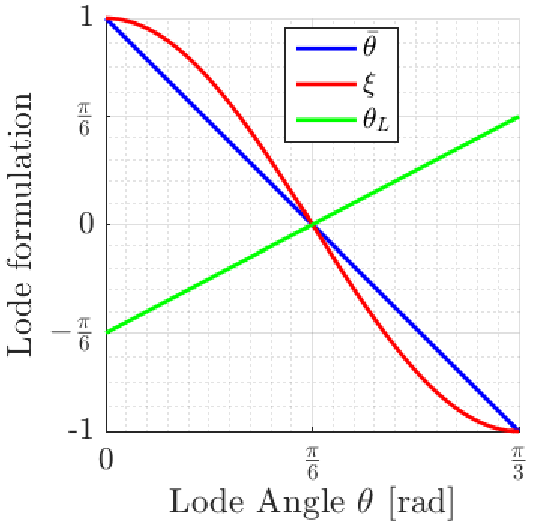

Figure 2.6: Lode parameter formulations

As mentioned in Section 1.2 using shell elements in the FEM is preferred over solid elements due to their computational efficiency. Shell elements inherently rely on the assumption that the stress normal to its plane is equal to zero. It was also mentioned that in-plane tensional stresses tend to dominate over bending stresses in the indented plate during ship collision. This causes the out-of-plane shear stresses to be negligible. Therefore the stress states up to fracture tend to be close to plane-stress conditions. Plane stress in shell elements means that the out-of-plane principal stress (σ_3 in the case of biaxial tension) is equal to zero. This excludes possible stress-states, reducing the triaxiality domain to $[-\frac{2}{3}, \frac{2}{3}]$ and uniquely relating the Lode parameter to the stress triaxiality. This relation is given in Eq. 2.10 in terms of the normalized third invariant and depicted in Fig. 2.7 after conversion of ξ to $\bar{\theta}$ according to Table 2.1.

$$\xi = -\frac{27}{2}\eta\left(\eta^2 - \frac{1}{3}\right) \tag{2.10}$$

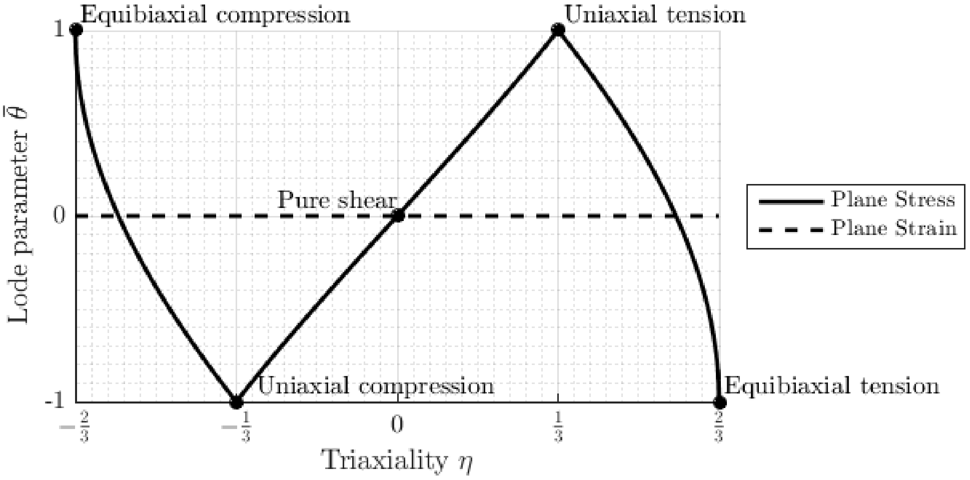

Figure 2.7: Triaxiality & Lode relations

This relation is important for stress-state dependent fracture prediction in shell elements: Due to the absence of one principal stress, the Lode parameter becomes dependent on the stress triaxiality.

2.1.2 Plasticity modelling

In engineering, strain is often defined as the measured elongation ΔL normalized using the initial, undeformed length L_0. The engineering strain e is obtained by:

$$e = \frac{\Delta L}{L_0}. \tag{2.11}$$

However, when this approach is used for plastic strains, an error is introduced as higher order terms are omitted: in order to obtain the true plastic strain ε in a material, the increase in length due to plasticity has to be taken into account in the calculation of the total strain. The true strain is obtained by normalizing the infinitesimal deformation dL to the current length L and integrating from the original length L_0 to the deformed length $L_0 + \Delta L$. This takes into account the increase in length due to plastic strain.

$$\varepsilon = \int_{L_0}^{L_0+\Delta L} \frac{dL}{L} = \ln\left(1 + \frac{\Delta L}{L_0}\right) \tag{2.12}$$

The engineering strain e is only an approximation of the true strain for small elongations: the engineering strain is equal to the first order Taylor series expansion of the true strain around zero.

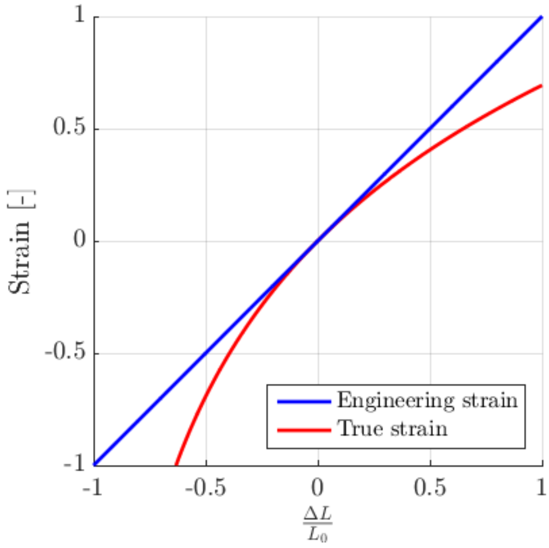

Figure 2.8: Engineering and true strain

For increasing plastic deformation the error of the engineering strain to the true strain increases (Figure 2.8). Stress, being defined as force per area, also exists as both *engineering* and *true stress*. Engineering stress is the applied force divided by the initial load-carrying area. In true stress the change of load-carrying area due to plastic deformation is accounted for. In ship collision large plastic deformations are present, therefore the true stress/strain approach is preferred over the engineering approximation and thus true stresses and strains are adopted in this research.

The total strain consists of an elastic part ε_e; the part of deformation that is reversed when the load is removed, and a plastic part ε_p; the irreversible part of deformation:

$$\varepsilon = \varepsilon_e + \varepsilon_p. \tag{2.13}$$

For linear elastic, isotropic materials the elastic behaviour is commonly described by *Hooke's law*. Structural steel typically shows linear elastic behaviour up to the *proportionality limit* (point A in Fig. 2.9) (Ugural and Fenster [2003]). Up to the *yield strength* (point B) the deformation response is still elastic, however it deviates from the linear behaviour described by Hooke's law. If the stress exceeds the yield strength, irreversible, plastic deformation occurs (point C for example).

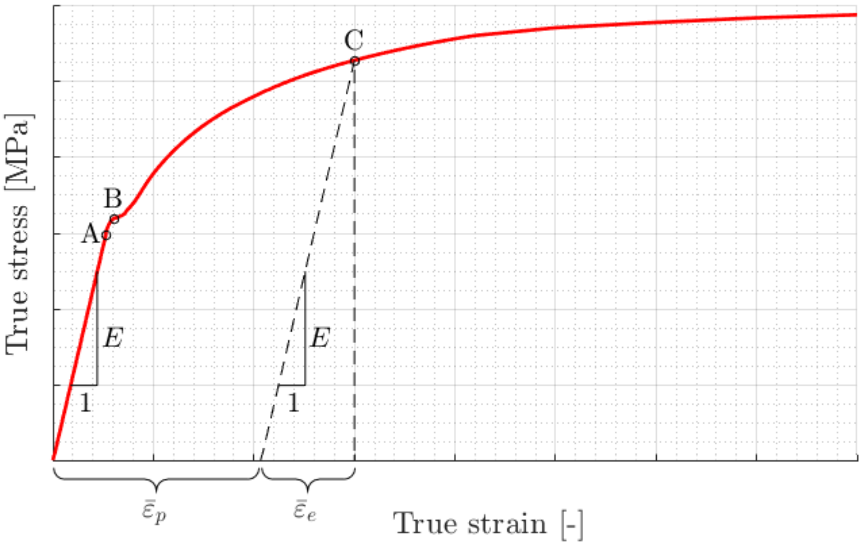

Figure 2.9: Typical true stress-strain curve for structural steel

Orthotropic material properties may be introduced during the fabrication process: The rolling direction may affect the directional material properties of structural steel. In Chapter 4 it is shown that the material considered in this research is highly isotropic and initially shows linear elastic behaviour. As a result the linear elastic strain response can be completely described by the stress-state, the *Young's modulus* and the *Poisson's ratio*.

Analogously to stress, the equivalent plastic strain (EPS) can be obtained from the components of strain in the principal directions:

$$\bar{\varepsilon}_p = \frac{\sqrt{2}}{3}\sqrt{(\varepsilon_1-\varepsilon_2)^2+(\varepsilon_2-\varepsilon_3)^2+(\varepsilon_3-\varepsilon_1)^2}. \tag{2.14}$$

Note that the subscript p has been dropped in the notation of the principal plastic strains in this report for notational purposes. During a deformation process, such as occurs during maritime crash, the mass of the deformed material is conserved. In finite element analysis this translates to conservation of mass of each individual element. Under the assumption that structural steel is a plastically incompressible solid (i.e. the density is independent of plastic strain), the volume of each element is only affected by the elastic part of strain and not by the plastic strain. This is satisfied by the relation in Eq. 2.15 in terms of true plastic principal strains.

$$\varepsilon_1 + \varepsilon_2 + \varepsilon_3 = 0 \tag{2.15}$$

Under the assumption of (plastic) incompressibility the incremental equivalent plastic strain can therefore be written in the form of Eq. 2.16. Note that this relation is only valid for plastic strain. However, in high plasticity the elastic strains are far smaller than the plastic strains and therefore become negligible. Thus Eq. 2.16 is a good approximation of the equivalent total strain if the plastic strain is dominant.

$$d\bar{\varepsilon}_p = \sqrt{\frac{2}{3}}\sqrt{d\varepsilon_1^2 + d\varepsilon_2^2 + d\varepsilon_3^2} \tag{2.16}$$

By defining the *strain ratio* as $\alpha = \varepsilon_2/\varepsilon_1$ and assuming incompressibility and proportional deformation ($\alpha =$ constant during deformation), the equivalent plastic strain can be expressed as

$$\bar{\varepsilon}_p = \frac{2}{\sqrt{3}}\sqrt{1 + \alpha + \alpha^2}\,\varepsilon_1. \tag{2.17}$$

To model the plastic behaviour of a material, a *plasticity model* in the form of Eq. 2.18 is required to relate the evolution of plastic strain to the stress that is required for the material to plastically deform after the onset of yielding.

$$f(\sigma, \varepsilon_p) = 0 \tag{2.18}$$

In Chapter 3 several models for the prediction of failure are introduced that are considered in this thesis. All of these models rely on the assumption of Von Mises-plasticity, which is therefore adopted in this thesis. This theory states that the plasticity model exists in the form of $f(\bar{\sigma}, \bar{\varepsilon}_p) = 0$, meaning that the equivalent stress is related to the equivalent plastic strain by an arbitrary function. This arbitrary function is referred to as the *stress-strain curve* of a material.

In plastic deformation of mild structural steel, typically an increase in stress is required for the material to further plastically deform: plastic deformation is the result of movement of dislocations in the materials' crystalline structure. However, new dislocations are also created by plastic deformation, causing the dislocation density to increase. Dislocations obstruct the movement of other dislocations. A higher dislocation density therefore causes a reduction in the mobility of the dislocations. As a result, a stress increase is required to overcome these obstructions, allowing further movement of the dislocations and further plastic deformation. This is referred to as *work hardening*. This phenomenon is readily observed from a stress-strain curve of a ductile material. An example is presented in Fig. 2.9. In this example a clear increase of stress is visible after the yield strength has been exceeded.

Several models to describe the stress-strain curve of structural steel are in existence. In the context of this thesis two of these models are relevant as the models presented in Chapter 3 rely on them. Firstly, a common model in literature (Bai and Wierzbicki [2008], Mohr and Marcadet [2015]) is *power-law hardening* model as presented by Swift [1952]:

$$\bar{\sigma} = K\big(\varepsilon_0 + \bar{\varepsilon}_p\big)^n, \tag{2.19}$$

where K, ε_0 and n are material-dependent calibration parameters. Another approximation of the stress-strain curve was proposed by Voce [1948] and is given in Eq. 2.20:

$$\bar{\sigma} = k_0 + Q\big[1 - \exp(-\beta\bar{\varepsilon}_p)\big]. \tag{2.20}$$

Here, the parameters k_0, Q and β are used to capture the strain response of a specific material.

Complementary to the stress-strain curve a *flow rule* is required to model the plastic behaviour of a material, which relates the individual components of stress and strain. The finite element package that is used for the realization of this thesis, LS-DYNA, relates the stress and strain components by the assumption that the increment of plastic strain has the same direction as the deviatoric stress. This particular case of a flow rule is referred to as the *associated flow rule* and is formulated as in Eq. 2.21:

$$d\varepsilon_{ij} = d\lambda \frac{\partial\bar{\sigma}}{\partial\sigma_{ij}}, \tag{2.21}$$

Here the subscripts i and j denote the individual components of the stress and plastic strain tensors, and $d\lambda$ is a hardening parameter that is related to the stress-strain curve. For any von Mises plastic material, the flow rule yields the following relations for the principal directions, often referred to as *Hencky's equations*:

$$\frac{d\varepsilon_1}{2\sigma_1 - \sigma_2 - \sigma_3} = \frac{d\varepsilon_2}{2\sigma_2 - \sigma_1 - \sigma_3} = \frac{d\varepsilon_3}{2\sigma_3 - \sigma_1 - \sigma_2} = \frac{d\bar{\varepsilon}}{\bar{\sigma}}. \tag{2.22}$$

The condition where one principal strain component is equal to zero is referred to as *plane strain*. Under the assumption of conservation of volume, this condition is satisfied if and only if $\varepsilon_1 = -\varepsilon_3$. For proportional loading, this condition is obtained when the intermediate principal stress is the average of the minimum and maximum principal stresses:

$$\sigma_2 = \frac{\sigma_1 + \sigma_3}{2} \tag{2.23}$$

This relation causes the second deviatoric principal stress to be equal to zero, resulting in a constant Lode parameter $\bar{\theta} = \xi = 0$. This condition is depicted in Fig. 2.7 and is readily obtained by combining Equations 2.3, 2.8 & 2.23.

Several researchers have investigated the effect of the rate of change of strain in time on the behaviour and established its effect on ductile materials. The *strain rate* is defined as the derivative of strain with respect to time:

$$\dot{\varepsilon} = \frac{d\varepsilon}{dt}. \tag{2.24}$$

Two well known models that describe the effect of strain rate on strain hardening are presented in Johnson and Cook [1983] and Cowper and Symonds [1957], which are given in Equations 2.26 and 2.25 respectively.

$$\bar{\sigma}(\dot{\bar{\varepsilon}}_p) = \bar{\sigma}_0 \cdot \left[1 + C_{JC} \ln(\dot{\bar{\varepsilon}}_p / \dot{\bar{\varepsilon}}_0)\right] \tag{2.25}$$

Here $\bar{\sigma}_0$ is the equivalent stress at a base strain rate of $\dot{\bar{\varepsilon}}_0 = 1\ \mathrm{s}^{-1}$ and a material coefficient C_{JC}.

$$\bar{\sigma}(\dot{\bar{\varepsilon}}_p) = \bar{\sigma}_0 \cdot \left[1 + \left(\frac{\dot{\bar{\varepsilon}}_p}{C_{CS}}\right)^{1/p}\right] \tag{2.26}$$

A suggested value of $C_{JC} = 0.0114$ in Eq. 2.25 for mild steel is given by Børvik et al. [2003]. Storheim and Amdahl [2015] suggest values of $C_{CS} = 4 \cdot 10^5\ \mathrm{s}^{-1}$ and a strain-rate exponent $p = 5$ for mild structural steel (Eq. 2.26). Furthermore they found that strain rates in ship collision are typically in the range of 5-15 s^{-1}. This is supported by the results obtained from finite element analysis later in this thesis. For this range of strain rates it is shown in Fig. 2.10 that the influence of strain rate on the mild steel is negligible using the previously mentioned coefficients from literature.

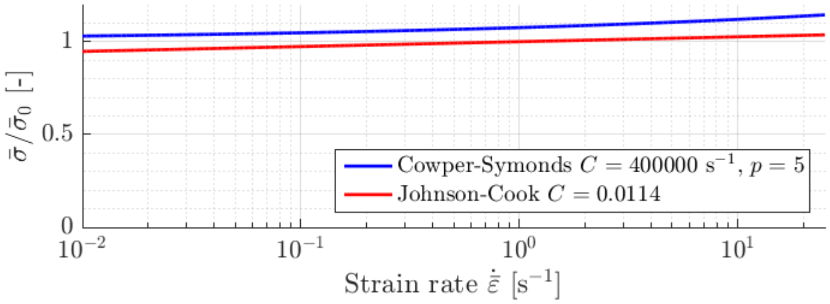

Figure 2.10: Cowper-Symonds and Johnson-Cook relations for strain rate dependency for typical mild structural steel

For this range of strain rates it has been shown by Choung et al. [2013] that strain rate is of negligible influence on the stress-strain curve. This is supported by applying the suggested values to the equations by Cowper-Symonds and Johnson-Cook (Fig. 2.10).

To scale the strain at fracture associated with a base strain rate of 1 s^{-1} Johnson and Cook [1985] suggests the same strain-rate-dependency function as for the stress-strain curve (The term between square brackets in Eq. 2.25). For structural steel a constant of 0.002 was proposed. This constant is even smaller than the constant suggested for the strain-rate dependency of the stress-strain curve, and therefore the strain-rate effect on fracture strain is even smaller. Based on these notions the effect of strain rate is not taken into account in this thesis.

2.2 Ductile Fracture

Typically, the structural response to loads below the design load is elastic, meaning the structure will return to its initial position when the load is removed. When subjected to larger loads, like accidental loads, plastic (irreversible) deformation may occur within the structure before failure. Materials that show this behaviour are referred to *ductile materials*. Its opposites are called *brittle materials*, which show close to no plastic deformation before failure. The ductility of a material is defined as the ability to plastically deform before fracture occurs. In Fig. 2.11 three fractured specimens of different ductility are depicted.

Commonly, structural steels are ductile materials, however, their ductility is conditional: For instance, the ductility of a material, expressed as effective plastic strain

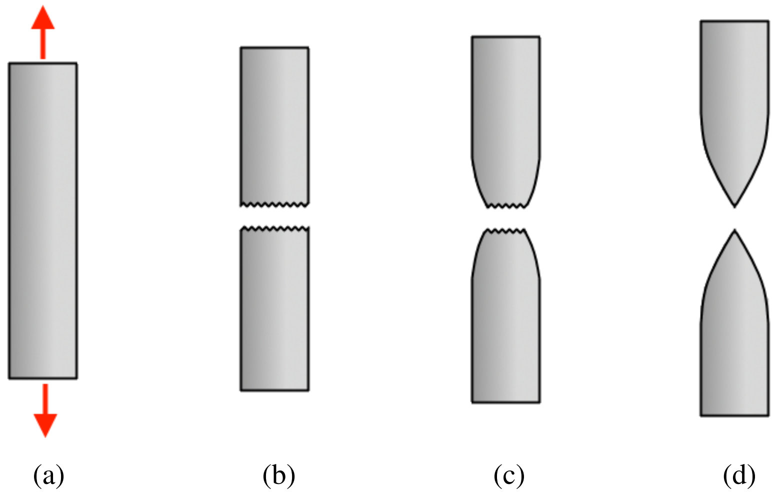

Figure 2.11: Brittle and ductile fracture under uniaxial tension. (a) original specimen. (b) brittle fracture. (c) moderately ductile fracture. (d) highly ductile fracture

to fracture, depends on the chemical composition and temperature of the material, but also on the state of stress and the presence of initial voids. In this section the general mechanics behind ductile fracture are presented.

2.2.1 Strain Localization

In Section 2.1 the concepts of work hardening and conservation of volume have been explained. The conservation of volume relation shows that the cross-sectional (load-carrying) area is reduced due to plastic deformation in the tensile direction. This has an increasing effect on the stress inside the material. At some point in the deformation process this increase in stress may become larger than the increase in strength due to work hardening. At this point the maximum load-carrying capacity, or *Ultimate Tensile Strength* (UTS), has been reached. Beyond this point the specimen becomes unstable, meaning that the load-carrying capacity of the specimen further decreases and the specimen will ultimately fail if the load is not reduced. This phenomenon is called *necking*. An example has been presented in Fig. 2.12 for a typical uniaxial tensile test.

Depending on the material, the geometry and the load, necking may affect the strain distribution in the material and cause a local strain concentration. As a result of the local changes in geometry due to this strain concentration, stresses develop in the directions perpendicular to the loading and thus the stress-state is affected: the hydrostatic compo-

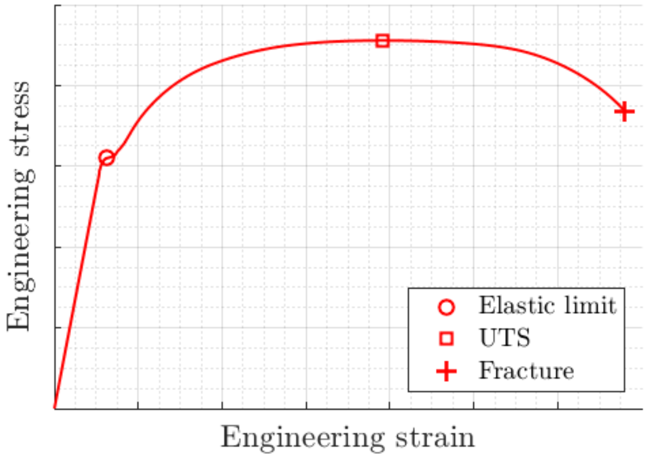

Figure 2.12: Example engineering stress-strain curve of a uniaxial tension test on structural steel

nent of stress is increased due to the presence of the neck (Bridgman [1952]). As a result the stress-state becomes more triaxial and the plane stress condition is violated. In the event of maritime crash, necking may occur in plastically deforming plates, resulting in a local change of the stress-state from plane stress to a fully three-dimensional one.

Necking typically occurs in plate material loaded by in-plane tension. In plate specimens two types of necking can occur (Lian and Zhou [1989]): the onset of necking in a uniaxial flat bar test tends to occur in the direction of the width of a specimen. This type is called *diffuse necking* (Fig. 2.13a). However, in more biaxial states of stress fracture may occur without the precedence of diffuse necking. Generally in a later stage of plastic deformation, through-thickness necking, or *localized necking* may occur (Fig. 2.13b). Localized necking can also occur without precedence of diffuse necking if the geometry restrains necking in the direction of the width.

2.2.2 Fracture Initiation

Plastic deformation is followed by fracture if the plastic strain exceeds the material's ductility. However, which failure mechanism controls fracture is highly dependent on the state of stress. In the domain of maritime crash, where the stress-states are dominated by tension, fracture is preceded by the nucleation of voids, their growth, and eventually coalescence at which point fracture is initiated and cracks start to propagate.

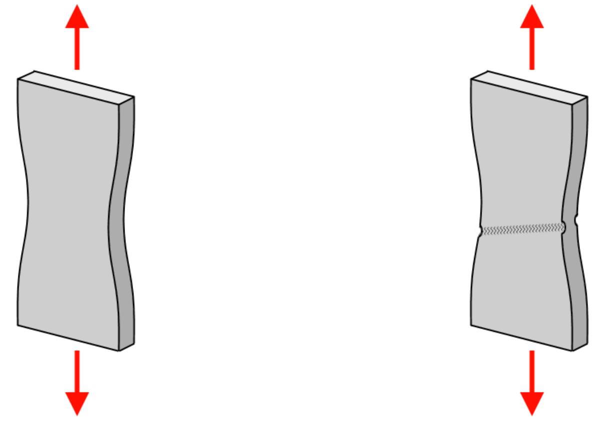

(a) Diffuse necking (b) Diffuse and localized necking

Figure 2.13: Necking in a flat bar specimen

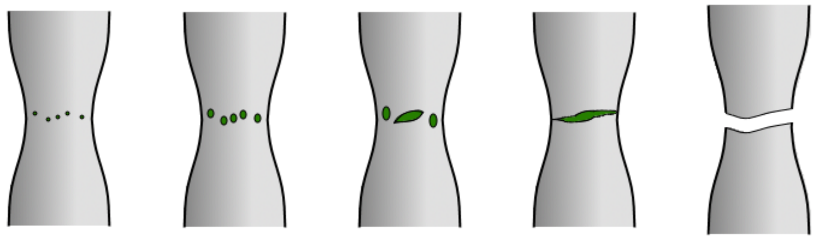

(a) (b) (c) (d) (e)

Figure 2.14: Illustration of the ductile fracture mechanism. (a) void nucleation. (b) void growth. (c) void coalescence. (d) crack propagation. (e) fracture.

In Fig. 2.14 the different stages of fracture initiation by void nucleation, growth and coalescence (VNGC) have been depicted. Note that the voids have been enlarged for illustrative purposes, actual void sizes are in the order of 10^0 to 10^1 μm (Qiu et al. [2003]). In high plasticity, voids in the material start to nucleate by decohesion or by fracture of second-phase particles (2.14a). Under increasing plasticity, the voids grow (2.14b) until their sizes interfere and the voids coalesce (2.14c). A microcrack is initiated and starts to propagate (2.14d). Continuing crack growth eventually leads to fracture (2.14e).

The effects of the stress-state on the VNGC mechanism has been studied by McClintock [1968] and Rice and Tracey [1969] who showed that the equivalent plastic strain at fracture highly depends on the stress triaxiality. A summary of their pioneering work in the field of fracture prediction is included in Appendix A.

2.3 Fracture in FEM

Where and when fracture is initiated inside a finite element model is controlled by a failure model that dictates under which conditions fracture is expected. These failure models play an important role in this thesis and therefore they are described in separate sections: Chapter 3 offers a description of the different models and their application is discussed in Chapter 5. The current section focuses on translating fracture, a phenomenon in a continuum solid, to a discrete domain.

2.3.1 Finite Element Analysis

In this thesis the finite element package *LS-DYNA* is used to simulate the different experiments that have been conducted. LS-DYNA is suitable for highly nonlinear, dynamic finite element analysis using explicit time integration, making it very adequate for application in this research. This will now be explained.

Linear versus Non-Linear

During the deformation process of ductile steel up to fracture as occurs in maritime collision, the structural behaviour is highly nonlinear for multiple reasons:

1. Large geometrical deformations
2. Material behaviour after the onset of yielding

For any indentation process, a third cause of nonlinearity exists: the area of contact between two surfaces changes during the deformation process. For these reasons, nonlinear FEA is an absolute prerequisite to simulate maritime collisions.

Static versus Dynamic

For any structural, dynamic finite element model a system of differential equations is obtained in the form of Eq. 2.27:

$$[M]\ddot{\mathbf{x}}+[C]\dot{\mathbf{x}}+[K]\mathbf{x}=\mathbf{F_e}(\mathbf{x},t), \tag{2.27}$$

where $[M], [C]$ and $[K]$ indicate respectively the mass, damping and stiffness matrices, which are updated every computational step in the case of nonlinear or dynamic behaviour. The vector $\mathbf{x}$ represents the nodal degrees of freedom. The externally applied force is denoted by $\mathbf{F_e}$. In static analyses, the inertia terms (proportional to the accelerations) and the damping terms (proportional to the velocities) are absent, while the externally applied force is constant in time.

Ship collisions occur in the quasi-static domain, meaning that dynamic vibrations are of negligible influence on the response. The kinematics, however, are important: relative motions lead to contact, contact leads to forces exerted on the structure, forces lead to deformation. The deformation is not instantaneous, since collision is an event that occurs over a certain time-span. Therefore static FEA is not suitable to model ship collisions. Moreover, for the prediction of failure in elements, the full histories of stress and strain are used. This will further be discussed in Chapter 5. For these reasons dynamic FEA is highly preferred and is therefore adopted in this research.

Time Integration

Numerical time integration of Eq. 2.27 can either be done implicitly or explicitly. In explicit time integration, the accelerations are determined by solving the equations of motion, using the known velocities and displacements. Subsequently, the next state $[\mathbf{x}^T\ \dot{\mathbf{x}}^T]^T_{i+1}$ is approximated using the current state $[\mathbf{x}^T\ \dot{\mathbf{x}}^T]^T_i$, the accelerations, and a time increment Δt. The obtained solution is accurate as long as the time increment is sufficiently small.

Implicit integration uses a similar method to approximate the state at a later time in the simulation. After each increment the Newton-Raphson method is used iteratively to find a force equilibrium of the model. This allows the implicit method to use larger time increments, while still obtaining an accurate solution.

Computationally, explicit time integration has a major advantage over the implicit method: in the explicit the equations of motions are solved for the accelerations. This requires computing the inverse of the mass matrix. The explicit method assumes that the mass matrix is lumped and therefore diagonal. Computing the inverse of a diagonal matrix is trivial, as the inverse is obtained from the reciprocals of the individual entries of the diagonal matrix. The implicit method, however, requires solving for the displacements (and rotations, depending on the type of elements), rather than the accelerations.

This requires computing the inverse of the stiffness matrix. Since the stiffness matrix is not diagonal, finding its inverse is computationally very expensive. For this practical reason, using explicit time integration is preferred for dynamic crash analyses.

2.3.2 Crack Propagation

Simulation of a crack propagating through a continuous solid using a discrete model, such as a finite element model, is not straightforward.

In reality, crack growth is a continuous process in both time and space. The discrete nature of a finite element model is inherently unable to capture this phenomenon correctly. Several methods exist to incorporate crack propagation in the finite element method. Three commonly used approaches are herein discussed: cohesive zone elements, element erosion, and the extended finite element method.

Cohesive Zone

One method to model crack propagation in a finite element model is by disconnection of elements using cohesive zones (CZ). In a finite element model using cohesive zones, the elements are not connected to each other by sharing common nodes like in a regular finite element model, but rather by cohesive zone elements. These elements can be massless and do not need to represent a physical volume. Their stiffness is based on a model of the cohesive forces. Therefore this technique requires a model of the cohesive forces between different elements in the form of a traction-separation curve (Fig. 2.16). This curve represents the cohesive forces as a function of the separation distance of the elements. Disconnection between bulk elements (Fig. 2.15) occurs when the separation between the elements exceeds the domain of the traction-separation curve.

An advantage of using cohesive zone elements is the conservation of mass during fracture. Crack growth is highly dependent on the mesh, as the crack can only propagate along the cohesive zone elements. This makes the method highly suitable for known crack paths, for example in the case of separation of laminated materials or composites, but less so for continuous materials. Prediction of ductile fracture would require CZ elements connecting all bulk elements, demanding an increase in computational resources. Moreover, conversion from a ductile failure model to a traction-separation curve is required. This conversion has a detrimental effect on the original failure model, as stress-state dependency is lost: The built-in functionality of LS-DYNA does not allow

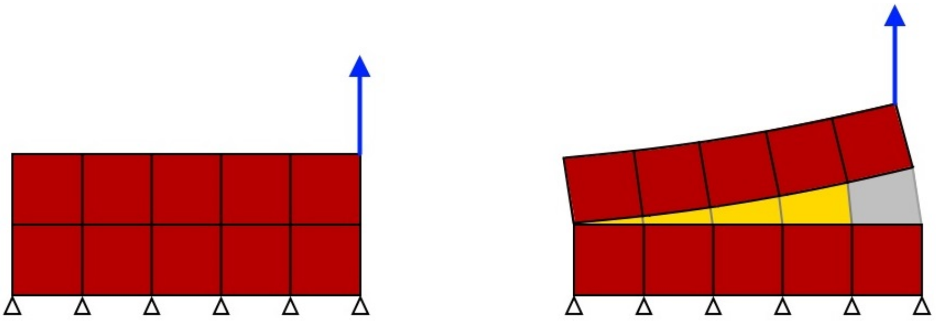
(a) Initial model (b) Deformed situation

Figure 2.15: Cohesive zone illustration. Red: Bulk elements. Yellow: Cohesive zone elements. Grey: Disconnection.

variation of the maximum separation δ_{sep} based on the state of stress.

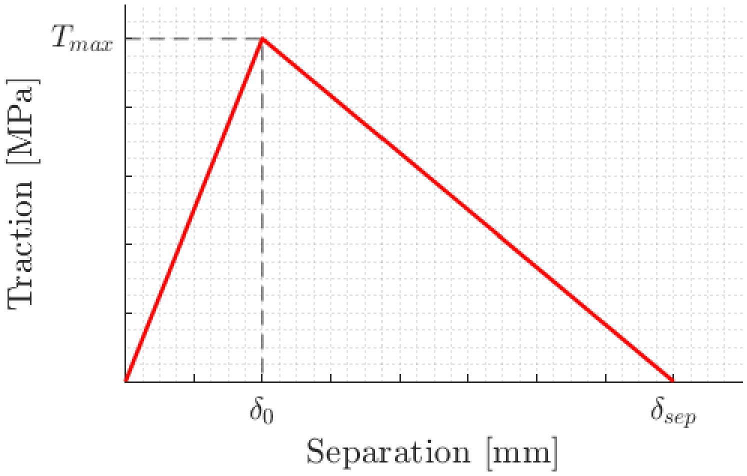

Figure 2.16: Example cohesive force model

Due to the previously discussed aspects, the CZ method is deemed not to be a viable fracture prediction method for the current objective and will not be used in this thesis.

Element Erosion

The most commonly used method to incorporate fracture in the finite element method is Element Erosion. In literature, this method is sometimes also referred to as Element Deletion or Element Removal. For this method, a fracture criterion is required: If a chosen parameter exceeds a critical value in a selected amount of integration points, the associated element is deleted from the FE model. This criterion is evaluated for each element in every timestep.

Due to the removal, the element is no longer able to carry any loads and the total mass of the model is reduced. The size of the elements dictates the size of the crack tip and therefore results in an error of the stress-state at this location.

Despite the previously mentioned disadvantages, this method is often preferred over others due to its wide availability in commercial finite element packages, its easy implementation and its computational advantage over more complicated methods. Most importantly, this method is applicable in combination with sophisticated stress-state dependent failure models. For these reasons, this element erosion is suitable for achieving the intended purpose of offering a stress-state dependent fracture prediction method for application by engineers. Therefore this method is employed throughout this research.

Extended Finite Element Method

As opposed to the previously mentioned methods, the Extended Finite Element Method (XFEM) has no dependency on the mesh. XFEM uses a set of shape functions that are a partition of unity to locally enrich elements. These shape functions allow jumps in the element formulation to model discontinuities, ignoring the discrete nature of the FE model. As a result, crack propagation is allowed to cut through elements. However, analogous to the other methods, the fractured state of each element is a boolean: XFEM does not allow for partially fractured elements. This is depicted in Fig. 2.17 where fractured elements are indicated in gray; the crack ends at the side of an element.

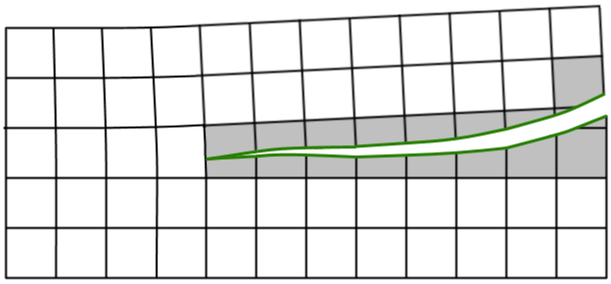

Figure 2.17: Example XFEM crack propagation

Currently, this method has been implemented in LS-DYNA for shell elements and

2D plane strain elements, but only for brittle to semi-brittle fracture of pre-cracked materials (Livermore [2016]) and therefore cannot be used towards the intended goal. However, XFEM has its advantages over element erosion, and might be its future replacement for ductile fracture prediction in FEM when its capabilities have been extended.

2.3.3 Effect of Element Size & Type

In Section 2.2.1 the concept of material instability and the occurrence of necking were discussed. Whether or not necking occurs before fracture depends on the material, but geometry and the loading conditions. Necking is a local phenomenon and has a large effect on the local state of stress, i.e. the state of stress within the neck. In steel plated structures, the size of a neck is in the order of the thickness of the plate. In order to capture the stress-state within a neck, solid elements are required that allow to model the geometry of the neck. The element size should therefore be much smaller than the thickness of the plate. However, engineers prefer to use shell elements due to their computational efficiency. Fine shell elements show similar behaviour to solids for in-plane tension up to the point of necking (Pack and Mohr [2017]). However, necking locally induces out-of-plane stresses. Therefore shell elements are unable to approximate the stress-state inside the neck due to their inherent plane-stress condition. This shortcoming needs to be accounted for in stress-state dependent fracture prediction for shell elements.

As the size of the shell elements is increased, the effect of the strain localization on the total elongation of an element is reduced: the size of the neck becomes small relative to the size of the element and therefore the contribution of the necked region to the total strain becomes negligible. Few researchers have addressed the problem caused by the effect of element size on the predicted strain to fracture. A straightforward and comprehensible method to overcome this problem is suggested by Walters [2014]. His theory states that both a model to predict the onset of necking, a *necking model*, and model to predict the onset of fracture, a *fracture model*, are required to predict the fracture in shell elements: if fracture is predicted before necking occurs, then the fracture model is governing. However, if necking is predicted before fracture, then a combination of the necking model and the fracture model is used. This combination depends on ratio of the element size to the thickness of the plate material. According to this theory, the failure strain $\bar{\varepsilon}_f$ is expressed by Eq. 2.28:

$$\bar{\varepsilon}_f = \min\left\{\bar{\varepsilon}_N + (\bar{\varepsilon}_F - \bar{\varepsilon}_N)\cdot\gamma\,,\,\bar{\varepsilon}_F\right\}, \tag{2.28}$$

where $\bar{\varepsilon}_N$ is the equivalent plastic strain at the onset of necking, or *necking locus*, $\bar{\varepsilon}_F$ is the equivalent fracture strain from the calibrated fracture model, or *fracture locus*, and γ is a weighting factor dependent on the plate thickness and element size:

$$\gamma = \frac{l_e^{cal}}{t^{cal}}\cdot\frac{t}{l_e}, \tag{2.29}$$

where l_e^{cal} and t^{cal} are the element side length and plate thickness that were used for calibration of the fracture locus. An example of this theory is depicted in Fig. 2.18 for an arbitrary necking and fracture locus in terms of equivalent plastic strain to failure and stress triaxiality.

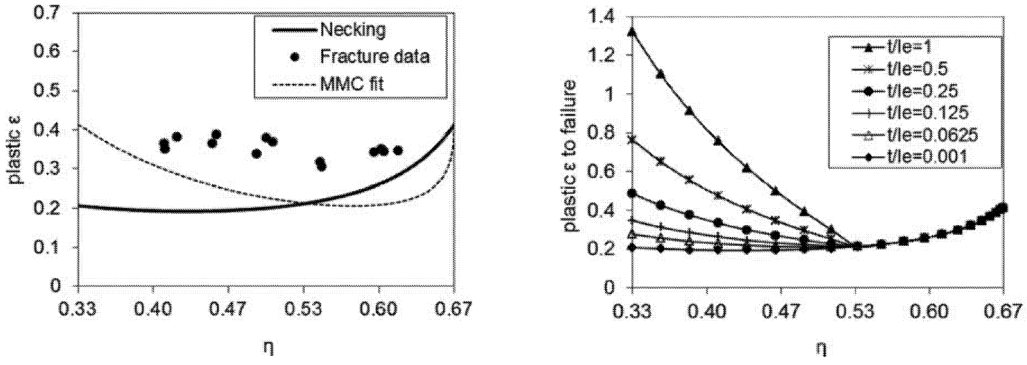

(a) Swift necking and MMC fracture locus (b) Element size dependent failure locus

Figure 2.18: Illustration of the theory to include element size dependency (from Walters [2014])

This theory provides scaling of the fracture strain for element sizes that are larger than the element size used for calibration.

Chapter Summary

In this chapter an overview of the important theory behind numerical fracture prediction is presented. The information contained in this chapter is relevant for the understanding of this thesis, as not only important aspects were explained, but also the symbols and notations that are used in this thesis are introduced.

Chapter 3

Failure Models

To predict ductile fracture in ship collision using finite element analysis by erosion of elements, a failure criterion is required to determine the final state of the elements at which deletion occurs. To this goal, failure models are used which can be calibrated to a certain material. The result of a calibrated failure model is called a *locus* and represents a failure criterion as a function of certain state parameters. The characteristics of these failure models are discussed in this chapter.

A failure model describes the state at which fracture is expected to occur within an element. Based on the framework presented by Walters [2014] (Section 2.3.3) both a fracture model and a necking model are required to obtain a failure model.

Many fracture models exist, therefore a selection is made based on analysis of the history of fracture prediction: the progression in time of the fracture mechanics community is studied to gain understanding of the state of the art of ductile fracture prediction. A literature review of fracture prediction history is included in Appendix A. Based on the previously mentioned analysis of the progression of modelling of ductile fracture, several fracture models were selected that relate the equivalent plastic strain at fracture (EFS) to the stress triaxiality and Lode parameter. Due to the high level of sophistication of these models, the required effort for calibration exceeds the limitations from Section 1.2. Therefore various modifications are proposed that are required for the application of these models. For all fracture models the effect of the different calibration parameters is discussed and example fracture loci are presented for a fully three-dimensional stress states and for tension-based plane stress states to depict the differences between the failure models.

Subsequently two selected necking models and the reasons for selection are introduced. The amount of necking models commonly used in literature is significantly lower than the amount of fracture models in existence. Necking models inherently differ from fracture models: since necking commonly occurs in sheet metal under in-plane tension, necking models are often presented as *Forming Limit Diagrams* (FLDs), which depicts a necking criterion based on the relation of the in-plane principal strains.

An overview of all selected models is presented in Fig. 3.1.

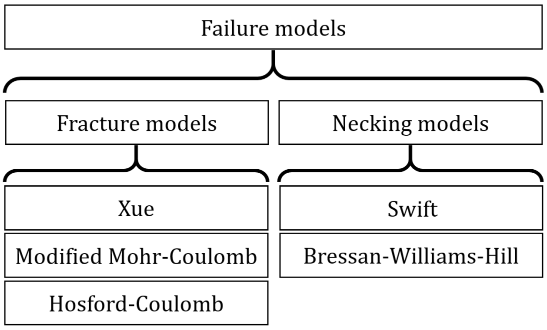

Figure 3.1: Selected models

3.1 Fracture Models

Based on analysis of fracture prediction history (Appendix A) and the criteria posed in Section 1.3 the following fracture models were selected: the Xue model (Xue [2007a,b, 2009]), the Modified Mohr-Coulomb model (Bai and Wierzbicki [2008, 2010]) and the Hosford-Coulomb model (Mohr and Marcadet [2015]). The details of these models are discussed in the following sections.

3.1.1 Xue

Liang Xue introduced a new model to predict the onset of fracture, taking into account the effects of hydrostatic stress, Lode parameter, material weakening and non-linear damage evolution (Xue [2007a,b]). The Xue model assumes that the effects of pressure and Lode parameter are independent of each other and can therefore be decoupled. The model is presented in the form of Eq. 3.1:

$$\bar{\varepsilon}_F(p, \theta_L) = \varepsilon_{F_0}\, \mu_p(p)\, \mu_\theta(\theta_L). \tag{3.1}$$

In this equation pressure dependency is captured in $\mu_p(p)$. The shape function $\mu_\theta(\theta_L)$ takes care of dependency on Lode angle the effective plastic strain at fracture. The calibration parameter ε_{F_0} affects the height of the locus. Across his many publications and his thesis, Xue introduces a multiplicity of shape functions that can be used in

Eq. 3.1. Due to Xue's acknowledgement of the vast amount of influencing parameters on ductile fracture, calibration of the original failure model is difficult. Moreover, the Xue model is expressed as $\bar{\varepsilon}_F(p, \theta_L)$: To be able to implement this form into LS-DYNA a user defined subroutine is required. Since one of the goals of the present study is to provide a practical way to predict fracture in the FEM, implementing a subroutine is deemed not to be a viable option.

Alternatively, the model has to be converted to the space of $\bar{\varepsilon}_F(\eta, \theta_L)$. A suitable formulation of the original model has been presented in [Xue, 2007b, p. 86-87] that holds at least five calibration parameters.

The increased effort to calibrate this formulation conflicts with the goal to provide a practical solution for fracture prediction. Therefore an adjustment to the Xue model is herein proposed. This modification is based on a simplified variation of the Xue model, which will now be discussed.

Simplification

In Xue [2009] a simplification to the original 2007-model is proposed. This simplification holds only two calibration parameters and is a stress-based fracture criterion, which retains the decoupling of pressure and Lode dependence (Eq. 3.2). Note the similarity between this equation and Eq. 3.1.

$$\bar{\sigma}_F(p, \theta_L) = \sigma_{F_0}\, y_p(p)\, y_\theta(\theta_L) \tag{3.2}$$

Subsequently, the model was converted to the same space of the original model under the assumption of an adjusted Swift-type power law to describe the hardening behaviour of the material:

$$\bar{\sigma} = \sigma_{y_0}\left(1 + \frac{\bar{\varepsilon}_p}{\varepsilon_0}\right)^n. \tag{3.3}$$

For the pressure and Lode dependency, Xue proposes the shape functions presented in Eq. 3.4 in Xue [2009].

$$y_p(p) = 1 + k_p p, \tag{3.4a}$$

$$y_\theta(\theta_L) = \tfrac{\sqrt{3}}{2\, \cos\theta_L} \tag{3.4b}$$

In this formulation the reference fracture stress σ_{F_0} and the material constant k_p are the only calibration parameters, which only affect the shape of the pressure dependency and the height of the fracture locus; the mathematical flexibility to adjust the shape of the Lode dependency is lost.

Triaxiality conversion

By definition, the stress triaxiality is given by:

$$\eta = \frac{\sigma_m}{\bar{\sigma}} = \frac{-p}{\bar{\sigma}}. \tag{3.5}$$

The triaxiality was introduced into Eq. 3.2 by substitution of $p = -\eta\bar{\sigma}_F$ into the pressure dependency function (Eq. 3.4a):

$$\bar{\sigma}_F = \sigma_{F_0}\left(1 - k_p\eta\bar{\sigma}_F\right)\frac{\sqrt{3}}{2\cos\theta_L}. \tag{3.6}$$

The resulting formulation is recursive with respect to $\bar{\sigma}_F$. Solving for the equivalent stress at fracture yields:

$$\bar{\sigma}_F = \frac{\sigma_{F_0}}{\sigma_{F_0}k_p\eta + \frac{2}{\sqrt{3}}\cos\theta_L}. \tag{3.7}$$

Analogously to Xue's approach, the current stress-based formulation was converted to the required space by equating Eq. 3.7 and the Swift hardening power law (Eq. 3.3). Solving for $\bar{\varepsilon}_F$ yields a formulation of the Xue fracture model in the space of triaxiality, Lode angle and equivalent strain at fracture:

$$\bar{\varepsilon}_F(\eta,\theta_L) = \varepsilon_0\left\{\left[\frac{\sigma_{F_0}}{\sigma_{y_0}}\cdot\frac{1}{\left(k_p\,\sigma_{F_0}\eta + \frac{2}{\sqrt{3}}\cos\theta_L\right)}\right]^{1/n} - 1\right\}. \tag{3.8}$$

This formulation holds only k_p and σ_{F_0} as calibration constants. The other parameters ε_0, σ_{y_0} and n are material constants and are obtained from a power law hardening fit to the stress-strain curve. After conversion of the Lode formulation according to Table 2.1, this formulation is suitable for implementation in LS-DYNA. This formulation is hereafter referred to as the Xue model.

The parameter k_p regulates the decay of the equivalent strain at fracture as a function of triaxiality. The constant σ_{F_0} only affects the height of the fracture locus. As a result,

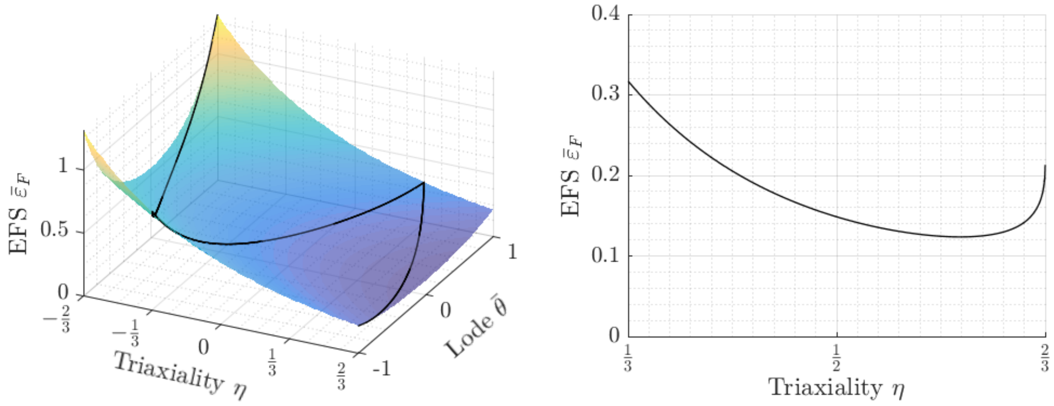

(a) Xue

(b) In-plane tension Xue

Figure 3.2: Example Xue fracture loci for $k_p = 0.00042$ [MPa^{-1}] and $\sigma_{F_0} = 640$ [MPa] with material constants $\varepsilon_0 = 0.002$ [-], $\sigma_{y_0} = 213$ [MPa] and $n = 0.2$ [-].

this form of the Xue model does not have the mathematical flexibility to tune the Lode dependency. Moreover, the fracture locus is assumed to be symmetrical with respect to plane strain ($\bar{\theta} = 0$, see Section 2.1).

3.1.2 Modified Mohr-Coulomb

The original Mohr-Coulomb failure model is based on the assumption that fracture occurs when the maximum value of a linear combination of the normal stress σ_n and shear stress τ on a plane reaches a critical value (Eq. 3.9).

$$\max(\tau + c_1\sigma_n)_F = c_2 \tag{3.9}$$

The coefficient c_1 is related to the slope of the linear combination and affects the relation between the normal and shear stress at fracture. It is often referred to as the negative tangent of the internal angle of friction of the material. c_2 is referred to as the cohesion of a material and represents the shear stress at fracture in pure shear.

Bai and Wierzbicki [2008] presented a plasticity model with dependency on stress triaxiality and the Lode parameter. This relation is shown in Eq. 3.10, in which the first term represents power-law strain hardening, the second term accounts for the hydrostatic stress dependency in the form of triaxiality, while the last term depends on the Lode parameter, which is related to the parameter γ.

$$\bar{\sigma} = [K\bar{\varepsilon}_p^n][1 - c_\eta(\eta - \eta_\text{o})][c_\theta^s + (c_\theta^{ax} - c_\theta^s)\gamma], \tag{3.10}$$

where

$$\gamma = \frac{\sqrt{3}}{2 - \sqrt{3}} \left\{ \sec\left(\frac{\bar{\theta}\pi}{6}\right) - 1 \right\} \tag{3.11}$$

and c_η, η_o, c_θ^s and c_θ^{ax} are calibration parameters and K and n are material parameters associated with power-law hardening. Combination of this plasticity model with the Mohr-Coulomb failure model and conversion to the $\bar{\varepsilon}_F, \eta, \bar{\theta}$ space results in the Modified Mohr-Coulomb failure model that is presented in Bai and Wierzbicki [2010].

$$\begin{aligned}
\bar{\varepsilon}_F(\eta, \bar{\theta}) = & \left\{ \frac{K}{c_2} [1 - c_\eta(\eta - \eta_\text{o}] \cdot \right. \\
& \left[c_\theta^s + \frac{\sqrt{3}}{2 - \sqrt{3}} (c_\theta^{ax} - c_\theta^s) \left\{ \sec\left(\frac{\bar{\theta}\pi}{6}\right) - 1 \right\} \right] \cdot \\
& \left. \left[\sqrt{\frac{1 + c_1^2}{3}} \cos\left(\frac{\bar{\theta}\pi}{6}\right) + c_1 \left\{ \eta + \frac{1}{3} \sin\left(\frac{\bar{\theta}\pi}{6}\right) \right\} \right] \right\}^{-\frac{1}{n}},
\end{aligned} \tag{3.12}$$

where

$$c_\theta^{ax} = \begin{cases} 1, & \bar{\theta} \geq 0 \\ c_\theta^c, & \bar{\theta} < 0 \end{cases} \tag{3.13}$$

The MMC model holds six calibration parameters and would therefore require at least six experiments to calibrate the model. However, the amount of calibration parameters can easily be reduced: Under the assumption of Von Mises plasticity four calibration parameters are eliminated: $c_\eta = 0$, $c_\theta^s = c_\theta^c = 1$ and the reference triaxiality η_o becomes idle. The reduced form holds only two calibration parameters and is presented in Eq. 3.14:

$$\bar{\varepsilon}_F(\eta, \bar{\theta}) = \left\{ \frac{K}{c_2} \left[\sqrt{\frac{1 + c_1^2}{3}} \cos\left(\frac{\bar{\theta}\pi}{6}\right) + c_1 \left\{ \eta + \frac{1}{3} \sin\left(\frac{\bar{\theta}\pi}{6}\right) \right\} \right] \right\}^{-\frac{1}{n}}. \tag{3.14}$$

Calibration parameter c_1 regulates the asymmetry of the fracture locus with respect to plane strain ($\bar{\theta} = 0$), but also affects the decay in the direction of positive triaxiality. In the case of $c_1 = 0$ the fracture locus is fully symmetrical and loses its dependency on triaxiality and the model is reduced to a maximum shear criterion. Increase the value of c_2 raises the fracture locus. Since c_2 only affects the height of the fracture locus, the triaxiality and Lode dependency cannot be tuned independently.

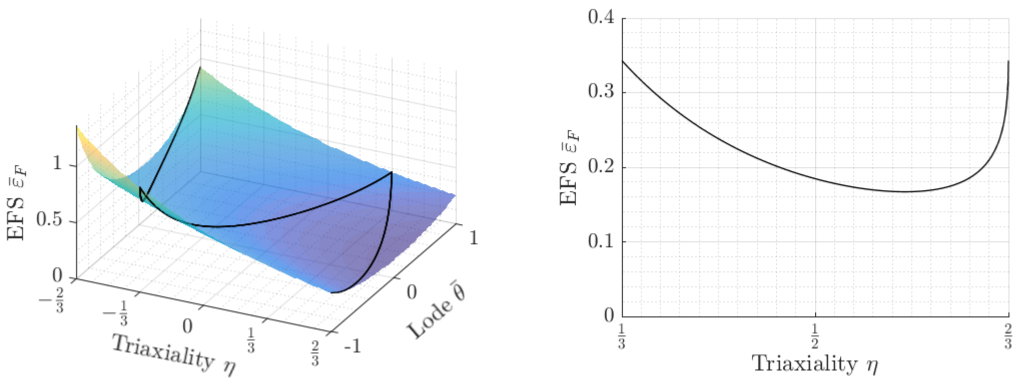

(a) Modified Mohr-Coulomb

(b) In-plane tension MMC

Figure 3.3: Example Modified Mohr-Coulomb fracture loci for $c_1 = 0.1$ [-] and $c_2 = 330$ [MPa] with material constants $K = 740$ [MPa] and $n = 0.2$ [-].

The MMC fracture locus (Fig. 3.3a) holds triaxiality dependence and asymmetric Lode dependence. Combined with the availability of six calibration coefficients, this model is deemed to be very versatile, but difficult to calibrate. However, using simple assumptions, it has been shown that the model is easily simplified. The two-parameter formulation (Eq. 3.14), i.e. the triaxiality and Lode dependent Mohr-Coulomb criterion, is selected for implementation as it meets the criteria posed in Section 1.3.

3.1.3 Hosford-Coulomb

Similar to the MMC model, Mohr and Marcadet [2015] published a fracture model based on the original Mohr-Coulomb criterion. By revising Eq. 3.9 and introducing the Hosford equivalent stress, they obtained a fracture criterion in the form of Eq. 3.15:

$$\left\{\frac{1}{2}\left[(\sigma_1-\sigma_2)^a+(\sigma_2-\sigma_3)^a+(\sigma_1-\sigma_3)^a\right]\right\}^{1/a}+c(\sigma_1+\sigma_3)=b, \tag{3.15}$$

where a, b and c are calibration parameters. Expressing the principal stresses in terms of equivalent stress, triaxiality and Lode parameter yields a stress-based fracture criterion:

$$\bar{\sigma}_F(\eta,\bar{\theta}) = \frac{b}{\{\frac{1}{2}[(f_1-f_2)^a+(f_2-f_3)^a+(f_1-f_3)^a]\}^{1/a}+c(2\eta+f_1+f_3)}, \tag{3.16}$$

where:

$$f_1(\bar{\theta}) = \frac{2}{3}\cos\left(\frac{\pi}{6}(1-\bar{\theta})\right) \tag{3.17a}$$

$$f_2(\bar{\theta}) = \frac{2}{3}\cos\left(\frac{\pi}{6}(3+\bar{\theta})\right) \tag{3.17b}$$

$$f_3(\bar{\theta}) = -\frac{2}{3}\cos\left(\frac{\pi}{6}(1+\bar{\theta})\right) \tag{3.17c}$$

To express this stress-based criterion in terms of equivalent plastic fracture strain, the authors propose power law hardening that is a combination of the formulations as proposed by Swift [1952] and Voce [1948] (Equations 3.18a & b respectively).

$$k_{Swift}(\bar{\varepsilon}_p) = K\,(\varepsilon_0+\bar{\varepsilon}_p)^n \tag{3.18a}$$

$$k_{Voce}(\bar{\varepsilon}_p) = k_0+Q\,[1-\exp\left(-\beta\bar{\varepsilon}_p\right)] \tag{3.18b}$$

$$k(\bar{\varepsilon}_p) = (1-\alpha)k_{Voce}+\alpha k_{Swift} \tag{3.18c}$$

The power law formulations are combined into Eq. 3.18c using a weighting factor α. Applying this formulation to Eq. 3.17 yields the final expression as presented in Eq. 3.19. In the current work this suggested formulation is used in the HC model, however any other Von Mises plasticity rule is applicable to this model.

$$\bar{\varepsilon}_F(\eta,\bar{\theta}) = k^{-1}\left(\frac{b}{\{\frac{1}{2}[(f_1-f_2)^a+(f_2-f_3)^a+(f_1-f_3)^a]\}^{1/a}+c(2\eta+f_1+f_3)}\right), \tag{3.19}$$

where k^{-1} is the inverse function of Eq. 3.18c:

$$\bar{\varepsilon}_p = k^{-1}(\bar{\sigma}). \tag{3.20}$$

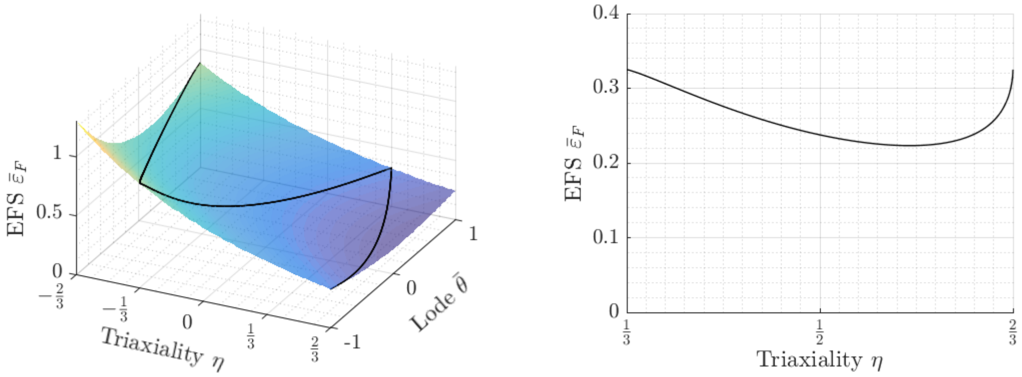

(a) Hosford-Coulomb (b) In-plane tension HC

Figure 3.4: Example Hosford-Coulomb fracture loci for $a = 1.4$ [-], $b = 650$ [MPa] and $c = 0.1$ [-] with material constants $K = 740$ [MPa], $n = 0.2$ [-] and $\varepsilon_0 = 0.002$ [-].

It can be seen from Eqs. 3.19 that the parameters a and c affect only the shape of the fracture locus, while b determines the height. Triaxiality dependency is influenced solely by c: Increasing this parameter results in a steeper decay with respect to positive triaxiality. Parameter a regulates the shape of the Lode dependency. In the case of $a = 2$ and $c = 0$, the models' denominator (Eq. 3.19) reduces to a normalized Von Mises criterion and loses its dependency on both triaxiality and Lode, resulting in the CEFS model.

3.2 Necking Models

As necking typically occurs in plates loaded in biaxial tension, necking models are often displayed in the space of first and second in-plane strains (ε_1,ε_2). Due to the tensional conditions, the third principal strain $\bar{\varepsilon}_3$ is the through-thickness strain and depends on the in-plane principal strains by the relation of the conservation of volume (Eq. 2.15).

In literature, four models to predict the onset of necking are regularly encountered:

- *Marciniak-Kuczynski* forming limit model
- *Swift* diffuse necking criterion
- *Hill* local necking criterion
- *Bressan-Williams* shear instability criterion

As opposed to the other failure models discussed in this section, the Marciniak-Kuczynski (MK) model does not exist in an analytical form. This model consists of mathematical model of an infinite plate with an initial defect loaded by in-plane tension. A set of equations relates the far-field strains to the strains within the initial defect. Combination of these equations yields a complex integro-differential equation (Marciniak et al. [1973]) that can be solved. A failure locus is obtained by solving for multiple far-field strain conditions with varying strain ratios $\alpha = \varepsilon_2/\varepsilon_1$. However, this model fails to account for the orientation of the necking band. Secondly, the obtained necking locus is highly dependent on the magnitude of the initial defect. Lastly, the MK model is poorly defined for plane strain conditions. Based on these remarks and the fact that this model requires far more effort to implement than the other necking criteria, the MK model is deemed not to be a viable option for application in maritime collision analysis and is therefore excluded from this thesis.

The remaining three necking models do exist in an analytical formulation and are readily implemented. However, the Hill diffuse-necking criterion is only defined for negative strain ratios, while the Bressan-Williams criterion is only valid for positive strain ratios. To predict the onset of necking, these criteria have been combined in this research as suggested by Alsos et al. [2008].

Figure 3.5 depicts the different necking loci from the selected necking models to serve as an example. The formulations used to obtain these loci are presented in the subsequent sections.

3.2.1 Swift

In Section 2.2.1 it was explained that necking occurs when the decrease of load carrying area becomes larger than the increase in strength due to work hardening. In the case of uniaxial tension, this moment during the deformation is indicated by the *Considère condition* (Eq. 3.21), which states that necking starts when the ultimate tensile strength has been reached:

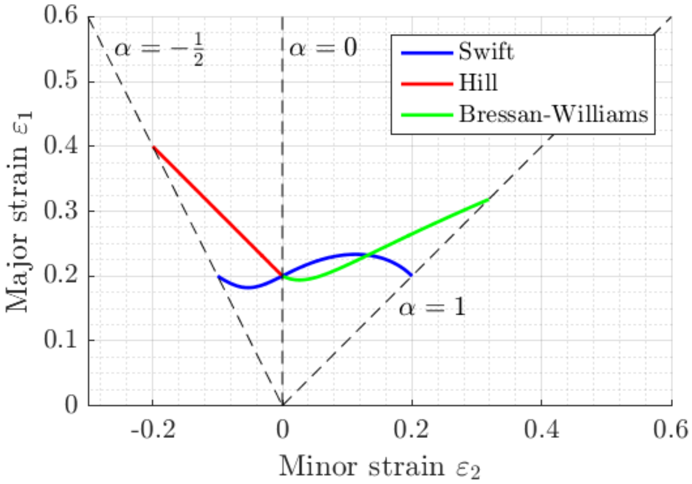

Figure 3.5: Example necking loci for $n = 0.2$

$$\frac{d(F/A_0)}{de_1} = \frac{d[\sigma_1 \exp(-\varepsilon_1)]}{d[\exp(\varepsilon_1) - 1]} = 0. \tag{3.21}$$

By computing the derivative of both the numerator and the denominator of the central expression in Eq. 3.21, the Considère condition is obtained in the form of Eq. 3.22.

$$\frac{d\sigma_1}{d\varepsilon_1} = \sigma_1. \tag{3.22}$$

Swift [1952] expanded the this condition for biaxial tension by adding the same condition for the orthogonal in-plane direction:

$$\frac{d\sigma_2}{d\varepsilon_2} = \sigma_2. \tag{3.23}$$

By combining these conditions with Hencky's equations (Eq. 2.22), Swift obtained a criterion for the onset of diffuse necking. Under the assumption of power law hardening the Swift necking model is given in Eq. 3.24 as a function of the strain ratio α in terms of in-plane principal strains:

$$\varepsilon_{1,N} = 2n\left(\frac{1+\alpha+\alpha^2}{2+\alpha+\alpha^2+2\alpha^3}\right) \tag{3.24a}$$

$$\varepsilon_{2,N} = \alpha\varepsilon_{1,N}, \tag{3.24b}$$

where n is the hardening exponent and the subscript N indicates the condition at the onset of diffuse necking. No further calibration parameters are present in the Swift model. Thus the only material-specific parameter is the hardening exponent, which is obtained from tensile testing as will be discussed in Section 4.3.

3.2.2 Bressan-Williams-Hill

Two types of necking in ductile plate material may occur: diffuse necking in the plane of the plate, or localized necking in the thickness direction. The previously discussed model, Swift, is created for the prediction of diffuse necking. The model discussed in this section, the Bressan-Williams-Hill model, predicts localized necking. This model consists of two parts: the Hill criterion for stress-states between uniaxial tension and plane strain. The Bressan-Williams criterion covers stress-states up to equibiaxial.

Local necking criterion

In the range between uniaxial tension and plane strain the strain ratio is negative ($-0.5 \leq \alpha \leq 0$). In this range localized necking typically occurs along a line of zero extension. Hill [1952] defined the angle ϕ as the angle between this line (the necking band) and the second principal direction (Fig. 3.6) and expressed the angle in terms of the strain ratio:

$$\phi = \arctan(\sqrt{-\alpha}). \tag{3.25}$$

According to Hill's relation for the angle of the localization band (Eq. 3.26) the angle is approximately 35 degrees in uniaxial tension. In plane-strain tension ($\sigma_2 = \sigma_1/2$, $\alpha = 0$) the neck is approximately perpendicular to the direction of the first principal strain ($\phi = 0$). The Hill criterion is invalid for positive strain ratios, as these would lead to imaginary values of ϕ.

Since the strain along the necking band is assumed to be zero, localized necking is predicted when the increase in strength due to work hardening equals the decrease in thickness due to plastic straining:

$$\frac{d\bar{\sigma}}{\bar{\sigma}} = -d\varepsilon_3. \tag{3.26}$$

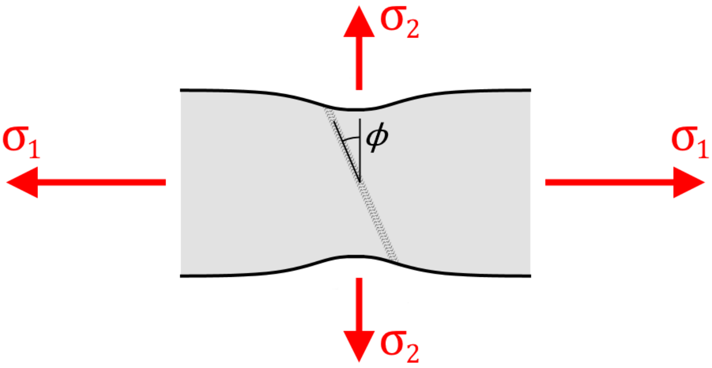

Figure 3.6: Angle of the localized necking band

By assuming proportional straining, meaning that the strain ratio remains constant until necking, and conservation of volume, Eq. 3.26 was rewritten to the form of:

$$\frac{d\sigma_1}{\sigma_1} = (1+\alpha)d\varepsilon_1. \tag{3.27}$$

Hill then proceeds by expressing the criterion in terms of in-plane principal strains by assuming power law hardening in the form of $\bar{\sigma} = K\bar{\varepsilon}_p^n$:

$$\varepsilon_{1,N} = \frac{\hat{\varepsilon}_1}{1+\alpha} \tag{3.28a}$$

$$\varepsilon_{2,N} = \alpha\varepsilon_{1,N}, \tag{3.28b}$$

where $\hat{\varepsilon}_1$ is equal to the power law exponent n. It can, however, also be used as a calibration parameter, indicating the strain at the onset of localized necking in plane strain conditions. The subscript N indicates the condition at the onset of localized necking. In Fig. 3.5 it is shown that the Hill criterion predicts the onset of necking at a later stage than the Swift criterion for negative minor strains. This is obviously caused by the inherent difference between the models: Swift predicts diffuse necking, while Hill predict localized necking, which typically occurs at a later stage during the deformation process.

Shear instability criterion

The Bressan-Williams criterion assumes that necking occurs in a through-thickness plane of zero extension and instability is caused when the shear stress on this plane reaches a critical value. The orientation of the shear plane of zero extension is depicted in Fig. 3.7.

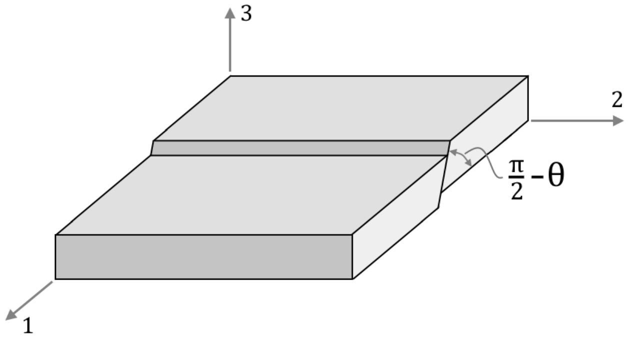

Figure 3.7: Orientation of shear plane

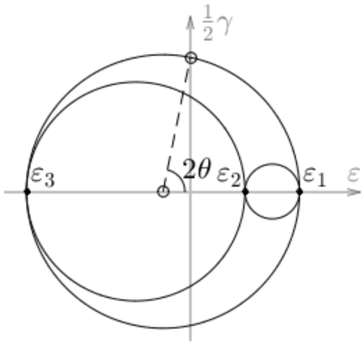

Figure 3.8: Mohr circle for strain with $\alpha = 0.5$

In Bressan and Williams [1983] the angle of the shear plane, θ, is related to the principal strain components: the angle is found using a Mohr circle analysis for strain (Fig. 3.8) and is expressed by:

$$\cos(2\theta) = -\frac{\varepsilon_1 + \varepsilon_3}{\varepsilon_1 - \varepsilon_3} = \frac{\alpha}{2+\alpha}. \tag{3.29}$$

Failure is predicted when a critical value of shear stress is reached. The BW criterion is expressed as Eq. 3.30 for in-plane tensile conditions:

$$\tau_{cr} = \frac{\sigma_1}{2}\sin(2\theta). \tag{3.30}$$

After combining Equations 3.29 & 3.30, the BW criterion is obtained in terms of the first principal stress:

$$\sigma_1 = \frac{2+\alpha}{\sqrt{\alpha+1}}\tau_{cr}. \tag{3.31}$$

Under the assumption of power law hardening the BW criterion is readily converted to the FLD space using the Hencky's equations (Eq. 2.22). For combination with the Hill criterion, Alsos et al. [2008] suggests calibrating the Bressan-Williams locus to the

Hill locus at plane strain ($\alpha = 0$). The critical shear stress τ_{cr} calibrated to the Hill locus then becomes:

$$\tau_{cr} = \frac{1}{\sqrt{3}} K \left(\frac{2}{\sqrt{3}} \hat{\varepsilon}_1 \right)^n, \tag{3.32}$$

where K and n are power law hardening parameters.

Bressan-Williams-Hill criterion

After conversion to strains of the BW criterion and combination with the Hill criterion (Eq. 3.28), the Bressan-Williams-Hill is obtained in the following form:

$$\varepsilon_{1,N} = \begin{cases} \frac{\hat{\varepsilon}_1}{1+\alpha}, & \alpha \leq 0 \\ \frac{1}{\sqrt{\alpha^2+\alpha+1}} \left(\frac{\hat{\varepsilon}_1^{-2n}(\alpha+1)}{\alpha^2+\alpha+1} \right)^{-1/(2n)}, & \alpha > 0 \end{cases} \tag{3.33a}$$

$$\varepsilon_{2,N} = \alpha \varepsilon_{1,N}. \tag{3.33b}$$

This formulation is directly applicable in the FLD space. As suggested by Alsos et al. [2008] the calibration parameter is set equal to the power law parameter n; calibration of $\hat{\varepsilon}_1$ requires an experiment in plane strain conditions. As a result, the BWH criterion only depends on n and the principal strain ratio.

Chapter Summary

In this chapter all failure models selected for implementation were discussed. These models are subdivided in fracture models and necking models. Three fracture models were presented: the Xue model, the Modified-Mohr Coulomb model and the Hosford-Coulomb model. The selection has been augmented with the Swift model and the Bressan-Williams-Hill model for the prediction of the onset of both types of necking. In Chapter 5 these models are calibrated on S235 structural steel and implemented in the finite element package LS-DYNA.

Chapter 4

Analysis of Small Scale Experiments

To be able to create a finite element model of the large scale raking damage experiment, several small scale experiments were conducted. The small scale specimens were cut from the same S235 structural steel plate as the large scale specimens were. The material certificate is presented in Appendix B. The small scale experiments serve two purposes: first, to obtain information on the material's behaviour. Second, to obtain the load paths up to fracture of the experiments,which are required for the calibration of the fracture models. The required theories and assumptions behind the modelling of the material's behaviour were presented in Section 2.1. Calibration of the necking models is based on the material model. This chapter is subdivided in the following parts:

- *4.1 Small Scale Experiments*: Description of the small scale experiments that were conducted and presentation of the results.
- *4.2 Sensitivity Analysis*: Study of the sensitivity of the finite element models to certain modelling parameters.
- *4.3 Material Modelling*: Description of how the material model for finite element analysis was derived from the experimental results.
- *4.4 Critical Elements*: Description of how the load paths for calibration were obtained from the different finite element models.

Each experiment was repeated at least three times to increase the reliability of the results. In total four small scale experiments have been conducted:

- Flat bar tensile test
- Notched flat bar tensile test
- Circular punch test
- Notched "Hašek" punch test

The results of these experiments as well as the results of parallel finite element analysis are herein presented. The used finite element models consist of solid elements to be able to obtain the complex load paths up to fracture. A more detailed description of the finite element models associated with the small scale experiments are presented in Appendix D. In Chapter 5 the results from this chapter are used to calibrate the several failure models.

4.1 Small Scale Experiments

The calibration of a fracture model requires a number of calibration experiments that is larger or equal to the amount of calibration parameters of the model. In the selection of fracture models the largest number of calibration parameters is three (Section 3.1). For the calibration procedure it is critical that the load paths of the experiments up to fracture are different from each other: any errors that may be present in the load paths result in a larger error of the calibrated loci if the load paths are similar to each other. Using more calibration experiments than calibration parameters reduces this effect and increases the reliability of the calibration results, i.e. the calibrated fracture loci. Therefore four different small scale experiments were designed to have different load paths. The different experiments and their results are presented in this section. The geometries of all specimens can be found in Appendix C. All specimens were created from the same structural steel plate as the large scale raking damage specimens.

4.1.1 Flat Bar Tensile Test

The first small scale experiments were conducted concurrently with the large scale raking damage experiment. These were flat bar tensile "dogbone" tests with a thickness equal to the thickness of the plate (6.1 mm) and a width of 20.0 mm. In total six specimens were tested: Two sets of three specimens, cut from the plate in orthogonal directions to obtain information on the orthotropic material properties induced by the fabrication process (Fig. 3.4). The results of these tests are presented in Fig. 4.2, the orthogonal directions are distinguished by the letters 'D' and 'L'.

During the entire deformation process the elongation was measured using an extensometer with a gauge length of 60 mm. The tensile tests were conducted by *Element Materials Technology* according to NEN-EN 10025-2, the associated test report is presented in Appendix E.

Evidence of orthotropic behaviour is only noticeable at the yield plateau: The load normalized with the undeformed load carrying area at which the material starts to yield

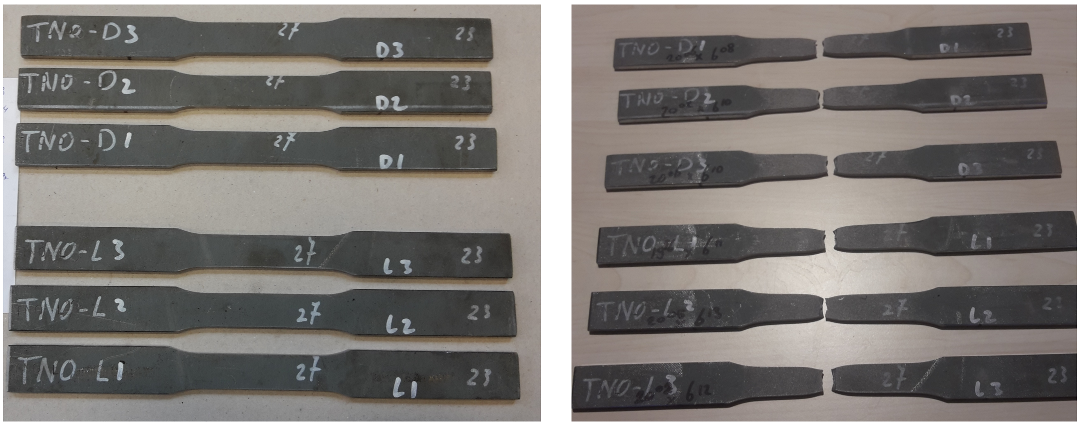

(a) Initial geometry (b) Fractured geometry

Figure 4.1: Tensile flat bar specimens

differs approximately 10 MPa between the orthogonal directions. This difference in material properties becomes imperceptible as the plastic deformation increases. No relation between the engineering strain at fracture and the direction of the specimens exist. For these reasons the material is deemed to be isotropic.

The results from Fig. 4.2 were combined for further use in this thesis: the curves were averaged and truncated at the mean value of the engineering strain at fracture.

4.1.2 Notched Flat Bar Tensile Test

By changing the geometry of a specimen the load path is also changed, for example by introducing notches: adding a notch to a flat bar specimen has the same effect on the stress-state as a diffuse neck of similar geometry. Therefore the stress triaxiality is affected by the presence of the notch. Three notched tensile specimens were tested in laboratory of TNO's Structural Dynamics department. The notched specimen geometry is based on the flat bar tensile specimens, but was adjusted to be compatible with TNO's testing equipment. The notches locally reduced the width of the specimen from 20.0 to 10.0 mm and had a radius of 20 mm. As a result, the length of the notches was approximately 27 mm.

The gauge length of the extensometer was 25.0 mm and was therefore insufficient to span the height of the notch. Therefore the extensometer was modified to a gauge length of 43.4 mm. Specifications of the extensometer and details of the modification

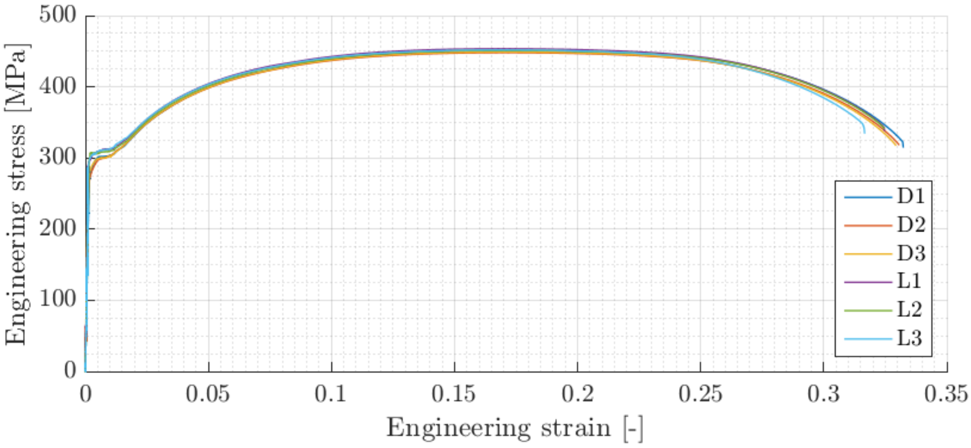

Figure 4.2: Engineering stress-strain results from tensile testing

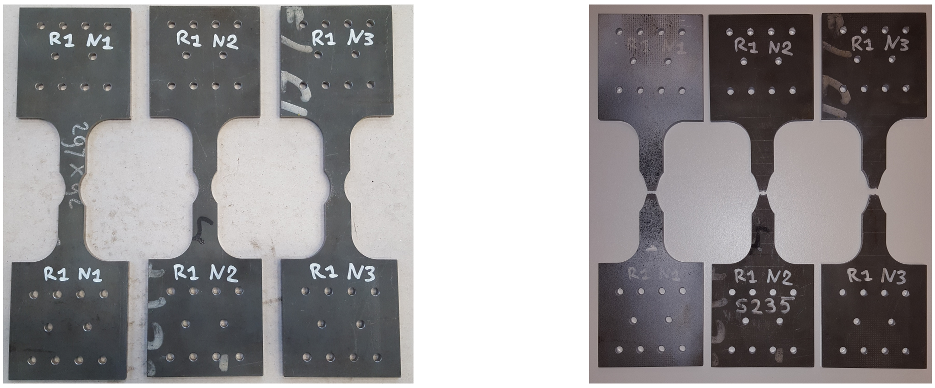

(a) Initial geometry (b) Fractured geometry

Figure 4.3: Notched tensile flat bar specimens

are presented in Appendix F.

The results from the second and third specimen agree very well to each other (Fig. 4.4). However, in the testing of the first specimen there were irregularities: the specimen was already in slight tension before the experiment started and the machine was improperly zeroed. For these reasons the first specimen was neglected in the averaging of the results. Similarly to the flat bar tensile test the results were averaged and truncated to the mean engineering strain at fracture.

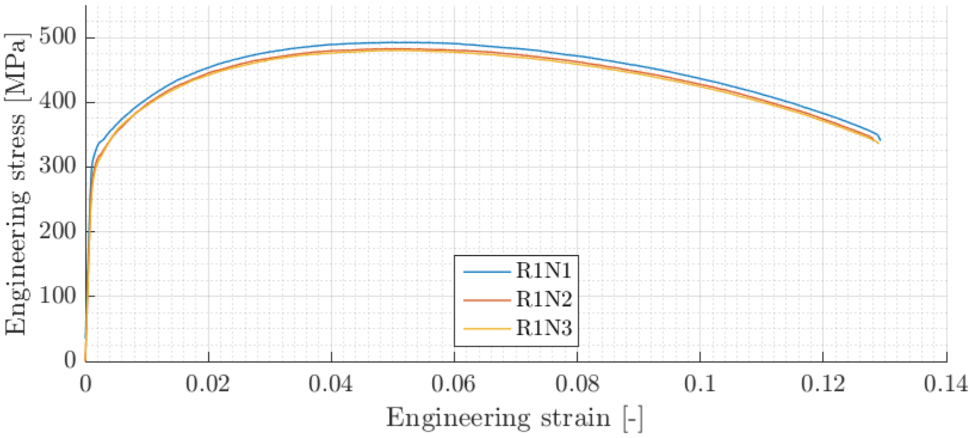

Figure 4.4: Engineering stress-strain results from notched tensile testing

4.1.3 Circular Punch Test

To produce information on fracture of the considered type of steel in a near-equibiaxial state of stress a punch test was conducted. The specimens were circular discs with a diameter of 150 mm. The thickness of the specimen was reduced by 50% near the center of the disc to reduce the stiffness and bending stresses, while preserving any through-thickness differences in material properties induced during the fabrication process of the steel plate (Fig. 4.5a). The specimens were supported by a bottom die and constrained by a top die. The constraints allowed the mounted specimen to freely rotate, while vertical displacement was constrained. A spherical indenter with a radius of 45 mm was used to deform the specimen until fracture. The setup is depicted in Fig. 4.7. Grease was applied to the contact areas of both the specimen and the indenter to reduce friction.

The punch experiment was displacement-controlled, meaning that the motion of the indenter was prescribed. During the first punch test the indentation to fracture was underestimated: Fracture of the specimen had not occurred before the maximum indentation was reached and the indenter automatically started rising again. After the indenter was raised entirely, the experiment was continued to a larger maximum indentation. In Fig. 4.6 the force-indentation curve for the first punch specimen is therefore separated in two parts, R1P1a and R1P1b. Fracture can be observed from the curve belonging to R1P1b as a sudden decrease in force. It can be seen that fracture of specimen R1P1 occurred at an indentation that is slightly larger than the initial maximum inden-

(a) Initial geometry

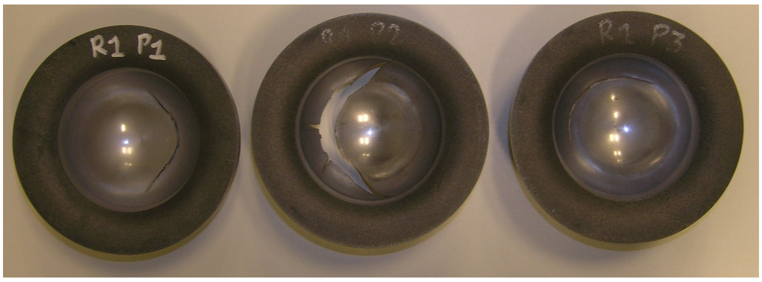

(b) Fractured geometry

Figure 4.5: Circular punch specimens

tation of R1P1a. Moreover, the maximum force of the continued experiment (R1P1b) does not exceed the maximum force before the indenter was raised (R1P1a). This is clear evidence that fracture was nigh at the instant the indenter was prematurely raised. Therefore experiment R1P1b is ignored and fracture is deemed to occur at the maximum indentation of experiment R1P1a. The mean indentation at fracture (obtained from R1P1a, R1P2 and R1P3) was equal to 46.7 mm (Fig. 4.6).

The presented force-indentation curves have been obtained from the testing machine output. Therefore the compliance of the test setup is of influence on the results: the stiffness of the experimental setup is not infinite, therefore the presented indentations are overestimated. Further testing was required to determine the compliance of the machine. In this thesis, the stiffness of the experimental setup is assumed to be far larger than the stiffness of the specimen. Therefore the compliance is neglected. This potentially has an increasing effect on the fracture loci calibrated in Section 5.2.1.

The radial contraction, defined as the decrease of the final diameter of the specimens, was derived from the post mortem measurements: After experiments were conducted the diameter of each specimen was measured across two orthogonal lengths using a height gauge. The radial contraction was obtained by subtracting the original diame-

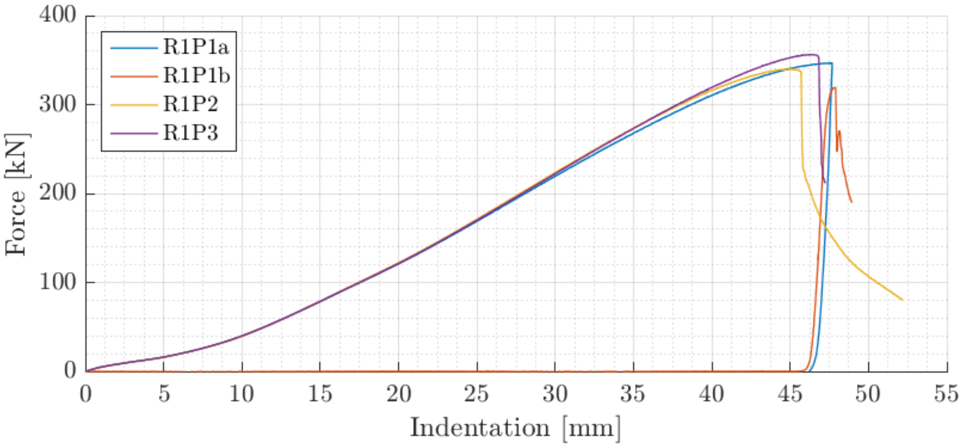

Figure 4.6: Force-indentation results from punch testing

ter. The results are presented in Table 4.1. The average radial contraction amounts to 5.7 mm, which plays an important role in the determination of friction coefficients in Section 4.3.4.

Table 4.1: Radial contraction of punch specimens

Specimen	Direction 1 [mm]	Direction 2 [mm]
R1P1	6.1	5.8
R1P2	5.7	4.7
R1P3	6.1	6.0
mean	5.7	

Table 4.2: Radial distance of crack initiation

Specimen	S [mm]	x [mm]
R1P1	26	24.6
R1P2	32	29.4
R1P3	35	31.6
mean	31	28.5

A second important parameter for the determination of friction coefficients is the distance of the location of crack initiation to the symmetry axis of the punch specimens. In Fig. 4.8 this distance is denoted by x. This distance is highly affected by the amount of friction: a reduction in friction generally reduces the radial crack distance to the center. The specimens were fabricated on a lathe, and therefore the center is readily distinguishable. The arc length S between the center and crack was measured along the indented surface. Assuming that the radius of the arc is equal to the radius of the indenter, the radial distance x is readily obtained using goniometric relations. The results are presented in Table 4.2.

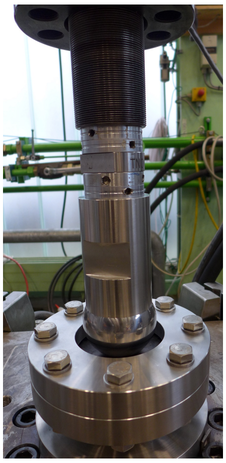

Figure 4.7: Experimental setup for punch testing

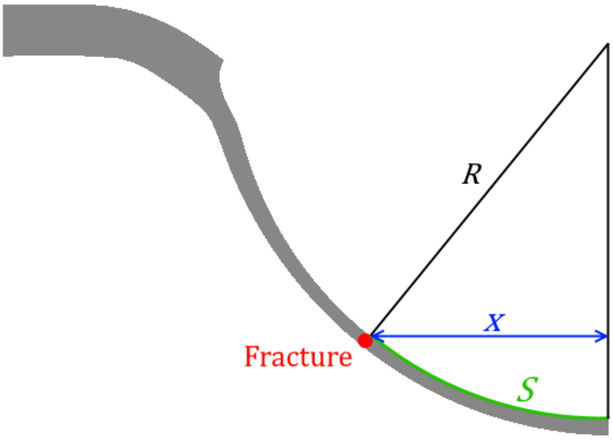

Figure 4.8: Radial distance of the crack to the symmetry axis

The purposes of both the radial contraction and the radial crack distance are to tune the finite element model's deformation field to the experiment. This is discussed in more detail in 4.3.4.

4.1.4 Hašek Punch Test

The fourth small scale experiment bears great resemblance to the previously mentioned experiment as it was based on the geometry of the circular punch test. The punch test specimen geometry was altered to resemble the experiments as proposed by Vladimir Hašek: two cut-outs were removed from the punch specimen geometry. The thick outer ring was kept intact (Fig. 4.9). The experimental setup was identical to the punch setup. As a result, the stress-state of the punch test is reduced to a more uniaxial one. No irregularities occurred during testing.

Similarly to the circular punch test the mean indentation at fracture was determined from the force-indentation curves (Fig. 4.10): A mean indentation of 26.1 mm was obtained. Since the specimens are not axisymmetric, the radial contraction differs depending on the direction of measurement. The remarks in the previous section on the compliance of the machine also hold for the Hašek test. However, its effect was smaller for the Hašek test, since fracture occurred at a lower indentation force.

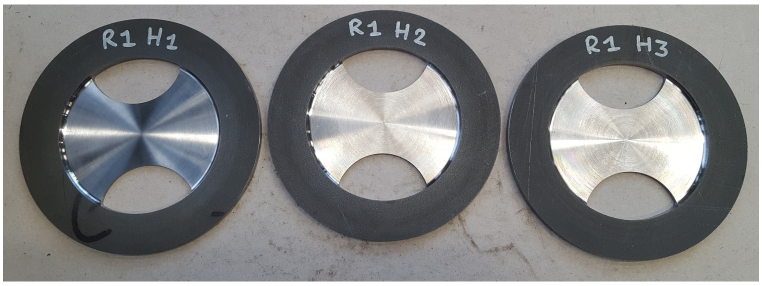

(a) Initial geometry

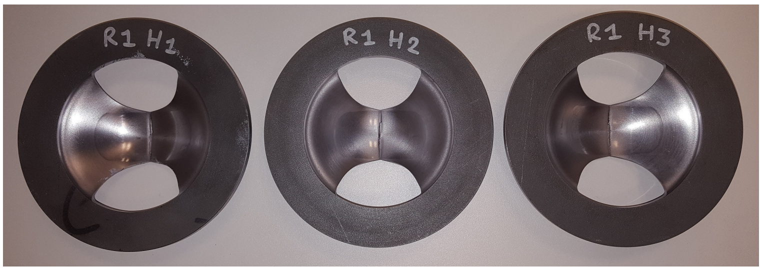

(b) Fractured geometry

Figure 4.9: Hašek punch specimens

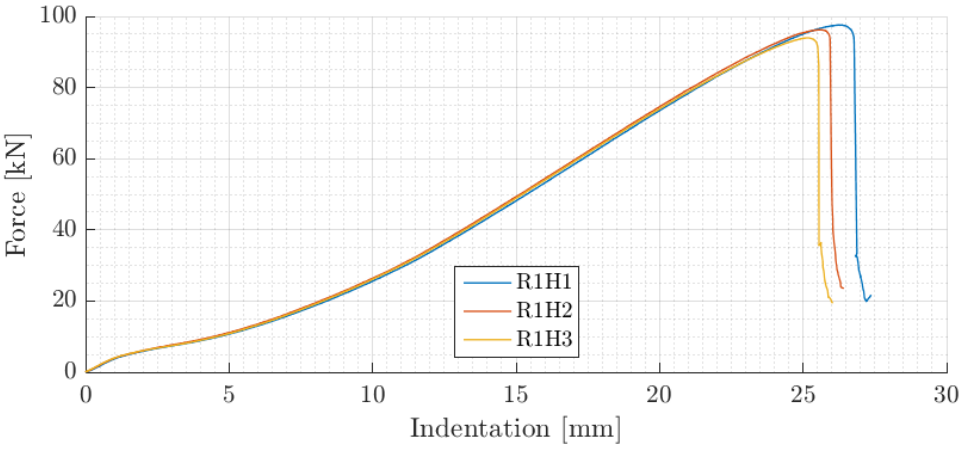

Figure 4.10: Force-indentation results from Hašek punch testing

From Fig. 4.9b it can be observed that fracture occurred in the region where the distance between the circular cut-outs was at a minimum. Herein lies the distinction with respect to the punch test, where crack initiation occurred away from the center: The radial crack distance cannot be used to tune the model, as it is independent of friction.

Table 4.3: Radial contraction of Hašek specimens

Specimen	Radial Contraction [mm]
R1H1	0.2
R1H2	0.2
R1H3	0.2
mean	0.2

The results presented in this section are used to tune the deformation field of finite element model to the experiments. This is discussed in section 4.3.

4.2 Sensitivity Analysis

To obtain the load paths for calibration parallel finite element analysis is required for each small scale experiment. During the finite element modelling of the experiments several important modelling parameters that affect the results were encountered. These influential parameters are hourglass control to avoid erroneous deformations, element size to obtain converged results, and initial defect to trigger the onset of necking. The sensitivity and influence of each of these parameters is studied in this section. Finite element models of the flat bar tensile test were compared in these analyses since the considered sensitivities affect the necking behaviour of finite element models.

4.2.1 Hourglassing

The default solid element in the finite element package LS-DYNA is an 8-node constant stress element with a single integration point. This element has the computational advantage over other solid element formulations. However, this element is subject to zero-energy deformation modes, since it has only a single integration point. The occurrence of these deformation modes is known as *hourglassing*, as the shapes of these modes resemble the shape of an hourglass, and is likely to be found in structured, rectangular meshes. Therefore the used solid models are prone to hourglassing. Hourglassing can be avoided by using fully-integrated solid element formulations. However, these elements are computationally expensive. This is undesired as iterative re-evaluation of the dogbone model is required to obtain the material model (Section 4.3.3).

An alternative to avoid hourglassing is to add internal stiffness to the default element formulation. The introduction of fictitious, non-physical stiffness to avoid hourglassing has a negative effect on the numerical results. Therefore the effect of stiffness-based hourglass control has to be established.

LS-DYNA allows its user to control the amount of added internal stiffness by adjusting the hourglassing coefficient q_h. This coefficient should be high enough to sufficiently counteract the zero-energy modes, yet low enough so that the added stiffness does not significantly influence the results. To determine the value of the coefficient q_h a finite element model of the flat bar tensile test was created using 8-node solid elements with a side length of 1 millimeter. An initial guess of the material model based on the experimental true stress-strain curve up to necking was used. This will be discussed in more detail in Section 4.3. In the middle of the model, at half the gauge length, a thickness reduction of 1% was introduced to trigger the onset of necking.

The finite element model was evaluated for different values of the coefficient q_h using the default solid element formulation. The engineering stress-strain results are presented in Fig. 4.11 and compared to results obtained using fully-integrated 8-node solid elements with selectively reduced integration (solid element formulation -2 in LS-DYNA).

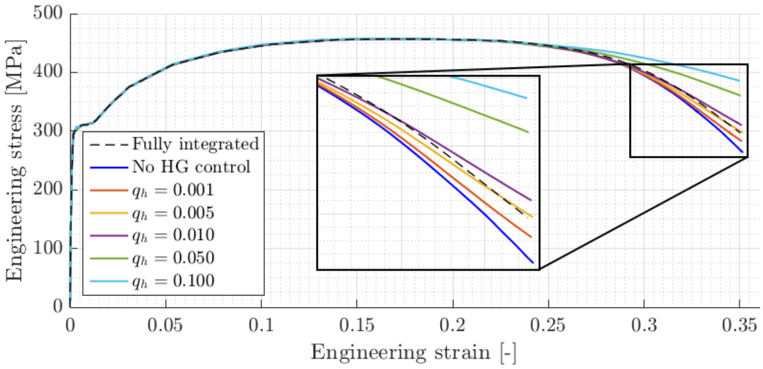

Figure 4.11: Effect of stiffness-based hourglass control on the engineering stress-strain curve

Both element formulations yield results that are in good agreement to each other if no hourglass modes are present in the model. Since hourglassing occurs during the deformation of the current model, the hourglassing coefficient that yields the closest match to the fully-integrated results is sought after. Figure 4.11 shows that hourglassing coefficients of $q_h = 0.005$ and $q_h = 0.010$ provide an equally close match to the fully-integrated element results. An hourglassing coefficient of $q_h = 0.005$ is applied in further finite element modelling, as it adds the least amount of fictitious stiffness, while ensuring proper results.

4.2.2 Element Size

To model the experiments where strain localization precedes fracture a sufficient amount of elements in the necking region is required to accurately describe the geometry of the neck. Since necking typically occurs in tensile tests, the tensile specimen geometry was modelled using several element sizes to study the convergence of the results.

The material model and thickness reduction that were used in the model for the determination of the hourglassing coefficient were once again applied. The previously determined hourglassing coefficient was adopted. Figure 4.12 shows the engineering stress-strain curves that were derived from LS-DYNA by measuring over a gauge length of 60 mm, which corresponds to the tensile experiments. The simulations were stopped when the engineering strain exceeded the experimental engineering strain. The corresponding load paths are depicted in Fig. 4.13.

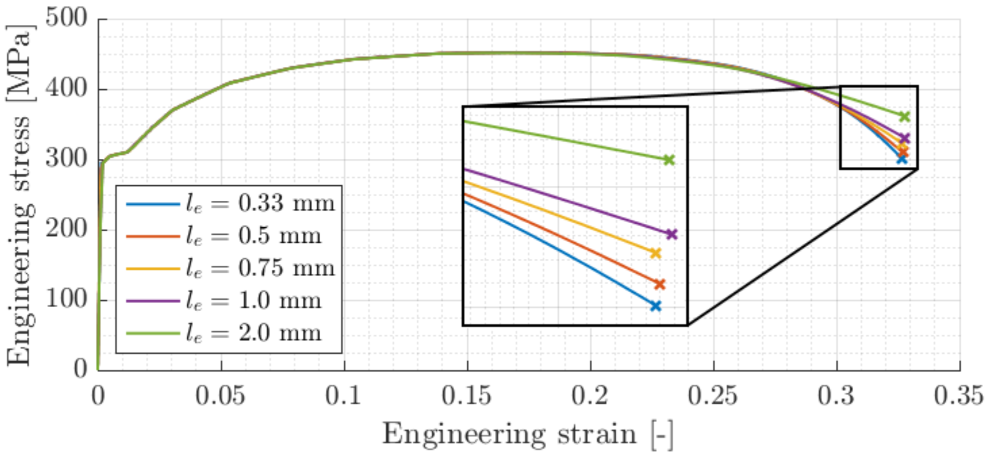

Figure 4.12: Effect of element size on engineering stress-strain curve

The further a neck develops, the finer the elements are required to be to yield accurate results. This can readily be observed from Figure 4.12: the strain is underestimated

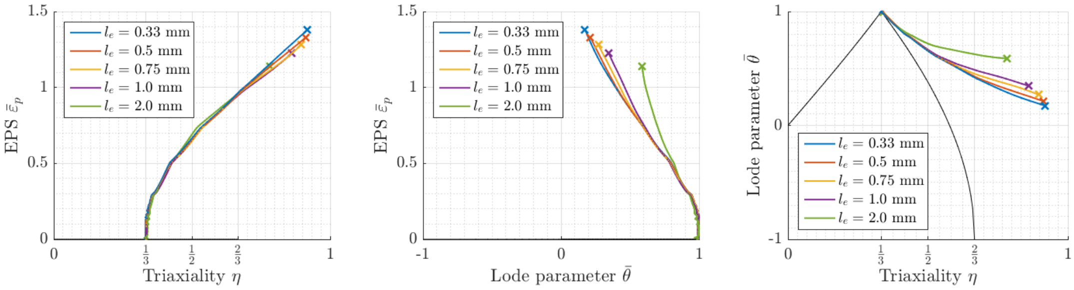

(a) Triaxiality vs EPS (b) Lode vs EPS (c) Triaxiality vs Lode

Figure 4.13: The effect of the element size on the load path

by the larger elements at a earlier stage in the development of the neck. The global engineering stress-strain results converge reasonably well. Locally, however, the strains are not converged: Fig. 4.13 shows the load paths associated with the element in the center of the model, where crack initiation is expected (Section 4.4). The load path results from the smallest element sizes are not in perfect agreement and thus convergence has not been reached. For proper calibration of the fracture models a constant element size across all finite element models of the small scale experiments is required to obtain consistent results. Reducing the element size drastically increases the required computational resources: an element size of 0.5 mm results already in over 200,000 solid elements required to model the circular punch specimens; reducing the element size to 0.33 mm results in over 700,000 elements. Based on the consideration of available computational resources and the observed global convergence an element size of 0.5 mm was selected for the purpose of calibration, even though this causes a slight error in the load path if necking precedes fracture.

4.2.3 Initial Defect

The development of a neck in a finite element model is governed by the presence of an initial defect: in a perfectly prismatic FE-model necking is prohibited due to the alignment of the nodes. As the imperfection in the model due to numerical noise may not be sufficient to trigger the onset of necking, a study was performed to the effect of the size of an initial defect on the necking behaviour. To this goal the thickness of the flat bar tensile model was locally reduced by 0.5%, 1% and 2%. This reduction was applied to all elements at the symmetric plane perpendicular to the loading direction.

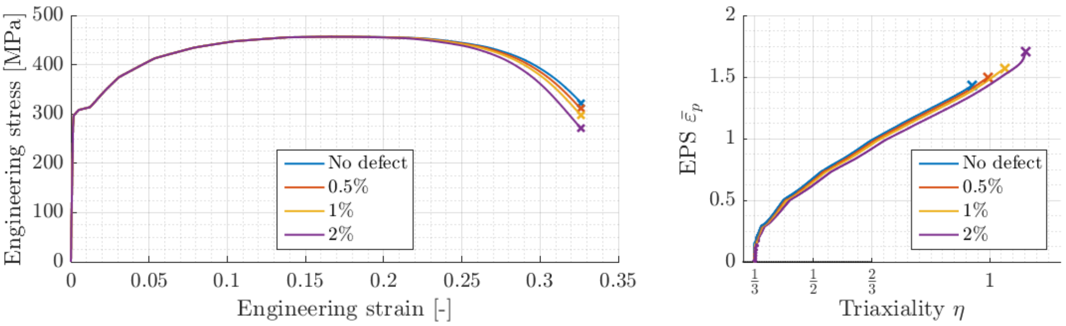

(a) Normalized force-displacement curve

(b) Load path

Figure 4.14: The effect of including an initial defect on the numerical onset of necking

The results of the finite element analysis (Fig. 4.14) are truncated to the point where the engineering strain exceeds the mean experimental engineering strain at fracture. Including an initial defect barely has any effect as long as the straining is uniform. Beyond necking the influence of the initial defect becomes noticeable. The results show that no initial defect is required to trigger the onset of necking: The engineering stress-strain results of having no defect are in good agreement to the those with a 0.5% thickness reduction. Therefore it is concluded that numerical noise in the model is sufficient to trigger necking. On the other hand, including an initial defect has an increasing effect on the equivalent plastic strain at fracture (Fig. 4.14b), which may lead to overestimation of the strain at fracture after calibration. Since including an initial defect has no apparent advantages, no initial defect is included in the hereafter used finite element models.

Note that the results from the model with 1% imperfection are not identical to the results for an element size of 0.5 mm in the previous section: a later iteration of the material model was used to establish the effect of the initial defect (Section 4.3).

4.3 Material Modelling

In this section the procedures to extract the required information from the additional experiments to create the model of the used material are presented. All of the considered fracture models that have been described in Section 3.1 are inherently stress-based fracture criteria that are converted to strain using stress-strain curves in the form of different power law hardening relations. The coefficients of these relations are determined in this section using the results of the flat bar tensile tests. Subsequently, an iterative procedure is used to obtain a more accurate description of the equivalent stress-strain relationship. The material is modelled using the following assumptions, which were explained in Chapter 2:

1. Linear elasticity
2. Von Mises plasticity
3. Associated flow rule
4. Isotropy

4.3.1 Elastic Behaviour

The elastic behaviour is modelled using Hooke's law, which assumes linear, isotropic elasticity. Under these assumptions the elastic behaviour can be fully described by Young's modulus, yield strength and Poisson's ratio. Young's modulus is derived from the engineering stress-strain relation for each of the flat bar specimens. By averaging the results a value of Young's modulus of $E = 216$ GPa is obtained. The yield strength has been determined by using the averaged engineering stress-strain curve, the found Young's modulus and a 0.2% offset strain. The yield strength is found to be $\sigma_y = 298$ MPa. Poisson's ratio has not been determined experimentally and therefore a value of $\nu = 0.3$ is assumed based on recommended practice RP-C208 by DNV-GL [2016].

4.3.2 Power-Law Coefficients

Power-law hardening relations (Eqs. 2.19, 2.20 & 3.18) are used by fracture models to describe the evolution of equivalent plastic strain as a result of equivalent stress. The coefficients of these relations are determined using the results of the flat bar tensile specimen. Before the onset of necking in these specimens (Denoted by a circle in Fig. 4.15), the first principal stress can be approximated by the true tensile stress if the stress distribution on the load-carrying area is assumed to be uniform. The second and third principal stresses in the material are negligible, therefore the equivalent stress is approximately equal to the true tensile stress until necking occurs. As a result, the power-law coefficients can be determined by curve-fitting to the plastic true stress-strain curve before necking obtained from tensile testing. The power law coefficients were found using the least squares method for all power law relations as used by the fracture models.

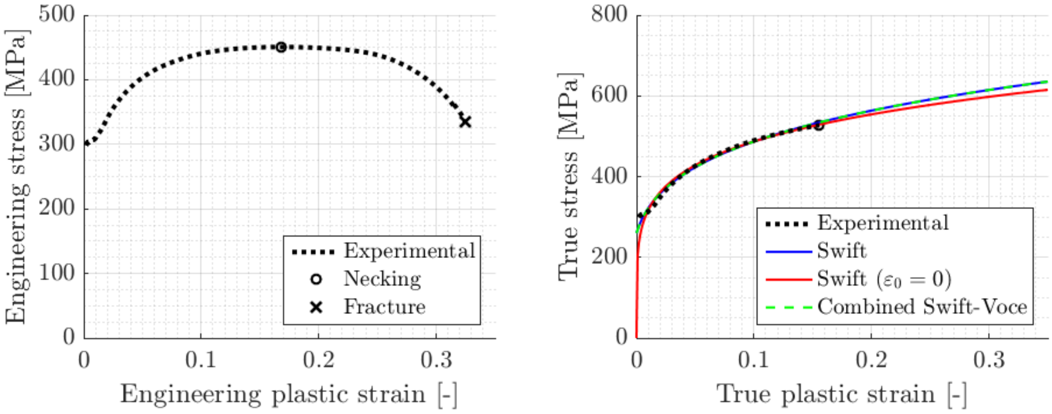

(a) Engineering stress-strain curve (b) Calibrated power-law hardening relations

Figure 4.15: Power law calibration on experimental results

The coefficients of the power laws associated with the curves in Fig. 4.15b are listed in Table 4.4. The combined Swift-Voce curve is collinear with the Swift curve: the contribution of the Voce relation is negligible. This also follows from examination of the coefficients: the small values of k_0 and β eliminate the contribution of the Voce power law. The obtained coefficients are applied in the determination of the shape of the fracture loci in Chapter 5.

The power law coefficient σ_{y0} as used by Xue (Eq. 3.3) is readily obtained from the fitted parameters by using the relation $\sigma_{y0} = K\varepsilon_0^n$.

4.3.3 Inverse Method

A more detailed description of the true stress-strain curve can be obtained by iterative finite element analysis. This method is referred to as the *inverse method*. Each iteration the finite element model of the flat bar tensile test is evaluated in LS-DYNA and the simulated force-displacement curve (FDC) is compared to the experimental one. Subsequently the true stress-strain curve is manually adjusted and the FE-model is re-evaluated. This procedure is repeated until simulated results match the experimental force-displacement curve up to fracture (Fig. 4.17a); the final true stress-strain curve is accepted. Figure 4.16 illustrates the procedure.

Table 4.4: Power law coefficients

Power Law	Coefficient	Value	Unit
Swift	K	798	MPa
	ε_0	$6.17 \cdot 10^{-3}$	-
	n	0.220	-
Swift ($\varepsilon_0 = 0$)	K	748	MPa
	n	0.0186	-
Combined Swift-Voce	α	0.724	-
	k_0	$7.96 \cdot 10^{-12}$	MPa
	Q	0.0801	MPa
	β	$1.16 \cdot 10^{-13}$	-
	K	1102	MPa
	ε_0	$6.17 \cdot 10^{-3}$	-
	n	0.220	-

To start the iteration an initial guess of the true stress-strain curve is required. Since adjusting is done manually, this procedure can be very time-consuming. Therefore a good initial guess is beneficial. In this case the experimental true stress-strain curve was used until necking, beyond necking a linear extrapolation was used as an initial guess. The linear extrapolation between necking and fracture was based on the tensile force at fracture and measurement of the fracture surface.

In hindsight the Swift hardening provides a better initial guess, as it is in better agreement with the accepted stress-strain curve than the linear extrapolation: the Swift power law is capable of describing this specific material's stress-strain curve with surprising accuracy (Fig. 4.17b).

The power-law relations in the considered fracture models can be replaced by a stress-strain curve that was obtained from the inverse method, which provides a more accurate description of the material's behaviour. However, the goal of this thesis is to compare several fracture models rather than to improve them. Therefore no unnecessary adaptations are made and the fracture models are applied in the ways that their authors envisioned: using power law relations.

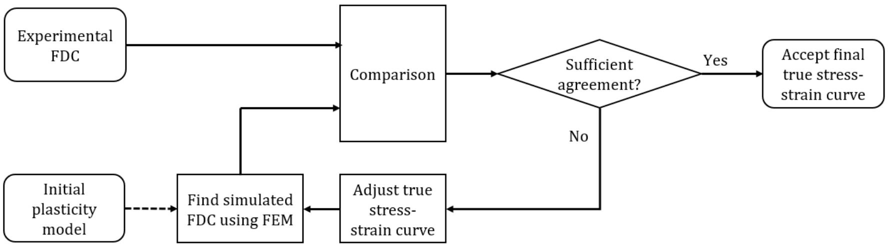

Figure 4.16: Inverse method flowchart

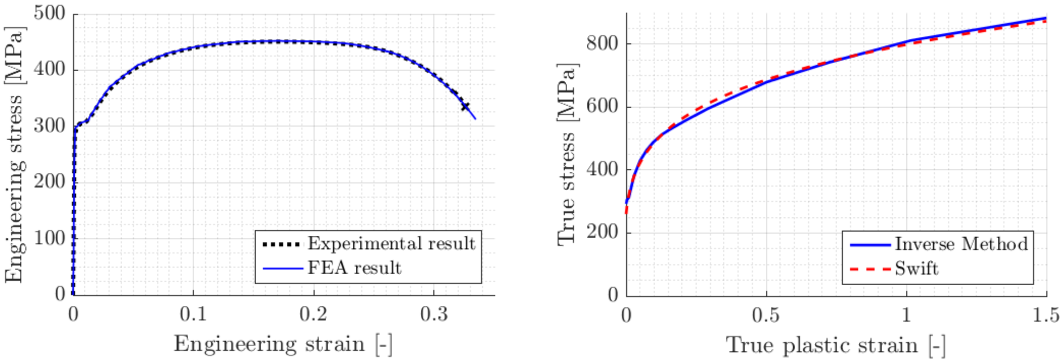

(a) Normalized force-displacement curves

(b) Comparison of stress-strain curves

Figure 4.17: Inverse method results

The normalized force-displacement curve associated with the final material model (Fig. 4.17a) extends past the experimental results: fracture is not included in the current model as the fracture loci have yet to be determined. However, when the FEA results are truncated to the point of fracture, a load path can be obtained to use in the process of calibration. This procedure is discussed in more detail in Section 4.4.

4.3.4 Coefficients of Friction

In the circular punch test and the Hašek tests friction plays an important role. To obtain proper load paths of these experiments for calibration, the displacement field of the specimens in finite element analysis needs to be in good agreement with the experiments. To this goal, the finite element models were tuned using friction coefficients: the friction coefficient between the specimen and the support rings differs from the friction coefficient between the indenter and the specimen, since grease was applied. The friction coefficients were assumed to remain constant during the simulations.

Circular punch friction

The displacement field of the finite element model of the circular punch test was calibrated to the experiments using the experimental radial contraction and the location of fracture. It is assumed that the location of fracture coincides with the location of maximum equivalent plastic strain. In Section 4.4 it is shown that this assumption is valid. The amount of radial contraction in the model is dominated by the support ring friction coefficient, while the location of maximum plastic strain is mainly affected by the indenter friction coefficient: increasing the support ring friction coefficient reduces the radial contraction, and increasing the indenter friction coefficient leads to an increase of the radial distance to the location of maximum plastic strain. However, these effects are not independent and thus iterative tuning of the friction coefficients was required until both the simulated radial contraction and the location of maximum plastic strain match the experimental results.

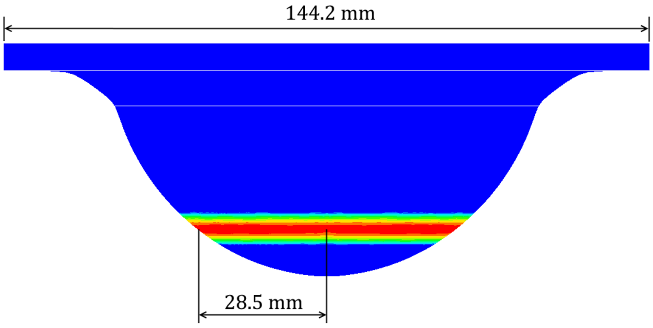

Figure 4.18: Final diameter and radial distance to location of maximum plastic strain (red) of the circular punch model after raising the indenter

The experimental radial contraction was measured post mortem, after the specimen was removed from the experimental setup. Consequently, the measured radial contraction does not equal the radial contraction at fracture, as the specimen showed spring-back after the indenter was raised. This was accounted for in the finite element model by lowering the indenter to the mean experimental indentation at fracture (46.7 mm) and subsequently raising the indenter until there was no more contact.

The friction coefficients were varied with a step size of 0.01. The combination of a support ring friction coefficient of $\mu_r = 0.14$ and an indenter friction coefficient of $\mu_i = 0.19$ were found to yield the best agreement of radial contraction and location of maximum plastic strain to the experimental results (Fig. 4.18 and Section 4.1). Since the specimens and the indenter were greased and the support rings were not, it is not physical that the indenter friction coefficient is lower that the support ring friction coefficient. However, the physical interpretation of these coefficients is inferior to obtaining a correct load path. Therefore these friction coefficients were adopted in the circular punch test model.

Hašek punch friction

Similarly to the circular punch model, the indenter in the Hašek punch model was also lowered to the mean experimental indentation at fracture (26.1 mm) and raised again until the contact was lost. The radial contraction of the model is affected mainly by the support ring friction coefficient, but is not independent of the indenter friction coefficient. The location of maximum plastic strain, however, is independent of the friction coefficients: the maximum is located directly under the indenter at the bottom surface of the specimen (Section 4.4). This is in agreement with the experimental location of fracture. Therefore the indenter friction coefficient cannot be tuned to this model specifically, thus the value obtained from the circular punch test was adopted: $\mu_i = 0.19$.

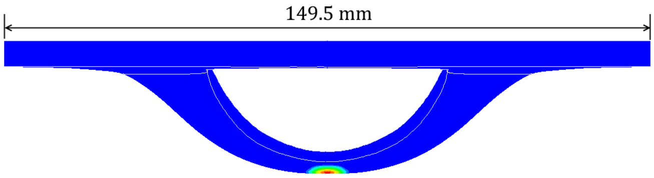

Figure 4.19: Final diameter and location of maximum plastic strain (red) of the Hašek punch model after raising the indenter

The mean experimental radial contraction of the Hašek punch specimens was determined in Section 4.1 to be equal to 0.2 mm. However, the initial diameters of the specimens were not measured and therefore the radial contractions (Table 4.3) were based on the design diameter of 150 mm. Since the final diameter is close to the design diameter, no estimate can be made on the true radial contraction without knowing the initial diameter. If the model was to be tuned to the “experimental” radial contraction of 0.2 mm, an unrealistically high friction coefficient would be obtained. Therefore a more realistic support ring friction coefficient of $\mu_r = 0.35$ is adopted under the assumption that the initial diameters were slightly larger than the design diameter.

4.4 Critical Elements

To calibrate the selected fracture models, the load paths obtained from different experiments are required. More specifically: the load path at the location of crack initiation is required to be known. This location is determined for all small-scale experiments by observing experimental data, aided by finite element analysis. The *critical element* in the FE-models is located at the position in the specimen where crack initiation is expected to occur: a single critical element is determined for each FE-model. These elements provide the load paths that are used for calibration. In this section the procedures of determining the critical elements and obtaining the load paths are presented.

4.4.1 Flat Bar Tensile Test

Before necking the state of stress inside the prismatic part of the flat bar tensile specimens is uniaxial. After the onset of necking, when strains start to localize due to the decrease in load carrying area being larger than the work hardening, the change in geometry alters the state of stress. As a result, tensional stresses in the transverse plane are induced.

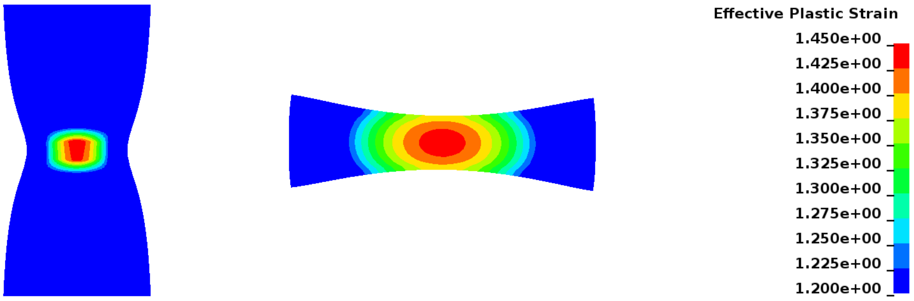

(a) Longitudinal mid-plane section (b) Transverse section at the center of the neck (c) Color scale

Figure 4.20: Equivalent plastic strain distribution in the flat bar tensile FE model

At the surface of the material the plane stress condition is necessarily maintained throughout the deformation process. However, at the center of the neck, this condition is violated after the onset of necking; the transverse tensional stresses result in a local increase of the stress triaxiality. The location of crack initiation is therefore deemed to be at the center of the neck, where both equivalent plastic strain (Fig. 4.20) and stress triaxiality are at a maximum. This is in agreement with the findings by Bao and Wierzbicki [2004] and Hancock and Mackenzie [1976]. The finite element model contained an odd number of elements in all three directions, resulting in the integration point of the critical element being coincident with the location of crack initiation.

4.4.2 Notched Flat Bar Tensile Test

A notch in a uniaxial tensile specimen acts as an initially present neck, causing strain localization to start as soon as the material starts to yield: during the notched flat bar tensile tests no uniform plastic deformation occurred as necking was present as soon as the yield strength was exceeded.

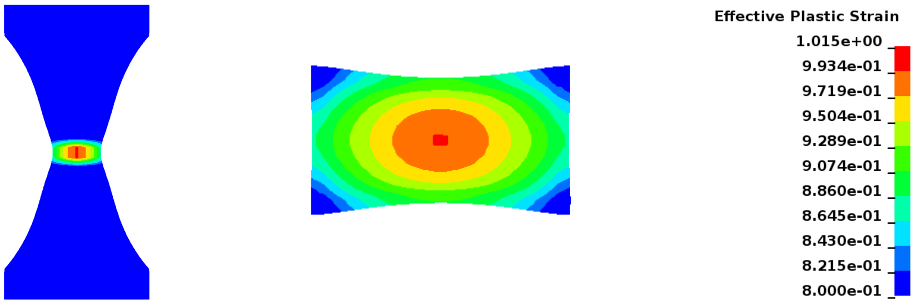

(a) Longitudinal mid-plane section

(b) Transverse section at the center of the neck

(c) Color scale

Figure 4.21: Equivalent plastic strain distribution in the notched flat bar tensile FE model

All remarks from the previous section regarding the states of stress after the onset of necking also do apply to the notched flat bar tensile specimens: fracture initiation occurred at the center of the neck where the locally the stress triaxiality and equivalent plastic strain are the highest (Fig. 4.21). The critical element in the finite element model was once again located at the center of the smallest cross-section.

4.4.3 Circular Punch Test

During the circular punch tests, significant friction was present, causing crack initiation to not occur at the apex of the dome of the indented specimen, but rather at some distance in the radial direction. In Section 4.3.4 the friction coefficients required for the modelling of the punch test were determined based on the location of the crack in the specimens: the location of maximum equivalent plastic strain in the FE model (Fig. 4.22) was matched with the mean experimental location of crack initiation. However, analysis of the state of stress is required to determine the location of the critical element.

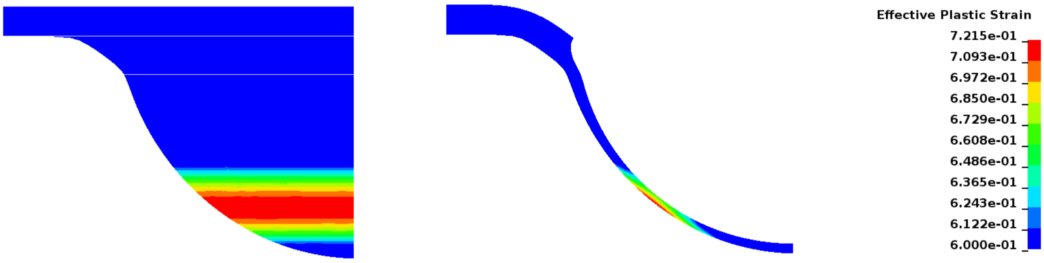

(a) Side view (b) Mid-plane section (c) Color scale

Figure 4.22: Equivalent plastic strain distribution in the circular punch FE model

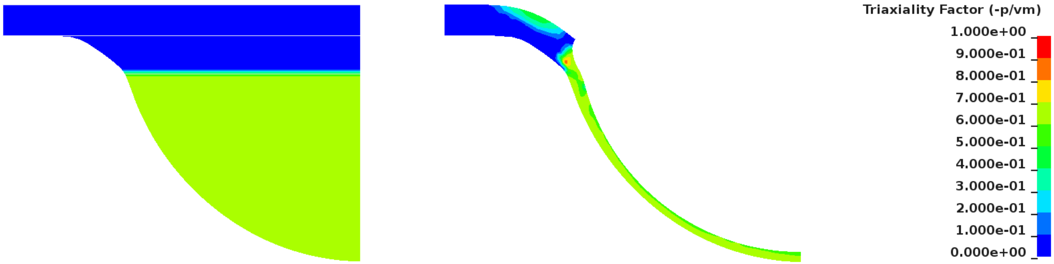

(a) Side view (b) Mid-plane section (c) Color scale

Figure 4.23: Stress triaxiality distribution in the circular punch FE model

The stress triaxiality is approximately constant across the outer surface of the indented region (Fig. 4.23) and has a value that suggests equibiaxial tension. Further inspection of state of stress, however, shows a ring of local increase in Lode parameter, coincident with the location of maximum plastic strain (Fig. 4.24): friction between the indenter and the specimen causes a local increase of the first principal stress (the stress in radial direction, tangent to the surface) at the bottom surface. As a result, the Lode parameter increases, while the triaxiality decreases according to the plane-stress relation (Fig. 2.7).

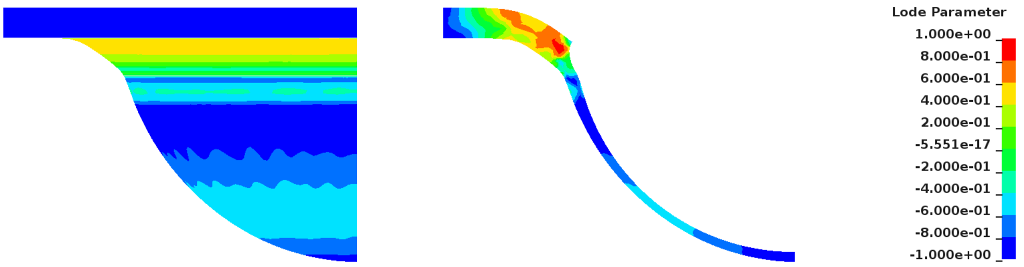

(a) Side view (b) Mid-plane section (c) Color scale

Figure 4.24: Lode parameter distribution in the circular punch FE model

4.4.4 Hašek Punch Test

As opposed to the circular punch results, fracture in the Hašek tests occurred at the center of the specimens. The cutouts of the Hašek specimens were circular, resulting in a minimum of the load-carrying area at the center. At this location plastic strain started to localize as soon as the the yield strength was exceeded.

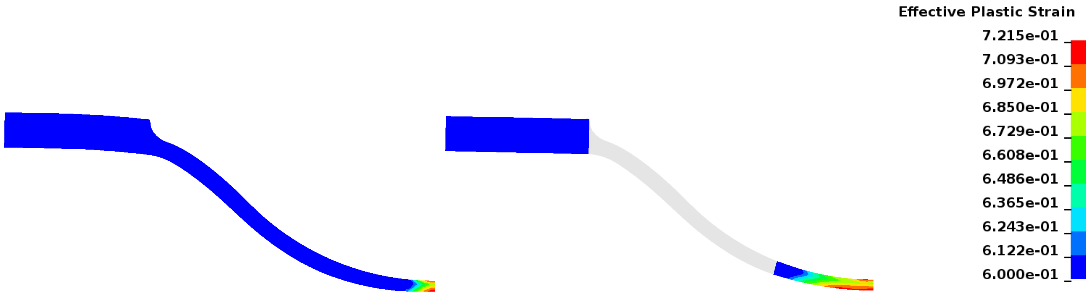

(a) Section view between notches (b) Section view across notches (c) Color scale

Figure 4.25: Equivalent plastic strain distribution in the Hašek punch FE model

During the deformation process the stresses at the bottom of the specimen were higher than the stresses at the indenter-contact surface due to bending of the specimen around the indenter. As a result, the plastic strain had a maximum at the bottom surface of the specimen directly underneath the apex of the indenter (Fig. 4.25). The element at this location was selected as critical element.

4.4.5 Load Paths

After extracting the stress and strain histories from LS-DYNA, the load paths of the critical elements in terms of stress triaxiality, Lode parameter and equivalent plastic strain are obtained according to the relations presented in Chapter 2.

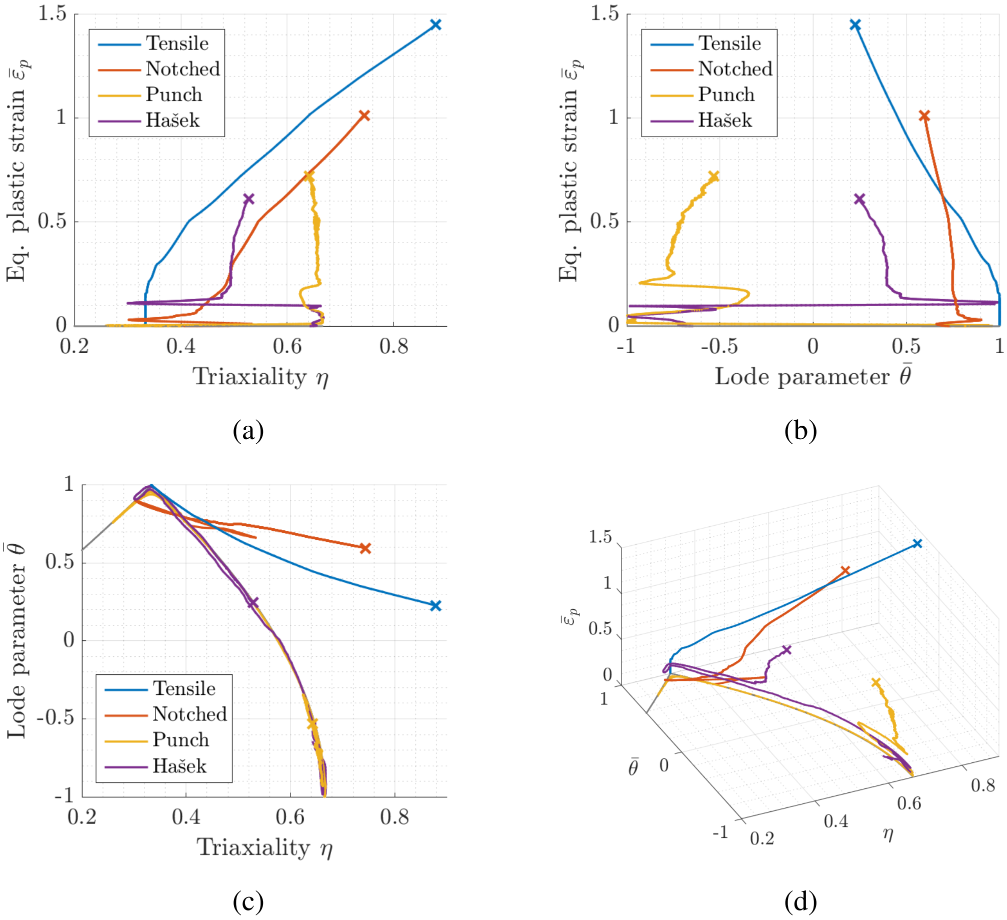

(a) (b)

(c) (d)

Figure 4.26: Load paths of critical elements from the small-scale experiments for calibration

Each small-scale experiment provides one load path. The load paths of the different experiments are depicted in Fig. 4.26 from multiple perspectives. The load paths of the punch and Hašek tests follow the plane-stress relation of triaxiality and Lode parameter, since their critical elements are located at the surface. The plane-stress condition in the notched and unnotched flat bar tensile tests is violated as soon as necking is incipient.

These four load paths are used in the subsequent chapter to calibrate the fracture models to S235 structural steel.

Chapter Summary

In this chapter four small scale experiments have been presented that have been conducted to obtain information on the material's behaviour. The material was modelled after the theory presented in Chapter 2. The approaches that were used to define the material model were presented in this chapter, along with the results that subsequently can be used in the analysis of the large scale experiment (Chapter 6). Finally, the load paths for calibration were determined in this chapter based on analysis of critical elements.

Chapter 5

Application of Failure Models

Several steps are required before a failure model can be used in the finite element package LS-DYNA. First, the failure models need to be calibrated on the examined material. Secondly, the calibrated failure models require correct implementation in the finite element package. In the course of this research, first a method for the implementation of the failure models was required that does not depend on a user-defined subroutine, as was posed as a criterion in Chapter 1. Subsequently the failure models require calibration to make them compatible with the method of implementation. This chronological order is maintained in this chapter: First the implementation is presented, succeeded by the calibration of failure models.

5.1 Implementation

Using the *MAT_ADD_EROSION keyword in LS-DYNA a failure criterion with both triaxiality and Lode dependency can be added to any material. This keyword is based on the GISSMO (*Generalized Incremental Stress State dependent damage MOdel*), which is LS-DYNA's user-friendly solution to provide the user with many options to add damage and fracture to an already existing material model. This model is used in the current research as it provides the possibility to include stress-state dependent failure in a finite element model without a user-defined subroutine.

5.1.1 Failure models

One of the options of the GISSMO is to include stress-state dependent fracture models in the form of equivalent plastic strain at fracture with dependency on both triaxiality and Lode parameter. Variable load paths during the deformation process up to fracture are accounted for by damage accumulation. The damage calculation in the GISSMO is formulated as:

$$\Delta D = m \cdot D^{(1-\frac{1}{m})} \frac{\Delta \bar{\varepsilon}_p}{\bar{\varepsilon}_f(\eta, \bar{\theta})}. \tag{5.1}$$

Here, the accumulated damage parameter D is the summation of the *damage increment* ΔD. Whenever, during the explicit integration in the time domain, the damage parameter exceeds the critical value of 1, the element is deleted from the finite element model.

The *damage exponent m* requires calibration and therefore the minimum amount of calibration tests is increased by one. This is often undesirable and is readily avoided by setting the damage exponent to unity, reducing Eq. 5.1 to linear damage accumulation as proposed by Johnson [1980], which is presented in Eq. 5.2 for any failure model with triaxiality and Lode dependency.

$$\Delta D = \frac{\Delta \bar{\varepsilon}_p}{\bar{\varepsilon}_f(\eta, \bar{\theta})} \tag{5.2}$$

Using this formulation, the damage increment over each timestep is assumed to be proportional to the increase in effective plastic strain and depends on the predicted effective failure strain as a function of the current stress state. The total damage to each element can subsequently be computed by taking the sum of the damage increments:

$$D = \sum_{\bar{\varepsilon}_p=0}^{\bar{\varepsilon}_p} \Delta D. \tag{5.3}$$

Element deletion occurs when the damage variable D exceeds the critical value of 1. It can be seen that for a constant load path the equivalent strain at fracture is coincident with the fracture locus. For varying load paths, the equivalent strain at fracture is not necessarily coincident with the fracture locus, since the entire load path is accounted for in the damage calculation.

The fracture locus, a continuous function, is discretized and tabulated in MATLAB and the results are formatted to an LS-DYNA input file using the keywords *DEFINE_CURVE and *DEFINE_TABLE. The discretized fracture locus is linked to the GISSMO by using the identification number from *DEFINE_TABLE as an input for the variable LCSDG on card 3 of the *MAT_ADD_EROSION keyword. This variable interprets the table and curves as a fracture locus in the space of η, ξ and $\bar{\varepsilon}_f$ and interpolates between the data points. An example keyword file, generated in MATLAB, can be found in Appendix G. A validation towards the implementation of the failure models in LS-DYNA is included in Appendix H.

5.1.2 Conversion

To combine a fracture locus with a forming limit diagram according to the theory presented by Walters [2014], first the FLD needs to be converted to the space of triaxiality and equivalent plastic strain; the Lode parameter is dependent on the triaxiality due to the FLD's inherent plane stress assumption (Eq. 2.10). The required steps to convert $(\varepsilon_1, \varepsilon_2)$ to $(\eta, \bar{\varepsilon}_p)$ are herein presented.

Lee [2005] presented a clear overview of conversion between the FLD and the space of triaxiality and equivalent plastic strain based on the assumptions of plane stress, conservation of volume and von Mises plasticity. The relation between stress ratio $\beta = \sigma_2/\sigma_1$ and the strain ratio $\alpha = \varepsilon_2/\varepsilon_1$ is obtained from Hencky's equations (Eq. 2.22) and is given by:

$$\beta = \frac{2\alpha + 1}{2 + \alpha}. \tag{5.4}$$

The equivalent plastic strain in terms of the strain ratio is given in Eq. 2.17. The stress triaxiality (Eq. 2.5) can be expressed in terms of the stress-ratio β by:

$$\eta = \frac{1}{3}\frac{1 + \beta}{\sqrt{1 - \beta + \beta^2}}. \tag{5.5}$$

A more complete overview of the procedure of conversion is depicted in Fig. 5.1.

After conversion the necking model and fracture model are represented in the same space, making them eligible for application in the framework by Walters [2014].

An example conversion of the BWH necking model is depicted in Fig. 5.2. Note that the dashed lines correspond between the figures and indicate uniaxial tension, plane strain and equibiaxial tension.

5.2 Calibration

As discussed in Chapter 2 both a calibrated forming limit diagram from a necking model and a fracture locus from a fracture model are required in order to predict fracture in a large shell elements. In this section methods for finding the FLDs from the selected

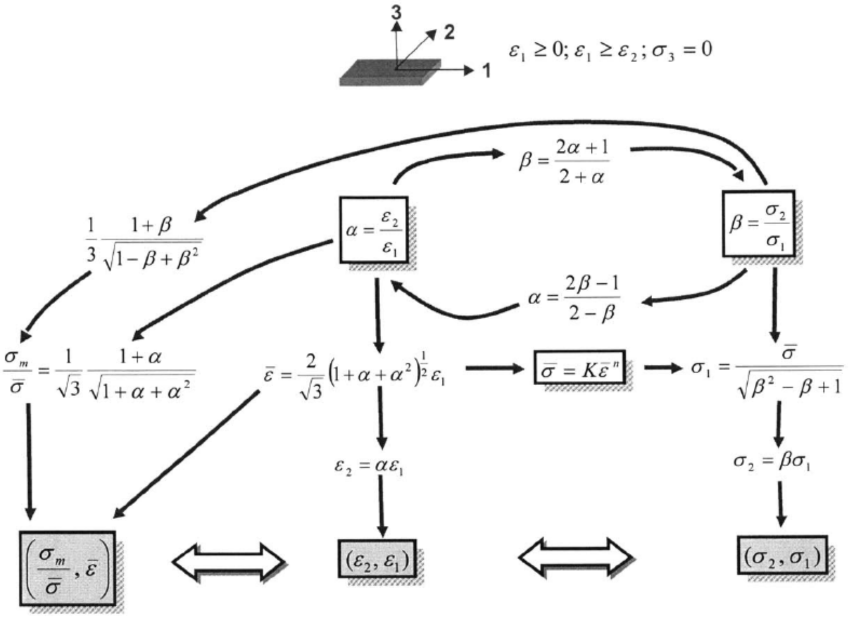

Figure 5.1: Conversion of failure loci between spaces. From Lee [2005]. Corrected.

necking models and the fracture loci from the selected failure models are presented. The current goal is to successfully determine the FLDs and fracture loci for S235 structural steel using the small scale experiments, so that a prediction of the behaviour of the large scale experiment can be made. The material models and load curves used for calibration were presented in Chapter 4.

5.2.1 Fracture Loci

To be able to use a fracture model in the finite element method, first the calibration parameters of the model need to be determined. To this goal, a set of small scale calibration experiments was conducted. The amount of calibration experiments used to define the locus must be equal or exceed the amount of calibration parameters in the failure model. Fewer experiments than calibration parameters results in a under-determined system of equations.

A common and simple approach to calibrating a fracture locus is to obtain the averaged Lode and stress triaxiality parameters from finite element analysis. These two values, along with the equivalent strain at fracture, define a single point on the fracture locus. Repeating this procedure for all experiments yields a set of points through which

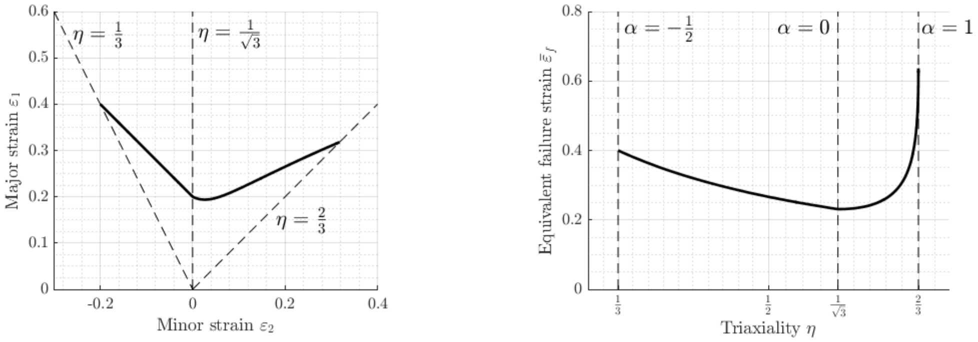

(a) Original FLD space

(b) Converted space

Figure 5.2: Example conversion of Bressan-Williams-Hill locus with $n = 0.2$

the fracture locus is curve-fitted.

The previously described calibration method serves as an illustration. It is, however, not very accurate due to the averaging of the load path. To overcome this problem, a procedure is herein proposed that assumes a damage evolution function in the form of Eq. 5.2. As a result, no information on the triaxiality and Lode parameter histories is ignored in the determination of the fracture locus. This method is henceforth referred to as *Variable Load Path Calibration* (VLPC) and is similar to the calibration approach used by Mohr and Marcadet [2015]. In this section the VLPC procedure is described.

A script has been produced which finds the calibration parameters by minimizing a set of functions using the least squares approach. A validation of this approach is presented in Appendix I. Using the load paths derived from analysis of the small scale experiments (Section 4.4), the different fracture loci can be calibrated to the material of the large scale experiment.

Variable Load Path Calibration

To incorporate the damage evolution into the VLPC procedure, the damage as a function of the fracture model and its calibration parameters is required. To this goal, the fracture models' shape functions are rewritten to a function of the calibration parameters (Eq. 5.6).

$$\bar{\varepsilon}_F(\eta,\bar{\theta}) \rightarrow \bar{\varepsilon}_F(\mathbf{C},\eta,\bar{\theta}) \tag{5.6}$$

Here, $\mathbf{C}$ is the array that holds all of the fracture model's calibration parameters.

Subsequently, an expression for the damage can be derived from Eqs. 5.2 & 5.3. The obtained expression is in the form of the left-hand part of Eq. 5.7:

$$D(\mathbf{C}, \bar{\varepsilon}_p, \eta, \bar{\theta}) \rightarrow D_i(\mathbf{C}) \ , \quad i = 1, 2, ..., N_{\text{exp}}. \tag{5.7}$$

The right-hand side is the result of the load path substitution and is a system of N_{exp} equations, where N_{exp} is the amount of experiments used for calibration. Fracture is associated with a damage parameter value equal to 1. Using this information, a minimization problem is defined by Eq. 5.8. This set of equations is referred to as the *damage functions*:

$$f_i(\mathbf{C}) = D_i(\mathbf{C}) - 1. \tag{5.8}$$

The VLPC procedure has been implemented in MATLAB. The system of equations in Eq. 5.8 is solved using the least squares approach. This yields a set of calibration parameters for which the damage variables associated with the calibration experiments are closest to unity.

The validity of this procedure has been studied and is elaborated in Appendix I. The validation study of the VLPC procedure shows that proper results are obtained when a suitable initial guess of the calibration parameters is adopted. Boundary values of the initial guess for the calibration parameters were suggested, which are listed in the following 5.1.

Table 5.1: Proposed initial guess domain

Fracture Model	Parameter	Lower limit	Upper limit	Unit
Xue	σ_{F_0}	350	1500	MPa
	k_p	$4.2 \cdot 10^{-6}$	10^{-3}	MPa^{-1}
Modified Mohr-Coulomb	c_1	10^{-4}	0.2	-
	c_2	150	600	MPa
Hosford-Coulomb	a	0.3	1.76	-
	b	100	1500	MPa
	c	10^{-3}	0.2	-

The values listed in this table have been obtained from an analysis based on fracture loci calibrated on materials similar to S235. Therefore the proposed domain of initial guess is not necessarily adequate for all types of steel.

Calibrated parameters

Calibration of the three selected fracture models has been done using the method described in the previous section. For each model, several sets of initial guesses for the calibration parameters were used. These sets were spread across the proposed initial guess domain (Table 5.1). The results of all initial guesses are presented in Tables 5.2 to 5.5 for all fracture models.

Table 5.2: Xue calibration

		σ_{F_0} [MPa]		
		400	800	1200
k_p [MPa^{-1}]	10^{-5}	Pass	Pass	Fail
	10^{-4}	Pass	Pass	Pass
	10^{-3}	Fail	Pass	Pass

Table 5.3: MMC calibration

		c_1 [-]		
		10^{-3}	10^{-2}	10^{-1}
c_2 [MPa]	200	Pass	Pass	Pass
	400	Pass	Pass	Pass
	600	Pass	Pass	Pass

Table 5.4: HC calibration ($a = 0.1$)

		b [MPa]	
		500	1000
c [-]	10^{-2}	Pass	Pass
	10^{-1}	Pass	Pass

Table 5.5: HC calibration ($a = 0.2$)

		b [MPa]	
		500	1000
c [-]	10^{-2}	Pass	Pass
	10^{-1}	Pass	Pass

These tables depict the outcome of the VLPC procedure for different combinations of initial guesses for the individual calibration parameters. Each *Pass* refers to finding the set of calibration parameters in Table 5.6. *Fail* indicates the VLPC procedure not finding a local minimum, and therefore not yielding any results. Finding calibration parameters that deviate from the values in Table 5.6 did not occur, therefore the values in this table are adopted.

From the calibrated parameters it can be seen that the models based on Mohr-Coulomb become purely dependent on the deviatoric part of stress: Coefficients c_1 and c, belonging to MMC and HC respectively, are equal to zero and therefore the models

Table 5.6: Calibrated Parameters

Fracture Model	Parameter	Value	Unit
Xue	σ_{F_0}	909	MPa
	k_p	$7.31 \cdot 10^{-5}$	MPa^{-1}
Modified Mohr-Coulomb	c_1	0	-
	c_2	410	MPa
Hosford-Coulomb	a	0.474	-
	b	1241	MPa
	c	0	-

forego their dependency on pressure. This is mainly caused by the high stress triaxiality at fracture in the flat bar tensile test. Moreover, the MMC criterion is reduced to a maximum shear criterion because of this. This is in agreement with the findings in Pack and Mohr [2017], where it is stated that, for the HC model, the coefficient c, associated with the internal angle of friction (Eq. 3.9), is negligible in biaxial tension. The Xue model is inherently different as it is not based on the Mohr-Coulomb criterion and still retains some pressure dependency in the form of k_p.

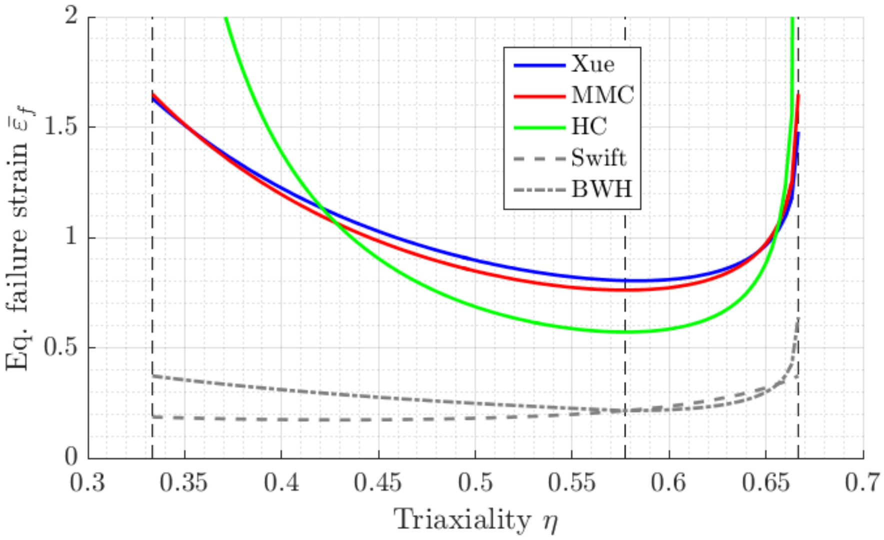

Figure 5.3: Calibrated loci

A graphical representation of the necking loci and the fracture loci is given by Fig. 5.3 for in-plane tensional states of stress.

5.2.2 Necking models

Calibration of the necking models is more straight-forward than calibration of fracture models: the necking models are expressed in terms of power law hardening parameters and therefore require no separate calibration procedure. These parameters are listed in Table 4.4. Inserting these in the formulations of the necking models presented in Chapter 3 yields the necking loci in the space of major and minor strains. Applying the conversion technique from Lee [2005] (Section 5.1.2) enables the necking loci to be combined with the fracture loci.

5.2.3 Element Size Dependency

In Section 2.3.3 the framework by Walters [2014] was presented to account for element size dependency on fracture strain of shell elements due to their inability to describe the state of stress inside a neck. The theory states that the fracture strain can be described by a linear combination of a necking locus and a fracture locus, making use of a scaling parameter γ, which is a function of element size. Unfortunately, problems arise if calibration of the fracture locus was done using fine solid elements: if the element size is small enough that the solution is converged, then further reducing the element size has no effect on the fracture locus obtained from calibration a fracture model. However, the scaling factor γ is affected by the smaller element size used for calibration. This is illustrated in Fig. 5.4, where the thickness equals the calibration thickness and calibration was done using different but converged element sizes.

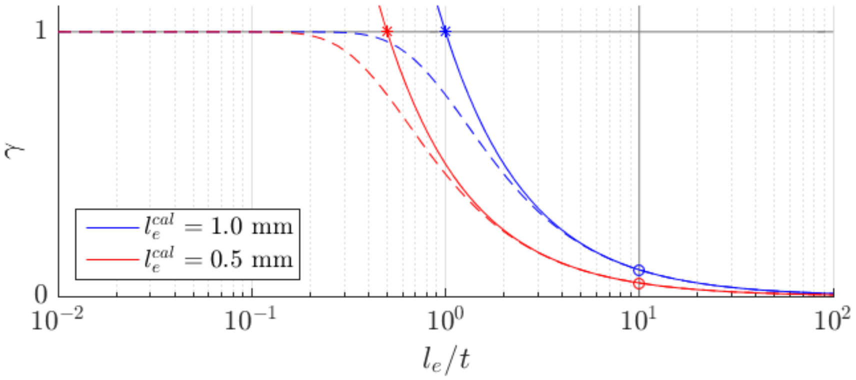

Figure 5.4: Effect of element size used for calibration on weighting factor γ

The continuous lines in this figure depict the scaling factor γ based on two converged element sizes used for calibration (The red and blue asterisks). If one were to apply this theory to obtain the equivalent strains at fracture for an element size of $l_e = 10t$ then inconsistent values of γ are obtained (The red and blue circles). Therefore a modification to Walters' framework is herein proposed: an alternative shape function for element-size dependency $\gamma(l_e)$ is employed, which is based on the assumption that for fine solid elements fracture strain converges to the fracture locus, and for large solid elements the fracture strain converges to the necking locus. A suitable formulation is presented in Eq. 5.9 and is depicted by the dashed lines in Fig. 5.4:

$$\gamma = \tanh\left(c_1 \left[\frac{t}{l_e}\right]^{c_2}\right). \tag{5.9}$$

This formulation includes two coefficients c_1 and c_2 that are required to calibrate the shape function: the coefficients capture the element size dependency in the transient zone for intermediate element sizes ($l_e/t \approx 1$). These coefficients adjust the horizontal position and the slope of the hyperbolic tangent and need to be determined, for instance by using finite element analysis or digital image correlation data.

An element size of $l_e/t \geq 1$ results in a single element through thickness if solid elements are used to model plate material, causing the results from finite element analysis to be similar to results obtained using shell elements of equal size. Based on this consideration, the herein suggested theory provides a solution of applying a fracture locus calibrated on solid elements to predict fracture in shell elements.

To achieve successful calibration of this shape function (Fig. 5.4), at least two values of scaling factor γ associated with two different element sizes are required to determine the two calibration parameters in Eq. 5.9. To this goal, the effect of the element size on the scaling factor γ was determined using the finite element model of the flat bar tensile test. Using the nodes in the FE model several *virtual elements* have been determined. Initially, all virtual elements were square, determined by four nodes that are equidistant to the center of the neck. Figure 5.5a depicts the smallest and largest virtual elements and their nodes in a deformed state. The length of the largest virtual element was equal to the width of the specimen (20 mm). Using the nodal displacements and their initial positions, the virtual strain histories were determined. Subsequently, the conversion by Lee [2005] (Fig. 5.1) was used to obtain the stress triaxiality and equivalent plastic strain, defining the virtual load paths.

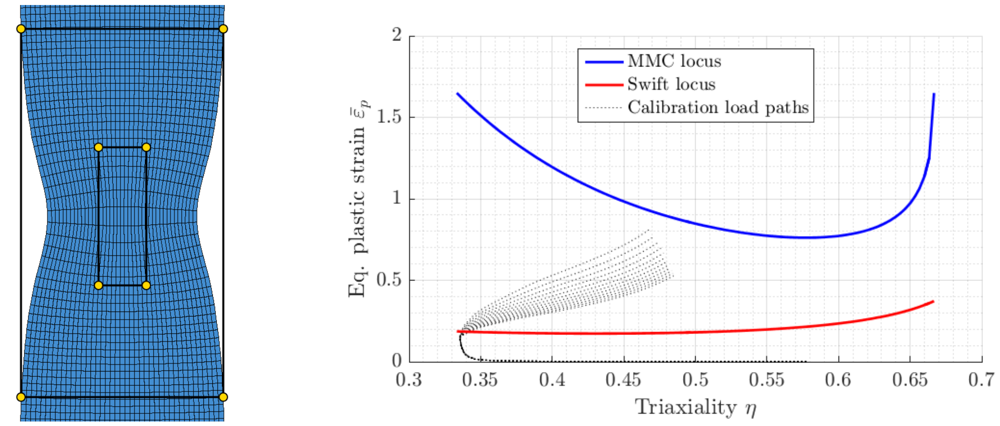

(a) Smallest and largest virtual element

(b) Failure loci and load paths for finding γ

Figure 5.5: Calibration method for element-size dependent failure

For each virtual load path (the dotted lines in Fig. 5.5b), associated with a certain virtual element size, the value for γ is determined by applying inverse damage accumulation (Section 5.2.1) to the linear combination of the failure loci (Eq. 2.28). Note that the values of γ are therefore not only dependent on the element size, but also on the fracture and necking loci. The coefficients in the element-size-dependency shape function (Eq. 5.9) are readily obtained by curve-fitting to the pairs of γ and l_e obtained from the virtual elements (Fig. 5.6).

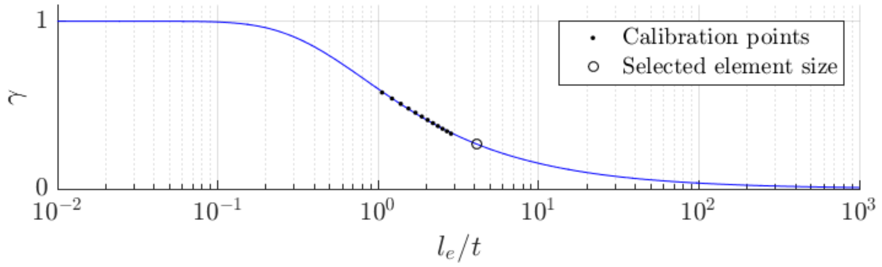

Figure 5.6: Calibrated shape function for the combined MMC-Swift locus

Now that the calibration coefficients of the shape function are known, the obtained *S-curve* relation between the scaling factor γ and the element size can be used to determine the combined failure locus. This procedure was repeated for all combinations of fracture and necking loci.

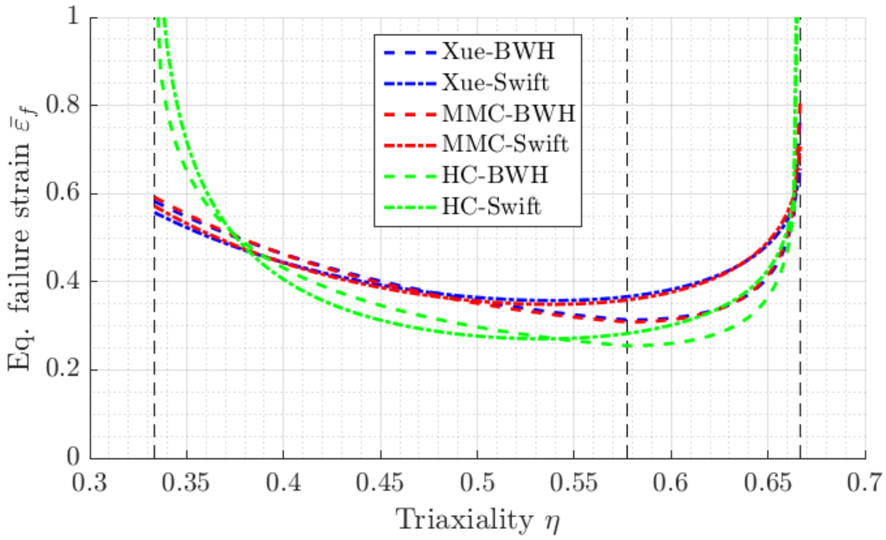

Figure 5.7: Combined loci

It is important to realize that the scaling factor is unique for each combination of a necking locus with a fracture locus. The height of the combined locus is highly affected by the load paths on which the the S-curve was calibrated. However, the shape of the combined locus highly depends on the shapes of the original necking and fracture locus. The calibrated MMC and Xue loci show large similarity (Fig. 5.3). As a result, combination of either of these loci with a necking model produces very similar loci. This can clearly be observed from Fig. 5.7, where the Xue-BWH locus is almost coincident with the MMC-BWH locus. The same is obviously true for the combinations with the Swift necking locus.

5.2.4 Practical approach

To be able to make statements on the performance of the combined failure loci with respect to a more practical approach that requires only a single calibration experiment, the Modified Mohr-Coulomb model was re-calibrated using the circular punch only: Voormeeren et al. [2014] has shown that the Modified Mohr-Coulomb coefficients c_1 and c_2 are related to each other for in-plane tensional states of stress. This means that only the height of the plane-stress MMC locus is scaled by the calibration parameters, without affecting the shape. Therefore $c_1 = 0$ was chosen freely, while c_2 was calibrated on the circular punch test in two ways:

1. using the variable load path calibration procedure (Section 5.2.1)
2. using the equivalent strain at fracture and assuming equibiaxial tension throughout the deformation process

For the second method, the equivalent failure strain can be obtained from FEA, DIC or post-mortem thickness measurements. For the punch test no DIC was available. The results from FEA are in good agreement with the thickness measurements: the obtained strains at failure were $\bar{\varepsilon}_f = 0.72$ and $\bar{\varepsilon}_f = 0.71$ respectively.

For the VLPC procedure $c_2 = 380.5$ MPa is obtained. Ignoring the stress-state history and assuming equibiaxiality yields $c_2 = 351.8$ MPa. These parameters lead to predicted failure strains of $\bar{\varepsilon}_f = 0.513$ and $\bar{\varepsilon}_f = 0.332$ in plane-strain tension. Even though both loci are calibrated using the punch test only, the results cause a large difference between the fracture loci due to the assumption of equibiaxiality.

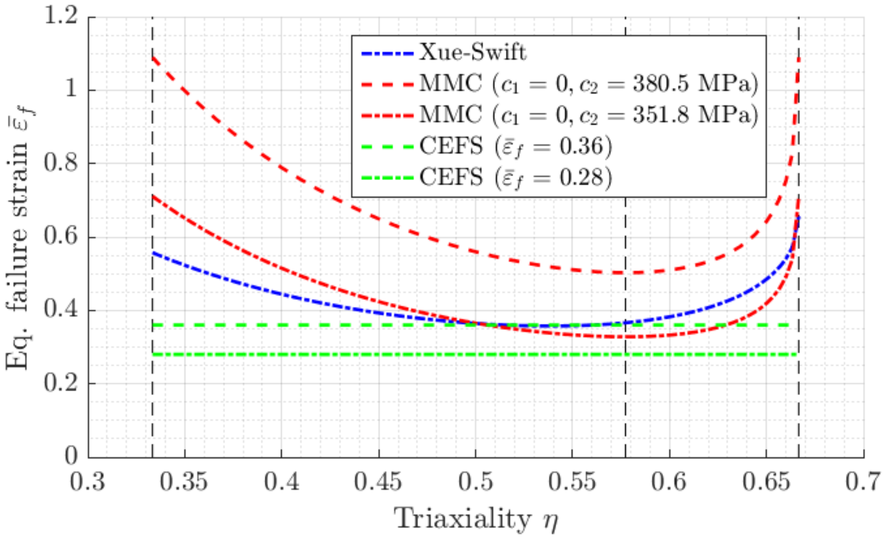

Figure 5.8: Single-parameter failure loci

The most common approach to predict failure is by assuming a constant value of the equivalent plastic strain at failure, therefore foregoing all dependency on stress-state and element size. The constant equivalent failure strain (CEFS) was obtained from the material certificate ($\bar{\varepsilon}_f = 0.36$, Appendix B) and from the flat bar dogbone test ($\bar{\varepsilon}_f = 0.28$, Section 4.1). Both values are different, even though both are obtained from tensile testing: the gauge length of the extensometer has a large influence on the failure strain due to the presence of a neck. All herein presented failure loci are depicted in Fig. 5.8, along with the combined Xue-Swift locus for comparison.

Chapter Summary

In this chapter a method was presented that allows implementation of failure models into LS-DYNA without requiring a user-defined subroutine. Subsequently, a method to convert necking models from the space of $(\varepsilon_1, \varepsilon_2)$ to $(\eta, \bar{\varepsilon}_p)$ that is required for the application of necking models was introduced. Lastly, the calibration methods for the failure models have been presented, as well as a new technique for including element size dependency. This technique was applied to all possible combinations of necking and fracture loci to obtain six combined failure loci. These will be applied to the finite element model in the next chapter.

Chapter 6

Experimental Validation

In this chapter the raking damage experiment conducted by Stan Haag (Haag et al. [2017], Haag [2017]) is presented. This experiment is used for experimental validation of the work presented in the previous chapters of this thesis. Validation obviously requires a finite element model. The details of this model are also presented in this chapter. Subsequently, the results of both the experiment and of the finite element analysis are compared to each other and the results are discussed.

6.1 Raking Damage Experiments

The experiment was designed by Haag to mimic a raking-damage scenario where a ship collides with a submerged rock as often occurs during ship grounding. The raking-damage specimens were created from the same plate of S235 structural steel as the specimens of the small-scale experiments presented in Chapter 4.

6.1.1 Experiment

The raking-damage experiment was specifically designed for the drop-tower facility in the laboratory of the Structural Dynamics department of TNO in Delft, the Netherlands. A cylindrical indenter with hemispherical ends represents the submerged rock (Fig. 6.1). The indenter was attached to a drop mass of 4575 kg. Directly underneath the drop mass two plate specimens were mounted to a frame under an inclination of 15 degrees with respect to the drop direction, representing the plating in the hull of a ship. Therefore in the experiment the "rock" collides with the "ship". The experiment was designed to be symmetrical to prevent horizontal deflection of the indenter during the experiment.

The frame consists of steel tubes with a square cross-section (140 mm x 140 mm x 12.5 mm). The specimens are attached to the frame at the flanges using five M30 bolts protruding through the frame per flange. The CAD drawings including the dimen-

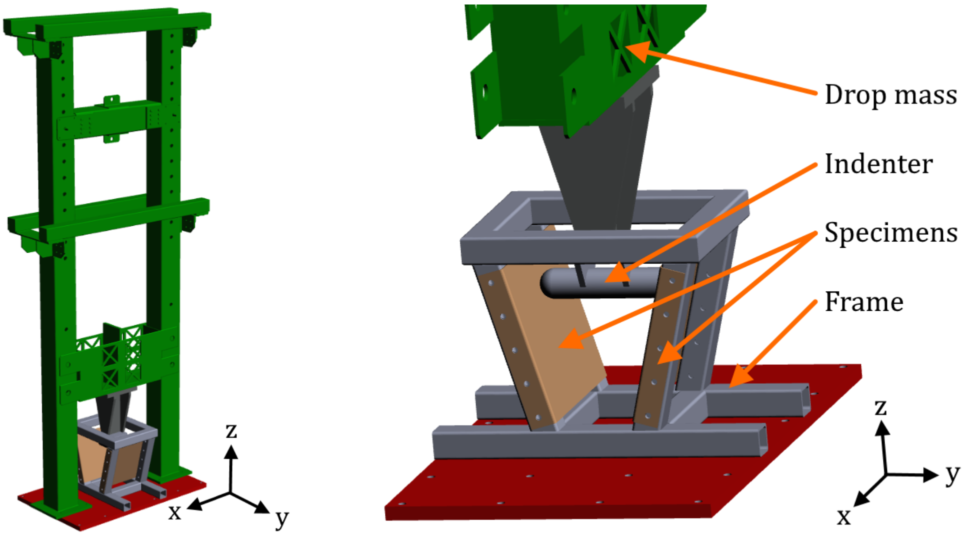

(a) Overview (b) Detailed view

Figure 6.1: Computer-aided design of the experimental setup. Credit: Stan Haag.

sions of the specimens, the frame and the indenter are presented in Appendix J. For further details and properties of the different parts in the experimental setup the reader is referred to the original design presented in Haag [2017].

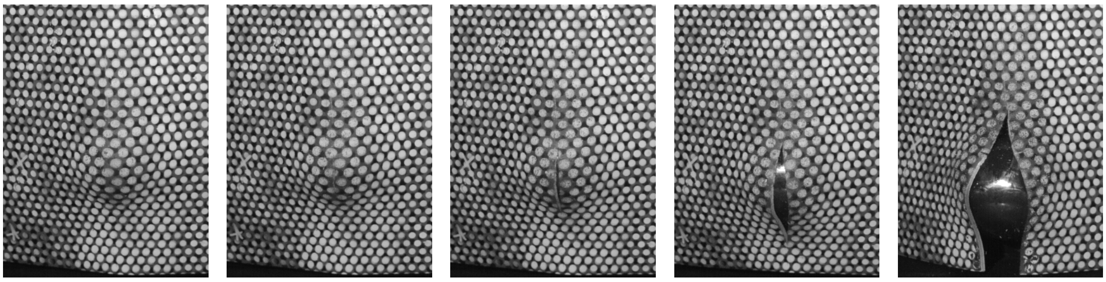

(a) (b) (c) (d) (e)

Figure 6.2: Sequential representation of fracture during the raking damage experiment. Credit: Stan Haag.

At the start of the experiment the drop mass is released and starts to translate downwards (in negative z-direction in Fig. 6.1) under the influence of gravity. The maximum drop height of the setup was approximately 1.5 m. After the indenter has made contact with the specimens, the specimens start to deform and eventually fracture occurs (Fig.

6.2). During the experiments the accelerations of the drop mass were measured using two accelerometers located close to the indenter. The experiment was conducted four times. In the first two experiments the drop height was lower than its maximum and no fracture occurred after a single drop. Consecutive drop tests were performed on the already deformed specimens until either one of the specimens had ruptured; fracture never occurred in both specimens due to a misalignment of 20 mm of the frame relative to the drop tower. In experiments 3 & 4 the maximum drop height was used. Friction in these experiments was reduced by sanding the specimens and applying grease to the contact surfaces of both the specimens and the indenter. These measures ensured that fracture occurred during the first drop.

6.1.2 Finite Element Modelling

The dimensions of the setup of the raking damage experiment are presented in Appendix J; the finite element model has been created accordingly. The finite element model is subdivided in three parts: The specimens (Colored blue in Fig. 6.3), the indenter (green) and the frame (yellow). All parts were meshed using Belytschko-Tsay shell elements with five integration points through-thickness.

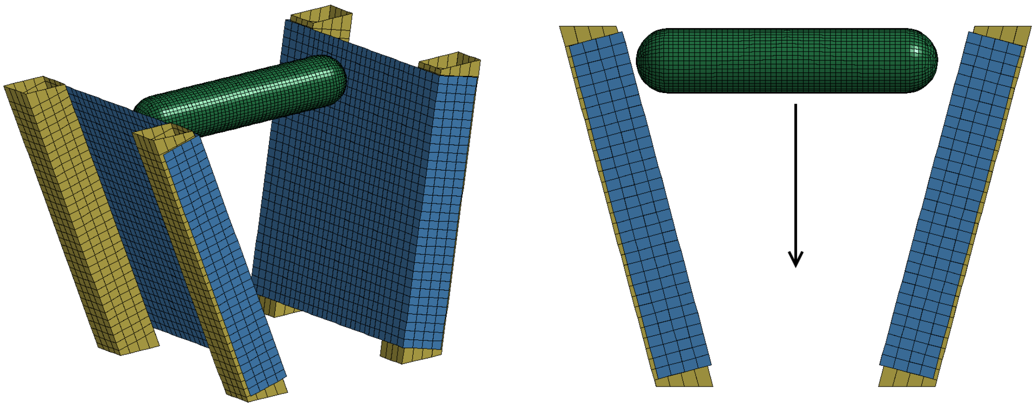
(a) Overview

(b) Front view and drop direction

Figure 6.3: Finite element model of the experimental setup

For the specimens an element size of 25 mm was used. Ideally, elements with a larger length-over-thickness ratio are desired, since this is more common in numerical analysis of maritime collisions. However, using larger elements yields poor results as these are unable to follow the shape of the indenter during the simulation: the element size is limited by the radius of the indenter. A mesh convergence study has not been performed, since obtaining convergence is not a goal: accurate prediction of failure in shell elements is the goal, regardless of whether the mesh is converged. The material model used for the specimens was presented in Section 4.3 and was derived using the flat bar tensile test. For simplicity the bolted connection between the frame and the specimens were not modelled. In stead the nodes located at the ends of the flanges of the plates were constrained in all directions. Interaction between the frame and the plate were treated using a surface-to-surface contact definition. The thicknesses of both the specimens and the frame were accounted for geometrically.

Excluding the frame from the model results in a significant overestimation of the stiffness, which could not be neglected. Therefore the inclined tubes of the frame were added to the model. The mesh of the tubes matches the mesh of the specimens. Fixed boundary conditions were applied on the nodes located at the ends of the tubes. No information on the steel-grade of the frame was available. Therefore a linear elastic material model was adopted with the same elastic properties as the material of the specimens.

For the indenter a rigid material model was used. The part consists of shell elements of negligible thickness. The mass density was tuned so that the total mass of the part was equal to the entire drop mass (4575 kg). Displacement of the indenter in any direction other than the vertical direction was constrained. To account for the misalignment of the experimental setup, a horizontal offset of the indenter of 20 mm was included in the model (Fig. 6.3b). A surface-to-surface contact definition that is suitable in combination with element erosion was applied between the indenter and the specimens. Haag et al. [2017] conducted experiments to determine the friction coefficients for greased steel-on-steel contact. For the same grease that was applied to the raking damage experiments, he observed that the Coulomb friction coefficient during the experiments was fairly constant and he suggested a value of $\mu = 0.03$. This value has been adopted in the finite element model.

6.2 Results

During the experiment the accelerations of the indenter in time were measured. By integration of the acceleration the vertical velocity and displacement of the drop mass are readily obtained:

$$\dot{z} = \int \ddot{z}\,dt \tag{6.1a}$$

$$z = \int \dot{z}\,dt = \iint \ddot{z}\,dt\,dt. \tag{6.1b}$$

Since the measured signal is discrete a trapezoidal integration scheme was used for numerical integration. Using the results from integration the kinetic and potential energies of the drop mass are determined:

$$E_{kin} = \frac{1}{2}m\dot{z}^2 \tag{6.2a}$$

$$E_{pot} = mgz. \tag{6.2b}$$

Due to the law of conservation of energy, the energy dissipated during the experiment is obtained from the kinetic, potential and total energy. No energy is dissipated until the indenter is in contact with the plate. Therefore the total energy is derived from the kinetic and potential energy of the indenter at $t = t_0$ before the indenter strikes the specimens:

$$E_{dis}(t) = E_{tot}(t = t_0) - E_{kin}(t) - E_{pot}(t). \tag{6.3}$$

In this formulation the kinetic energy of the specimens is neglected; finite element analysis shows that this energy is less than 0.1% of the total energy. Unfortunately, the elastic potential energy of the specimens cannot be distinguished from the measurement data and is unavoidably included in the dissipated energy. However, at fracture the elastic strain is small compared to the plastic strain, and therefore the contribution of the elastic potential energy in the specimens in negligible compared to the energy dissipated by plastic deformation. The kinetic energy of the specimens, derived from FEA, did not exceed 0.1% of the total energy, and is therefore also negligible. As a result, the only dominant contributions to the total energy dissipation are caused by friction and by plastic deformation:

$$E_{dis} = E_{fric} + E_{pl}. \tag{6.4}$$

Experiment

The dissipated energy during the deformation process was calculated for the tests where fracture occurred during the first drop: tests 3 and 4. In Fig. 6.4 the energy dissipation during the experiment is plotted against the displacement. This is the absolute displacement of the indenter in vertical direction, starting from an arbitrary height where the indenter was not in contact with the specimens.

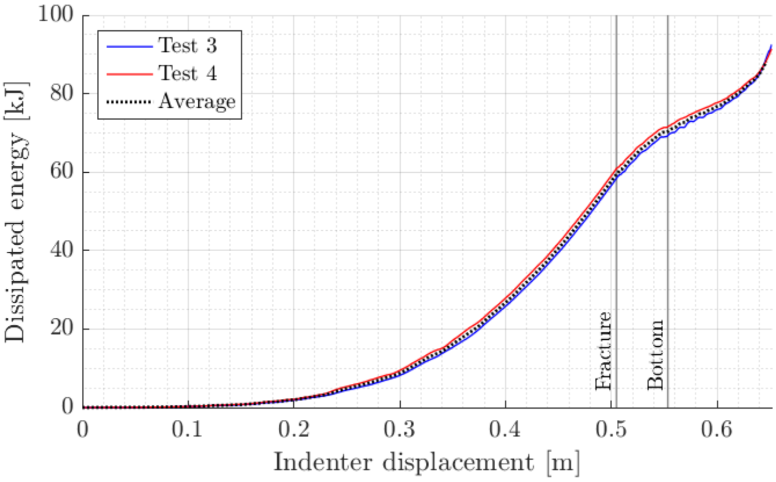

Figure 6.4: Dissipated energy during experiments

The results of test 3 and 4 are in good agreement with each other. Their averaged results are used for validation of the numerical results. The experimental points of fracture were determined in Haag [2017] by synchronization of the acceleration measurements with a high-speed-camera system. The average point of experimental fracture is depicted by the leftmost vertical line in Fig. 6.4. The rightmost vertical line indicates when the indenter first touches a damper mounted underneath the experimental setup.

Finite Element Analysis

The finite element model of the raking damage experiment was evaluated without any failure criterion. The results from FEA are presented together with the experimental results in Fig. 6.5. Rather than obtaining the dissipated energy directly from the post-processor, the dissipated energy from FEA has been calculated in the same way as the experimental dissipated energy.

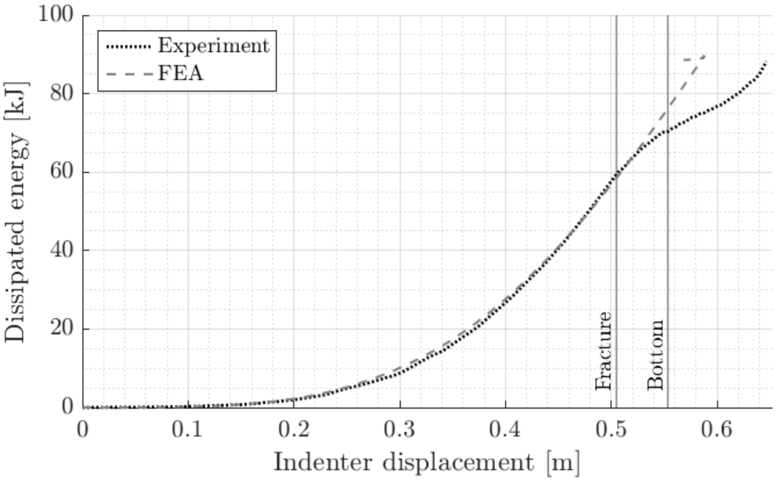

Figure 6.5: Finite element results without failure criterion using shell elements of 25 mm

Up to the experimental point of fracture the agreement between the FEA and experimental results is good. Beyond this point the structural integrity of the plate is compromised. This leads to a reduction of the rate at which energy is dissipated in the experiment. However, in the finite element model no elements are deleted and thus the amount of energy that is being dissipated is overestimated.

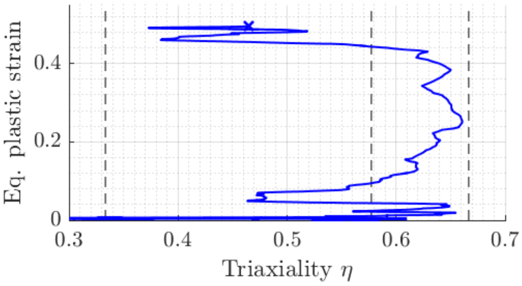

Figure 6.6: Load path of the critical element up to the experimental point of fracture

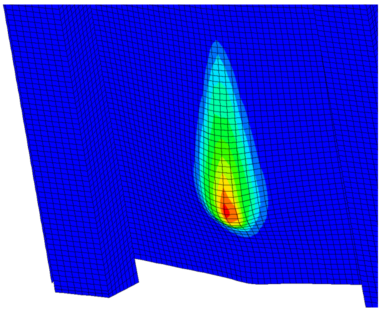

Figure 6.7: Equivalent plastic strain distribution from FEA at the experimental point of fracture

The load path of the element that is deemed to be the first element to be deleted is depicted in Fig. 6.6. This load path was obtained from the integration point where the equivalent plastic strain was the highest at the moment when the indenter displacement in the simulation was equal to the experimental indenter displacement at fracture. As the indenter approaches, the state of stress is between plane strain and equibiaxial tension. Similar to the experiment (Fig. 6.2) failure in the model is expected at the apex of the spherical part of the indenter, where the plastic strain shows a local maximum (Fig. 6.7). At this point the plate is no longer bulging and therefore the stress triaxiality is reduced just before failure.

Failure

Subsequently, failure was introduced by applying the failure loci obtained from combining fracture loci with necking loci (Section 5.2.3). Element erosion occurs as soon as the failure condition $D \geq 1$ (Section 5.1.1) is met in a single integration point, based on the assumption that through-thickness crack growth is unstable.

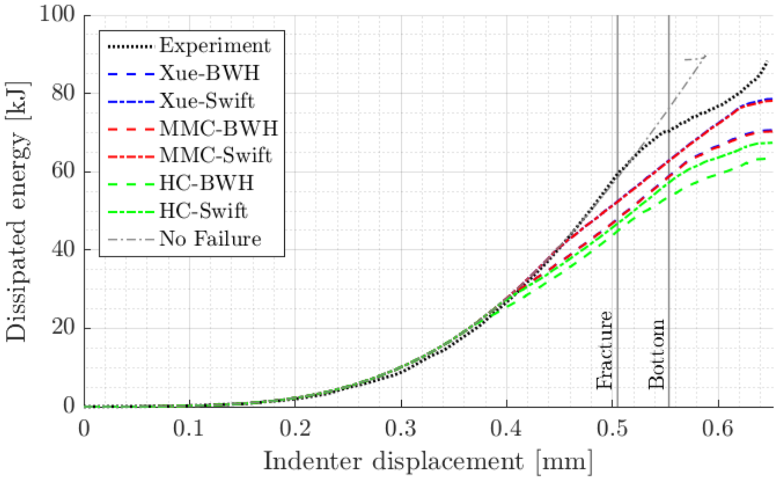

Figure 6.8: Finite element results using combined failure loci as failure criteria

The results in Fig. 6.8 show that the fracture strain is underestimated by all failure loci, meaning that element erosion occurs too early during the simulations and therefore the energy dissipation is underestimated as well. Inspection of the finite element model shows that failure occurs in triaxialities between plane strain tension and equibiaxial tension ($\frac{1}{\sqrt{3}} < \eta \leq \frac{2}{3}$). Therefore the height of the failure loci (Fig. 5.7) in this range is highly related to the total amount of dissipated energy (Fig. 6.8): a larger underestimation of the equivalent strain at failure causes a larger underestimation of the dissipated energy. For further comparison, the Xue-Swift locus is used, since it provides the smallest underestimation of the energy dissipation.

Element dependency

If the theory on element-size dependency that is presented in Section 2.3.3 and applied in Section 5.2.3 is correct, then the results obtained from a solid-element model and a shell-element model must be in agreement with each other. Moreover, scaling the failure locus for different element sizes according to the theory must not affect the amount of dissipated energy.

In the finite element model the shell elements belonging to the specimen part were replaced by solid elements. The dimensions of the solid elements agree with the side lengths and thickness of shell elements. To account for bending stresses and for the poor aspect ratio, LS-DYNA's solid element formulation -2 has been used, which are fully integrated solid elements.

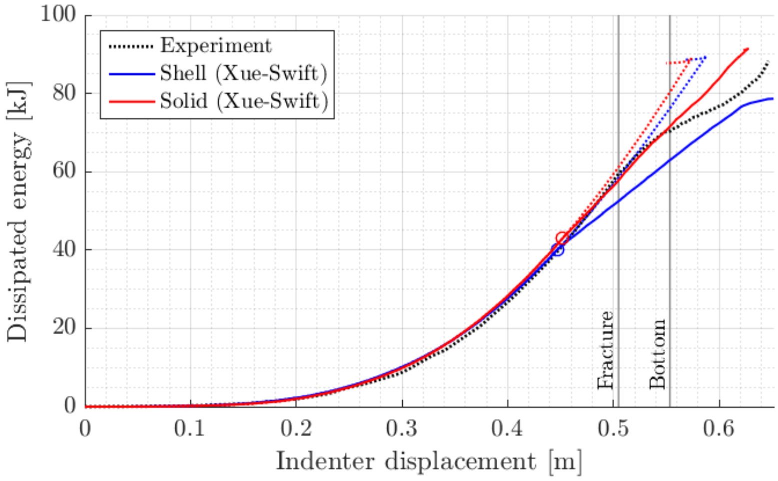

Figure 6.9: Effect of element type

In Fig. 6.9 the results of both models are presented. First deletion of elements is indicated by a circle. The solid model's results are in good agreement with the shell-element results up to element deletion: the rates of energy dissipation are visually indistinguishable and the points at which the first element deletion is predicted are fairly close to each other. This is important as it indicates the validity of the assumption that the response of shells is similar to that of solids for element sizes larger than the thickness. Also, element erosion seems to be barely affected by the element type: The first solid element is removed from the model at a slightly later moment during the simulation. This is attributed to the location within the element where the damage is evaluated. However, after the numerical onset of failure, the solid model overestimates the amount of energy dissipation. The contact definition used in LS-DYNA accounts for the deletion of elements. Its applicability on solid elements, however, is questionable.

The element size of the shell-element model (Fig. 6.3) was reduced by splitting the shell elements in both in-plane directions, resulting in an element size of $l_e = 12.5$ mm and quadruplication of the number of elements. The combined Xue-Swift failure locus was determined for this element size.

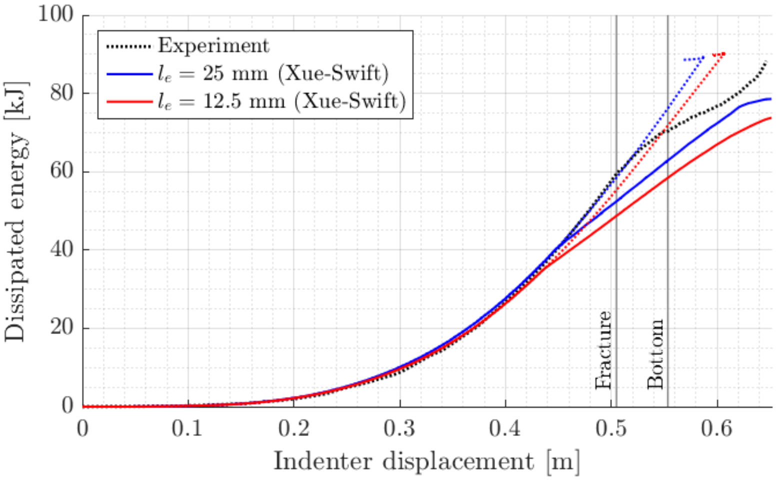

Figure 6.10: Effect of element size

The results of applying the Xue-Swift failure locus for both element sizes are presented in Fig. 6.10. Failure is predicted at an earlier stage during the simulation for the smaller element size, even though the failure strain for the smaller element size is larger: for an equal thickness, the failure locus is higher for a smaller element size, since the scaling factor γ is higher (Fig. 5.6). However, a strain concentration exists in the specimens in proximity of the apex of the indenter. Smaller elements are able to model this strain concentration more accurately, resulting in higher strains than in the original model. Therefore the failure strain is reached at an earlier stage in the simulation, even though the failure strain is higher.

For the finite element results presented in Figures 6.8 & 6.10 the equivalent strain

Table 6.1: Strain at failure and dissipated energy results

l_e [mm]	Failure model	$\bar{\varepsilon}_f$	error [%]	E_{dis}^{bottom} [kJ]	error [%]
25	Xue-BWH	0.401	-19.0	59.22	-15.8
	Xue-Swift	0.446	-9.9	62.74	-10.8
	MMC-BWH	0.402	-18.8	59.09	-16.0
	MMC-Swift	0.447	-9.7	62.47	-11.2
	HC-BWH	0.369	-25.5	53.67	-23.7
	HC-Swift	0.401	-19.0	57.25	-18.6
	Reference	0.495		70.36	
12.5	Xue-Swift	0.531	-29.7	58.43	-17.0
	Reference	0.755		70.36	

at failure of the first element during the simulation are presented in Table 6.1. The reference strain is obtained from the simulation where no failure criterion was applied at the moment of experimental fracture. The results of the dissipated energy are also presented. These results are associated with the moment that the indenter touches the damper at the bottom of the experimental setup.

Practical approach

In this section the Xue-Swift locus is compared to several failure models that require only a single experiment for calibration. In Section 5.2.4 two different single-parameter Modified-Mohr Coulomb loci and two different values of constant equivalent failure strains (CEFS) were presented. These failure models were applied directly in the FEM without combination with a necking locus. The results are depicted in Fig. 6.11 along with the results from applying the Xue-Swift locus to the finite element model.

The MMC locus obtained by assuming equibiaxial tension during the deformation of the circular punch test ($c_2 = 351.8$ MPa) underestimates the failure strain, and therefore the dissipated energy, by a larger percentage than the combined Xue-Swift locus. The MMC locus calibrated using damage accumulation ($c_2 = 380.5$ MPa) over-predicts the failure strain and only deleted two elements during the end of the simulation.

The constant equivalent failure strains predict failure of elements at an earlier stage

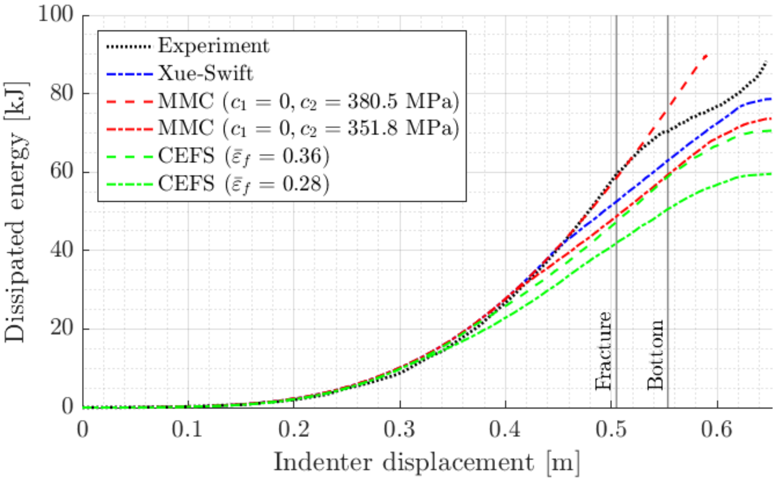

Figure 6.11: Single-parameter failure-loci results

during the simulation than the Xue-Swift locus, indicating an even larger underestimation of the failure strain. This is a logical consequence, since the minimum value of the Xue-Swift locus (Fig. 5.8) is approximately equal to the highest CEFS ($\bar{\varepsilon}_f = 0.36$, from the material certificate); for most states of stress, the Xue-Swift locus predicts higher failure strains.

6.3 Discussion

In the previous section the results from finite element analysis have been compared to experimental results. This section interprets the results and discusses the influence on the results of various aspects explained in this thesis.

Calibration

In Section 5.2.1 the selected fracture models were calibrated on all four small-scale experiments. Subsequently, the MMC model was also calibrated to only the punch test using the same procedure (Variable Load Path Calibration). The latter locus (Fig. 5.8) is substantially lower than the MMC locus calibrated on all four experiments (Fig. 5.3): the strain at fracture in the tensile specimens is substantially higher than the fracture strain in the punch-loaded specimens. The two-parameter fracture models (MMC & Xue) lack the mathematical flexibility to accurately describe fracture in all four specimens. As a result, the fracture loci calibrated on all four specimens would overestimate the fracture strain in the punch specimens, while underestimating th fracture strain in the tensile specimens. The Hosford-Coulomb model is less affected by this phenomenon due to its increased flexibility, courtesy of the additional calibration parameter.

In Section 5.2.3 a method was presented to obtain a ‘combined’ failure locus based on the element size, a necking locus, and a fracture locus. The height of the combined locus depends on the method used to calibrate the S-curve. In this thesis a method was used to account for the effect that the element size has on the failure strain in a necking specimen. Two different element sizes were used to model this experiment. However, the theory to account for element-size dependency could not be validated due to the differences between the results obtained from using different element sizes. Possible causes for these differences are discussed in the two following subsections.

Necking

In Figures 4.6 and 4.10 the force-indentation diagrams of the circular punch and Hašek tests were presented. During the deformation process of the specimens, the force kept increasing until the indentation at fracture was nearly reached; a slight decrease in force is observable from the force-indentation curves just before fracture. Whether this is caused by necking or by loss of integrity due to internal damage cannot be determined.

In Chapter 5 the selected necking and fracture models were calibrated to the material considered in this thesis. The obtained loci (Fig. 5.3) show that necking is always expected long before fracture, independent of the state of stress. This conflicts with the experimental results. Therefore the performance of the necking models is questionable for biaxial tensile conditions under out-of-plane loading, which are common in the event of ship collision. A possible explanation for this is that some bending stresses were present in the bulging specimens, while the necking models were derived assuming uniform in-plane stresses without any bending component.

The failure loci for application in the FEM are obtained using the theory for combining a necking locus and a fracture locus to predict element-size dependent failure of shell elements (Sections 2.3.3 & 5.2.3). The theory results in high dependency of the failure locus on the element size if necking occurs long before fracture, and low element-size dependence if necking occurs just before fracture. Since the necking loci predict necking long before fracture in the bulging experiments, high element-size dependence is obtained for the associated states of stress. Technically, however, small (or even no) element-size dependence is expected, since necking occurred only just before fracture (or not at all).

In summary, in the out-of-plane loaded (bulging) specimens:

1. Necking occurs either just before fracture, or not at all
2. Necking is predicted long before fracture by the necking loci

This causes considerable dependence of the failure strain on the element size in bulging conditions, while no or little element-size dependence is expected. For an increasing element size the failure locus converges towards the necking locus. As a result, failure loci for larger elements generally underestimate the failure strain and the dissipated energy in the raking damage model (Table 6.1 & Fig. 6.8). However, this phenomenon is counteracted, as will be discussed in the following subsection.

Strain concentrations

Both diffuse and localized necking may lead to strain concentrations. To account for these strain concentrations, element-size dependence of the failure locus is introduced by Walters' framework (Walters [2014]). The effects of this framework were discussed in the previous subsection. However, not all strain concentrations are caused by necking: strain concentrations were present in all bulging specimens during the entire deformation processes, yet these concentrations have been caused by the geometry and the load rather than by necking (Fig. 6.7).

Since mesh convergence has typically not been reached in finite element analysis of ship collision, the peak strain within such a strain concentration highly depends on the size of the elements. The theory used in this thesis accounts for strain concentrations due to necking, yet does not account for the element-size dependency of the peak strain in strain concentrations caused by the geometry and the load. If mesh convergence has not been reached, the peak strain is generally underestimated. Therefore the failure strain is overestimated by the method used in this thesis if the mesh is not converged.

This effect counteracts the effect discussed in the previous section, which causes a general underestimation of the failure strain. This can be observed from Fig. 6.10 and Table 6.1: Generally, the failure strain is underestimated. However, the larger elements are less able to accurately model the peak strain, resulting in a smaller total underestimation of the failure strain and dissipated energy. In other words: larger elements underestimate the plastic strain, therefore the failure condition is reached at a later stage during the simulation.

However, two wrongs do not make a right and both effects only increase the uncertainty in the prediction of failure.

Practical approach

In Figure 6.11 the results of several more practical approaches were compared to the results obtained by using the combined Xue-Swift locus to predict failure in 25 mm shell elements. The associated failure loci have been presented in Fig. 5.8. Both values of constant equivalent failure strain result in a large underestimation of the failure strain and the dissipated energy: these values have been determined using tensile tests with a certain gauge length. Therefore CEFS can be interpreted as a failure criterion for a specific loading condition (uniaxial) and a specific element size (the gauge length). Since the CEFS was employed on elements of a different size and under different loading conditions, the poor performance of CEFS is not surprising.

Between the single-parameter Modified-Mohr Coulomb loci, a discrepancy in performance is observed: The failure strain is either over- or underestimated, depending on the calibration method. Assuming pure equibiaxial stress to calibrate the MMC model results in a low failure locus ($c_2 = 351.8$ MPa, Fig. 5.8): the MMC locus is very steep in this region. As a result, a small difference in stress triaxiality has a large effect on the failure strain. Therefore making the equibiaxiality-assumption is not recommended.

On the other hand, using the MMC locus obtained by employing the Variable Load Path Calibration procedure causes an overestimation of the failure strain and the dissipated energy: this locus was calibrated on the load path of the punch test, which was obtained using fine solid elements. Obviously, the inability of the used shell elements to accurately describe peak strains causes the failure condition to be reached at a later stage during the simulation. The MMC locus calibrated on the punch test using the VLPC procedure can therefore be interpreted as an upper-bound of the failure locus for shell elements, but is not expected to provide accurate prediction of failure.

If mesh convergence has not been reached, applying the single-parameter loci to smaller elements is expected to result in element failure at an earlier stage in the simulation: smaller elements describe the strain concentration in the plate in the proximity of the indenter more accurately and yield higher strains, causing the failure condition to be reached sooner. For this specific model with an element size of 25 mm the combined Xue-Swift is preferred over the practical approaches due to its predictive capabilities in terms of failure strain. However, considered the previously discussed influences of the size of the shell elements, the same is not necessarily true for different models or different element sizes.

Friction

The presented dissipated energies contain the contributions of both friction and plastic deformation. As a result, the error made in the modelling of friction also protrudes in the presented results. However, Haag [2017] has concluded that energy dissipation due to friction in the experiment could not be accurately determined from the available digital image correlation results and infrared measurements. Therefore the total energy dissipations were compared in this research, assuming that the Coulomb friction model accurately describes the friction in the experiment and thus assuming that the error due to friction modelling is negligible compared to the error due to failure modelling.

Chapter Summary

This chapter was dedicated to the validation of the stress-state dependent failure criteria presented in the previous chapters. First of all, the raking damage experiment that has been used for validation was introduced, along with the finite element model that has been created. The different failure criteria have been applied to the finite element model and the obtained results were presented and discussed.

Chapter 7

Conclusions

This thesis was set out to offer an improvement in the numerical analysis of ship collision by examining the effect of applying state-of-the-art failure models in LS-DYNA. A research question containing three sub-questions was formulated in Section 1.3 to serve as a guideline throughout this research. In this chapter conclusions are presented in accordance to the research question.

1. Which failure models satisfy the imposed restrictions?

To limit the amount of effort required to use the failure models is LS-DYNA, two restrictions were imposed. First, the failure model was not allowed to depend on more than three calibration parameters. Increasing the amount of calibration parameters highly increases the amount of time required, since more calibration experiments need to be designed, conducted and analyzed. Second, the user must be able to implement the model without expert knowledge of the finite element package, using only the built-in functionality. A method in LS-DYNA was found that allows the application of stress-state dependent failure models. Three fracture models were found to be eligible for this method: The Xue model (after modification to depend on stress triaxiality), the Modified Mohr-Coulomb model (after reduction of the amount of calibration parameters) and the Hosford-Coulomb model. This selection was supplemented by two models that predict the onset of necking: the Swift model for diffuse necking and the Bressan-Williams-Hill model for localized necking.

2. For the application of the material model, the failure models and friction, what precautions can be taken to restrict the introduction of errors?

A sensitivity analysis was performed for three modelling aspects: the element size, initial defect size and the hourglass-control coefficient. The four small-scale experiments were modelled in LS-DYNA using solid elements in accordance with the results of these sensitivity studies.

To determine the material model, an iterative procedure has been used. This procedure, known as the *inverse method*, requires updating the material model in the FEM until a satisfactory match was achieved between the finite element results and an experiment. In this thesis, the uniaxial flat bar tensile test was used: the experiment was modelled in LS-DYNA using solid elements. The results from FEA were compared to the engineering stress-strain curve obtained from the experimental data. Iteratively, the material model was updated and the FE-model was re-evaluated, until the engineering stress-strain curve from FEA could not be visually distinguished from the experimental results.

The effect of friction in the punch-loaded small-scale experiments was modelled by tuning two friction coefficients: one coefficient for the contact between the indenter and the specimen, and another coefficient for the contact between the specimen and the support. The combination of friction coefficients that provides the closest match with the experimental results was used for further analysis. For the raking damage experiment, separate friction tests were conducted by Haag [2017] to determine the friction coefficient between the specimen and the indenter. The results of these friction tests were applied to the finite element model of the raking damage experiment consisting of shell elements.

For the failure models several precautions were taken: LS-DYNA uses an algorithm called *damage accumulation* to determine when elements are deleted from the model. To obtain consistent results, a calibration method was developed based on the inverse of the damage accumulation algorithm. This method was named *Variable Load Path Calibration* and has been used to calibrate the fracture loci. A validation for this method has been presented. Also, the method used to implement a failure model into LS-DYNA was validated to ensure correct application of the failure models.

3. How can the failure models be applied to a finite element model consisting of shell elements?

Walters [2014] provided a theoretical framework to account for element-size dependency of failure in shell elements. This theory combines a fracture locus with a necking locus by using a scaling factor that depends on the size of the shell elements and the thickness of the plate. The theory was modified by employing an alternative shape function, called the *S-curve*, to determine the scaling parameter as a function of the element size. This new shape function required calibration, therefore a calibration method was also presented. Subsequently, the three calibrated fracture loci were combined with two necking loci, using the newly presented method for element-size dependent failure of shell elements. This resulted in six different failure criteria to be applied to the finite element model of the raking damage model used for validation.

Which stress-state dependent fracture prediction method yields the smallest error in terms of energy dissipation by plastic deformation of structural steel plating in the event of collision?

The combination of either the Xue model or the Modified Mohr-Coulomb model with the Swift necking model provides the closest estimation of the amount of dissipated energy during the raking damage experiment. The failure loci obtained from both combinations are very similar and therefore also produce similar results when applied to any finite element model. However, the relative position of the calibrated (theoretical) necking and fracture loci is not in agreement with experimental observations. This causes the applicability of this highly theoretical approach to be questionable. Moreover, the inability of shell elements to accurately describe strain concentrations has a large influence on the prediction of fracture. As a result, the used theoretical approach to predict failure in shell elements is subject to large uncertainties due to the size of these elements.

Besides the theoretical approach, two more practical approaches, the single parameter Modified Mohr-Coulomb model and the constant equivalent failure strain, have been included in this research for comparison. These failure models did not account for element-size dependency. The Xue-Swift locus provides a more accurate prediction of the failure strain than the single-parameter approaches in the raking damage model for the considered element size of 25 mm. This statement can, however, not be made with certainty for other element sizes or other models.

In this research the application of stress-state dependent failure models on shell elements for analysis of the crashworthiness of ships in LS-DYNA has been explored. The merits of applying complex multi-parameter failure models could not be determined. The uncertainty caused by the inability of shell elements to accurately describe strain concentrations and the dependence of the failure strain on element size nullifies the benefits of multi-parameter models. Accurate fracture prediction can only be achieved if the dependency of the failure strain on both the state of stress and the element size is accurately modelled.

Chapter 8

Recommendations

Although fracture can be predicted with reasonable accuracy in finite element models consisting of fine solid elements, fracture prediction in analysis of maritime collision has been shown to be highly subject to effects related to the size of the used shell elements. Based on the findings and gained experience during this research, several recommendations are made in this chapter for future research and for prediction of fracture in the analysis of the crashworthiness of ships.

Future research

Further research towards the effect of element size on failure strain is required. A numerical study towards the effect of different mesh sizes is suggested using, for example, the raking damage experiment. Starting off by determining the failure strain for a converged mesh and then expanding towards larger shell elements may yield insights in how the failure strain is related to the element size in FE models of out-of-plane loaded structures.

For accurate prediction of failure in any type of finite element model consisting of shell elements, models for the element-size dependence and the stress-state dependence of the failure strain are required. Until now, element-size dependence and stress-state dependence have only been treated as uncoupled phenomena. Expanding this research by coupling both dependencies for in-plane tension might prove fruitful.

An alternative to the previous suggestion, is to distinguish between failure in in-plane and out-of-plane loading conditions. No clear evidence of the presence of a neck is found in any of the bulging experiments considered in this research. Further research is required to determine under which conditions necking needs to be accounted for in the prediction of fracture for mild structural steel. Possibly, even a failure model for application in out-of-plane loaded conditions could be conceived.

Application in FEM

Until a viable solution for the element-size-dependency problem has been found, using the maximum shear criterion in the form of the single-parameter Modified Mohr-Coulomb model is suggested. Modelling a punch test using coarse shell elements and calibration using the inverse damage accumulation (the VLPC procedure) is expected to provide reasonably accurate results when applied to a FE model of an out-of-plane loaded plate consisting of shell elements, while the required effort for application remains acceptable.

Continuing on the previous recommendation, calibration on the punch test and application of the obtained locus in the raking damage model using a constant ratio of the shell element size to the indenter radius l_e/R might prove useful as the strain distributions over the spherical part of the indenter are expected to be similar.

Calibration based on assuming the state of stress has been shown to have a detrimental effect on the failure locus and is therefore highly discouraged.

Bibliography

H. S. Alsos, O. S. Hopperstad, R. Törnqvist, and J. Amdahl. Analytical and numerical analysis of sheet metal instability using a stress based criterion. *International Journal of Solids and Structures*, 45(7):2042 – 2055, 2008.

Y. Bai. *Effect of Loading History on Necking and Fracture*. PhD thesis, Massachusetts Intitute of Technology, 2008.

Y. Bai and T. Wierzbicki. A new model of plasticity and fracture with pressure and lode dependence. *International Journal of Plasticity*, Vol. 24:1071–1096, 2008.

Y. Bai and T. Wierzbicki. Application of extended Mohr-Coulomb criterion to ductile fracture. *International Journal of Fracture*, Vol. 161, 2010.

Y. Bao and T. Wierzbicki. On fracture locus in the equivalent strain and stress triaxiality space. *International Journal of Mechanical Sciences*, Vol. 46:81–98, 2004.

J. D. Bressan and J. A. Williams. The use of a shear instability criterion to predict local necking in sheet metal deformation. *International Journal of Mechanical Sciences*, 25(3):155 – 168, 1983.

P. W. Bridgman. *Studies in Large Plastic Flow and Fracture*. McGraw-Hill, 1952.

T. Børvik, O. S. Hopperstad, and T. Berstad. On the influence of stress triaxiality and strain rate on the behaviour of a structural steel. part II. numerical study. *European Journal of Mechanics - A/Solids*, 22(1), 2003.

J. Choung, W. Nam, and J.-Y. Lee. Dynamic hardening behaviors of various marine structural steels considering dependencies on strain rate and temperature. *Marine Structures*, 32:49 – 67, 2013.

G. R. Cowper and P. S. Symonds. Strain-hardening and strain-rate effects in the impact loading of cantilever beams. Technical report, Division of applied mathematics, Brown University, 1957. Technical Report No. 28.

DNV-GL. *Determination of structural capacity by non-linear finite element analysis methods*. Det Norske Veritas - Germanischer Lloyd, September 2016 edition, 2016.

S. R. Haag. Ship grounding damage - an estimate through acceleration measurements. Master's thesis, Delft University of Technology, 2017.

S. R. Haag, M. G. Hoogeland, and A. W. Vredeveldt. Grounding damage estimate through acceleration measurements. *International Conference on Offshore Mechanics and Arctic Engineering*, Vol. 3A, 2017.

J. W. Hancock and A. C. Mackenzie. On the mechanisms of ductile failure in high-strength steels subjected to multi-axial stress-states. *Journal of the Mechanics and Physics of Solids*, Vol. 24:147–160, 1976.

R. Hill. On discontinuous plastic states, with special reference to localized necking in thin sheets. *Journal of the Mechanics and Physics of Solids*, 1(1):19 – 30, 1952.

G. R. Johnson. Materials characterization for computations involving severe dynamic loading. *Proceedings of the Army Symposium on Solid Mechanics*, pages 62–67, 1980.

G. R. Johnson and W. H. Cook. A constitutive model and data for metals subjected to large strains, high strain rates and high temperatures. *Proceedings 7-th International Symposium on Ballistics*, pages 541–547, 1983.

G. R. Johnson and W. H. Cook. Fracture characteristics of three metals subjected to various strains, strain rates, temperatures and pressures. *Engineering Fracture Mechanics*, Vol. 21:a, 1985.

Y. W. Lee. *Fracture Prediction in Metal Sheets*. PhD thesis, Massachusetts Institute of Technology, Cambridge, MA, 2005.

J. Lian and D. Zhou. Diffuse necking and localized necking under plane stress. *Materials Science and Engineering: A*, 111(Supplement C):1 – 7, 1989.

Livermore. *LS-DYNA Keyword User's Manual, Volume I*. Livermore Software Technology Corporation, r:7883 edition, 8 2016.

L. E. Malvern. *Introduction to the Mechanics of a Continuous Medium*. Prentice-Hall, 1969.

Z. Marciniak, K. Kuczynski, and T. Pokora. Influence of the plastic properties of a material on the forming limit diagram for sheet metal in tension. *International Journal of Mechanical Sciences*, 15:789–805, 1973.

F. A. McClintock. A criterion for ductile fracture by the growth of holes. *Journal of Applied Mechanics*, Vol. 35:363–371, 1968.

D. Mohr and S. J. Marcadet. Micromechanically-motivated phenomenological hosford-coulomb model for predicting ductile fracture initiation at low stress triaxialites. *International Journal of Solids and Structures*, 67:40–55, 2015.

J. F. Moxnes and Ø. Frøyland. Mathematical relations related to the Lode parameter for studies of ductility. *Advanced Studies in Theoretical Physics*, Vol. 10:113–124, 2016.

K. Pack and D. Mohr. Combined necking & fracture model to predict ductile failure with shell finite elements. *Engineering Fracture Mechanics*, 182, 2017.

H. Qiu, M. Enoki, Y. Kawaguchi, and T. Kishi. A model for the static fracture toughness of ductile structural steel. *Engineering Fracture Mechanics*, Vol. 70, 2003.

J. R. Rice and D. M. Tracey. On the ductile enlargement of voids in triaxial stress fields. *Journal of the Mechanics and Physics of Solids*, Vol. 17:201–217, 1969.

M. Storheim and J. Amdahl. On the sensitivity to work hardening and strain-rate effects in nonlinear fem analysis of ship collisions. *Ships and Offshore Structures*, 12:100–115, 2015.

H. W. Swift. Plastic instability under plane stress. *Journal of the Mechanics and Physics of Solids*, Vol. 1:1 – 18, 1952.

A. Ugural and S. Fenster. *Advanced Strength and Applied Elasticity*. Prentice-Hall, 4-th edition, 2003. ISBN 0130473928.

E. Voce. The relationship between stress and strain for homogeneous deformation. *Journal of the Institute of Metals*, Vol. 74:537–562, 1948.

R. Von Mises. Mechanik der festen Körper im plastisch deformablen Zustand. *Nachrichten von der Gesellschaft der Wissenschaften zu Göttingen, Mathematisch-Physikalische Klasse*, Vol. 1:582–592, 1913.

L. O. Voormeeren, C. L. Walters, L. Tang, and A. W. Vredeveldt. Estimation of failure parameters for finite element simulations based on a single state of stress and arbitrary stress-strain relation. *Proceedings of the International Conference on Offshore Mechanics and Arctic Engineering - OMAE*, 2014.

C. L. Walters. Framework for adjusting both stress triaxiality and mesh size effect for failure of metals in shell structures. *International Journal of Crashworthiness*, Vol. 19, 2014.

T. Wierzbicki, Y. Bao, Y. W. Lee, and Y. Bai. Calibration and evaluation of seven fracture models. *International Journal of Mechanical Sciences*, Vol. 47, 2005.

L. Xue. Damage accumulation and fracture initiation in uncracked ductile solids subject to triaxial loading. *International Journal of Solids and Structures*, Vol. 44:5163–5181, 2007a.

L. Xue. *Ductile Fracture Modeling - Theory, Experimental Investigation and Numerical Verification*. PhD thesis, Massachusetts Intitute of Technology, 2007b.

L. Xue. Stress based fracture envelope for damage plastic solids. *Engineering Fracture Mechanics*, Vol. 76:419–438, 2009.

Appendices

Appendix A

Fracture Prediction History

One of the earliest and most basic strain-based failure models simply assumes that fracture occurs when a certain equivalent failure strain is reached (Eq. A.1). This model is more commonly known as *Constant Equivalent Failure Strain* (CEFS) and is most straight-forward to use.

$$\bar{\varepsilon}_f = C \tag{A.1}$$

The constant C represents a calibration parameter which requires at least a single test to establish. In hereafter discussed failure models the calibration parameters are also denoted by C, which are not necessarily interchangeable. In the case of multiple calibration parameters in a single model, subscript indices are attributed. Material fracture is predicted at the instant that the equivalent strain equals or exceeds the CEFS.

$$\bar{\varepsilon}_p \geq \bar{\varepsilon}_f \tag{A.2}$$

The constant factor in this equation calibrates the equivalent strain to the first principal strain in the case of uniaxial tension and results in equivalent stress and strain being energy conjugates.

Even though the CEFS completely neglects all dependency on other potentially influential parameters, such as triaxiality and Lode parameter, it is until the present day still an engineer's favourite due to its simplicity; calibration of this failure model is straight-forward, as it has only a single parameter, which can be obtained from a material certificate. However, the capability of predicting failure by the model is limited to the domain close to the state at failure of the calibration test.

An example of a stress-based fracture model is the maximum shear stress criterion. This model is more commonly used for the prediction of material yielding rather than fracture, in which case it is referred to as the Tresca criterion. However, this criterion is applicable as a fracture criterion for a fracture shear stress that exceeds the predicted yielding shear stress.

$$\tau_{max} = \frac{1}{2}\max\big(\sigma_1 - \sigma_2, \sigma_2 - \sigma_3, \sigma_1 - \sigma_3\big) \tag{A.3}$$

Fracture is predicted when the maximum shear stress exceeds a calibrated value.

$$\tau_{max} = (\tau_{max})_f \tag{A.4}$$

Similar to the Von Mises criterion, the maximum shear criterion is prismatic with respect to the octahedral plane, perpendicular to the hydrostatic axis, and therefore forgoes dependency on the hydrostatic component of the stress state. Thus these theories assume that fracture is dependent on the deviatoric stresses only.

In 1968 McClintock studied the void growth response of circular prismatic voids to an applied far field stress and strain (McClintock [1968]). He observed small fracture strains at high stress triaxiality and derived an equivalent strain fracture criterion by assuming that void coalescence occurs if the void length equals the void spacing. The downside of this criterion is that the initial void size and spacing are required to estimate the fracture strain.

Directly after McClintocks publication, J.R. Rice and D.M. Tracey continued on his work by considering spherical voids, publishing their own failure model in Rice and Tracey [1969]. They derived an analytical formulation for the dependence of the growth rate of a single spherical void on the far field strain rate and stress triaxiality. For a perfectly plastic material they found the relation in Eq. A.5, which relates the effective strain rate to the growth rate of the radii of voids. This relation was obtained from curve-fitting the results from numerical simulation of the void growth model.

$$\frac{\dot{R}}{R_0} = 0.283\,\exp\Big(\frac{3}{2}\eta\Big)\dot{\bar{\varepsilon}} \tag{A.5}$$

Eq. A.5 can be expressed in terms of equivalent strain to fracture by means of integration:

$$\bar{\varepsilon}_f = C\,\exp(-\frac{3}{2}\eta) \tag{A.6}$$

Ever since these publications, the stress triaxiality is commonly acknowledged as one of the dominating parameters in ductile fracture. In Hancock and Mackenzie [1976] it was stated that a void nucleation threshold strain, ε_n, exists, which is independent of the stress state and added it to the Rice-Tracey model. They postulated that the equivalent failure strain was a function of the stress triaxiality in the form of Equation A.7.

$$\bar{\varepsilon}_f = C_1 + C_2 \exp\left(-\frac{3}{2}\eta\right) \tag{A.7}$$

This model was adapted in Johnson and Cook [1985] for dynamic loading conditions, such as high-velocity impact and blast, by adding dependency on strain rate and temperature. The influences of these variables were captured in the form of Eq. A.8. Based on experimental observations, they replaced the constant in the triaxiality exponent by a coefficient and they introduced dependency on strain rate and temperature. However, the temperature dependency in this model was established using tests above room temperature only. Ductile-brittle transition occurs below room temperature and has a different effect on the failure strain, which the JC model fails to account for.

$$\bar{\varepsilon}_f = [C_1 + C_2 \exp(C_3\eta)][1 + C_4 \ln(\dot{\bar{\varepsilon}})][1 + C_5 T^*] \tag{A.8}$$

In the analysis of collision the JC model is often used in its reduced form (without strain rate and temperature dependent terms) since the occurrence is mostly in the quasi-static domain with temperatures close to room temperature (Wierzbicki et al. [2005], Lee [2005]). Except for C_3 the reduced form of the JC model is equal to the model proposed by Hancock & Mackenzie: The novelty of the JC model does not lie in the formulation of the fracture strain; the novel feature of the model was the dependency on all stress states up to fracture: Johnson [1980] was the first to account for a varying stress state during loading conditions. This was achieved by introducing a *damage parameter* D which comprises a contribution from all past stress states:

$$\Delta D = \frac{\Delta\bar{\varepsilon}_p}{\bar{\varepsilon}_f} \tag{A.9}$$

The onset of fracture is predicted when the damage parameter reaches the critical value of unity. Clearly, in previous equation, the damage increment varies as the equivalent fracture strain changes due to a variation in triaxiality. As such, a variable load path is accounted for in the failure prediction. This caused the model to become popular and has been widely used for a long time; it still finds its way in many commercial finite element packages.

The dependency of equivalent fracture strain on the stress state of all previously discussed models was determined using analytical models for void nucleation, growth and coalescence. In 2004 Yingbin Bao and Tomasz Wierzbicki presented experimental test results that contradicted the existing failure models (Bao and Wierzbicki [2004]). They proposed the a failure model (the BW model) that distinguishes two different fracture mechanisms and created a combined fracture locus in the space of equivalent strain and stress triaxiality. It was stated that a transition between mechanisms occurs at $\eta \approx 0.4$, below which shear fracture dominates, while void coalescence causes failure at higher stress triaxialities. In the intermediate domain both fracture mechanisms collaborate. Their failure model holds a cut-off value of $\eta = -1/3$, which was observed from their experiments: Failure did not occur at lower triaxialities, regardless of the equivalent plastic strain. A failure model was presented in the form of Eq. A.10.

$$\bar{\varepsilon}_f = \begin{cases} C_1 \cdot (\eta + \frac{1}{3})^{-C_2}, & -\frac{1}{3} \leq \eta < 0 \\ C_3 \cdot \eta^2 - C_4 \cdot \eta + C_5, & 0 \leq \eta < \eta_T \\ C_6 \cdot \eta^{-1}, & \eta \geq \eta_T \end{cases} \tag{A.10}$$

Where η_T denotes a triaxiality transition value, depicting the transition from shear fracture to fracture due to void coalescence, with the remark that the transition value is a material constant.

Although the BW model contains six constants, fewer tests are required to calibrate the model. Coefficient C_5 determines the equivalent failure strain in pure shear. Since the first two expressions in eq. A.10 must be coincident at $\eta = 0$ to create a continuous fracture locus (Fig. A.1), C_1 and C_2 become dependent on one another. Similarly C_6 follows from the second expression evaluated at $\eta = \eta_T$. Thus the amount of independent coefficients is reduced by two, leading to just four required calibration tests.

The BW results suggest that the equivalent strain at failure is not dependent on the triaxiality parameter alone. Xue was the first to introduce a failure model with I_1-J_2-J_3 dependency (Xue [2007b]), I and J indicating the invariants of the stress tensor and deviatoric stress tensor respectively. He presented a failure model where the EFS is a function of both triaxiality and Lode parameter: The hydrostatic stress is proportional to I_1, the equivalent stress can be obtained from J_2. The Lode parameter has many formulations which are all related to the ratio of J_3 to the equivalent stress.

Ever since the publication of the Xue model, the fracture mechanics community seems convinced of the importance of both stress triaxiality and Lode parameter: Most of the more recent failure models are presented in the space of triaxiality, Lode param-

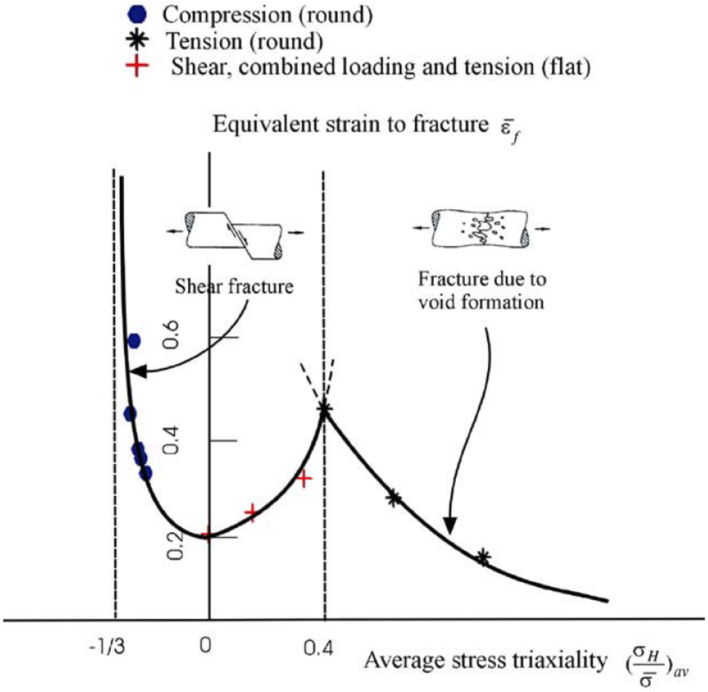

Figure A.1: Fracture locus as determined by Bao and Wierzbicki, calibrated for Al 2024-T351 (From Bao and Wierzbicki [2004])

eter and equivalent failure strain. Several of these models were presented in Section 3.1 and have been implemented into LS-DYNA.

Appendix B

Material Inspection Certificate

In this part of the appendix the material inspection certificate produced by the manufacturer of the steel plate that was used in this thesis is presented.

NLMK DanSteel A/S
Havnevej 33
(A01) DK-3300 Frederiksværk

Inspection Certificate (A02)

EN 10204:2004/3.2

Page 1 of 6
Date of creation: (Z02) 16.04.2014
Certificate No.: (A03) **018337**

Our order No.: (A08) 4132031 **Your order No.:** (A07) 1670900 **Order registration date:** 14.03.2014 **Date of dispatch:** 15.04.2014 B

Material requirements and customer information

Product: (A03) Plate

Delivery condition: (B04) As rolled (AR)

Steel standard and grade: (B02) LR/A

Customer name and address (A06)
7119
De Boer Staal B.V.
Postbus 17
Molenstraat 28
1911 DA Uitgeest
NETHERLANDS

Certificate address
7119001
Certificaten@deboerstaal.nl

Surface tolerance: EN 10163-2 B3
Length tolerance: EN 10029 Table 3
Width tolerance: EN 10029 Table 2
Thickness tolerance: EN 10029 Class B
Flatness tolerance: EN 10029 Table 4 Class N

Supplementary information: (C04)
Fully Killed and Fine Grain

Visual examination and dimensional checking: Satisfactory. The results of tests performed are in compliance with the requirements. (Z01)

Details of supplied materials dimensions, weights and pieces

Heat/Slab (B07)	Plate No. (B06)	Item	Thickness mm (B09)	Width mm (B10)	Length mm (B11)	Pieces (B08)	Gross kg (B12)	Hard stamp	Stamp location	Customer remark (B99)
45984G4	7834S	1	5.0	3000	8000	1	942	LR A	Head	1670900
45984F3	7838S	1	5.0	3000	8000	1	942	LR A	Head	1670900
45765B2	7415S	2	5.0	3000	11650	1	1 372	LR A	Head	1670900
45760I4	7627S	5	6.0	3000	11650	1	1 646	LR A	Head	1670900
45760B4	7787S	5	6.0	3000	11650	1	1 646	LR A	Head	1670900
45760A4	7790S	5	6.0	3000	11650	1	1 646	LR A	Head	1670900
45765N4	8410S	5	6.0	3000	11650	1	1 646	LR A	Head	1670900
45984G2	7836S	6	7.0	2000	8000	2	1 758	LR A	Head	1670900
45927I5	7965S	8	8.0	3000	11650	1	2 195	LR A	Head	1670900
45923A4	8389S	8	8.0	3000	11650	1	2 195	LR A	Head	1670900
45920C5	7735S	12	15.0	3000	11650	1	4 115	LR A	Head	1670900

Lloyd's Register EMEA
Copenhagen Office
Lloyd's Register

(A04)

Third party inspection (Z03)
LR

Inspection representative NLMK DanSteel A/S (A05)
Simeon Tulip

NLMK DanSteel A/S
Havnevej 33
DK-3300 Frederiksværk
(A01)

Inspection Certificate (A02)

EN 10204:2004/3.2

Page 2 of 6
Date of creation: (Z02) 16.04.2014
Certificate No.: (A03) **018337**

Our order No.: (A08) 4132031 **Your order No.:** (A07) 1670900 **Order registration date:** 14.03.2014 **Date of dispatch:** 15.04.2014 B

Details of supplied materials dimensions, weights and pieces

Heat/Slab (B07)	Plate No. (B06)	Item	Thickness mm (B09)	Width mm (B10)	Length mm (B11)	Pieces (B08)	Gross kg (B12)	Hard stamp	Stamp location	Customer remark (B99)
45984F4	7831S	18	5.0	3000	12000	1	1 413	LR A	Head	1670900
45984F3	7838S	18	5.0	3000	12000	1	1 413	LR A	Head	1670900
						14	22 929			

Lloyd's Register EMEA
Copenhagen Office
Lloyd's Register

(A04)

Third party inspection (Z03)
LR

Inspection representative NLMK DanSteel A/S (A05)
Simeon Tulip

(A01) **NLMK DanSteel A/S**
Havnevej 33
DK-3300 Frederiksværk

Inspection Certificate (A02)

EN 10204:2004/3.2

Page 3 of 6
Date of creation: (Z02) 16.04.2014
Certificate No.: (A03) **018337**

Our order No.: (A08) 4132031 **Your order No.:** (A07) 1670900 **Order registration date:** 14.03.2014 **Date of dispatch:** 15.04.2014 B

Chemical composition (heat analysis) **all results in %**

Heat No. (B07)		C	Mn	Si	P	S	Al
Set values:	min.		0.00				0.020
	max.	0.21		0.50	0.035	0.035	
45760		0.13	0.92	0.20	0.013	0.011	0.041
45765		0.13	0.86	0.17	0.011	0.006	0.040
45920		0.12	1.09	0.17	0.012	0.005	0.039
45923		0.13	1.09	0.16	0.007	0.007	0.039
45927		0.15	1.21	0.18	0.008	0.004	0.039
45984		0.13	0.84	0.17	0.005	0.005	0.037

Heat No. (B07)		**CEV**	**Remark** (C70)
Set values:	min.		
	max.		
45760		0.29	1 3 6
45765		0.28	1 3 6
45920		0.31	1 3 6
45923		0.32	1 3 6
45927		0.36	1 3 6
45984		0.27	1 3 6

Supplementary information (C99)

CEV = C + Mn/6 + (Cr + Mo + V)/5 + (Ni + Cu)/15
1 = Basic Oxygen Steel, 2 = Electric Arc Furnace, 3 = Ladle Refined, 4 = Calcium Treated, 5 = Vacuum Degassed, 6 = Continuous Cast, 7 = Ingot

Lloyd's Register EMEA
Copenhagen Office
Lloyd's Register

(A04)

Third party inspection (Z03)
LR

Inspection representative NLMK DanSteel A/S (A05)
Simeon Tulip

NLMK DanSteel A/S
Havnevej 33
DK-3300 Frederiksværk
(A01)

Inspection Certificate (A02)

EN 10204:2004/3.2

Page	4 of 6
Date of creation: (Z02)	16.04.2014
Certificate No.: (A03)	**018337**

Our order No.: (A08) 4132031 **Your order No.:** (A07) 1670900 **Order registration date:** 14.03.2014 **Date of dispatch:** 15.04.2014 B

Tensile testing

Tensile tests were performed in accordance with EN 10002/ISO 6892-1 with results as stated below:

Heat/slab (B07)	Plate ID (B06)	Thickness mm	Shape (C10)	Loc. (C01)	Dir. (C02)	Yield MPa (C11)	Yield type	UTS Rm MPa (C12)	Elong. type	Elongation % (C13)	Yield/UTS
45765B2	7415S-2-1	5.0	R	H	T	298	REH	427	A5	47	0.70
45760I4	7627S-2-1	6.0	R	H	T	298	REH	430	A5	43	0.69
45920C5	7735S-1-1	15.0	R	H	T	279	REH	427	A5	41	0.65
45760B4	7787S-2-1	6.0	R	H	T	282	REH	433	A5	45	0.65
45760A4	7790S-2-1	6.0	R	H	T	282	REH	433	A5	45	0.65
45984F4	7831S-1-1	5.0	R	H	T	297	REH	421	A5	50	0.71
45984G4	7834S-2-1	5.0	R	H	T	296	REH	429	A5	46	0.69
45984G2	7836S-1-1	7.0	R	H	T	296	REH	429	A5	46	0.69
45984G2	7836S-1-2	7.0	R	H	T	288	REH	420	A5	45	0.69
45984F3	7838S-1-1	5.0	R	H	T	288	REH	420	A5	45	0.69
45984F3	7838S-2-1	5.0	R	H	T	288	REH	420	A5	45	0.69
45927I5	7965S-2-1	8.0	R	H	T	305	REH	465	A5	39	0.66
45923A4	8389S-1-1	8.0	R	H	T	302	REH	448	A5	42	0.67
45765N4	8410S-2-1	6.0	R	H	T	291	REH	423	A5	47	0.69

Supplementary Information (C99)
Loc.: (C01) H = head, T = tail
Dir.: (C02) T = transversal, L = longitudinal
Shape: (C10) Ø = round, R = rectangular
Original gauge length: 200 mm

Lloyd's Register EMEA
Copenhagen Office
Lloyd's Register

(A04)

Third party inspection (Z03)
LR

Inspection representative NLMK DanSteel A/S (A05)
Simeon Tulip

NLMK DanSteel A/S
Havnevej 33
DK-3300 Frederiksværk
(A01)

Inspection Certificate (A02)

EN 10204:2004/3.2

Date of creation: (Z02) 16.04.2014
Certificate No.: (A03) **018337**

Our order No.: (A08) 4132031 **Your order No.:** (A07) 1670900 **Order registration date:** 14.03.2014 **Date of dispatch:** 15.04.2014 B

Impact testing

Impact tests were performed in accordance with EN 10045/ISO 148-1 with results as stated below:

Heat/slab (B07)	**Plate ID** (B06)	**Position** (C01)	**Notch** (C40)	**Shape** (C41)	**Loc.** (C01)	**Dir.** (C02)	**Temp.** °C (C03)	**SV** J (C42)	**SV** J (C42)	**SV** J (C42)	**AV** J (C43)
45765B2	7415S-2-1	1	CV	5x10	H	L	20	85	89	80	85
45760I4	7627S-2-1	1	CV	5x10	H	L	20	66	68	63	66
45920C5	7735S-1-1	1	CV	10x10	H	L	20	253	242	236	244
45760B4	7787S-2-1	1	CV	5x10	H	L	20	76	73	81	77
45760A4	7790S-2-1	1	CV	5x10	H	L	20	76	73	81	77
45984F4	7831S-1-1	1	CV	5x10	H	L	20	81	77	74	77
45984G4	7834S-2-1	1	CV	5x10	H	L	20	81	77	74	77
45984G2	7836S-1-1	1	CV	5x10	H	L	20	81	77	74	77
45984G2	7836S-1-2	1	CV	5x10	H	L	20	81	77	74	77
45984F3	7838S-1-1	1	CV	5x10	H	L	20	81	77	74	77
45984F3	7838S-2-1	1	CV	5x10	H	L	20	81	77	74	77
45927I5	7965S-2-1	1	CV	5x10	H	L	20	75	80	78	78
45923A4	8389S-1-1	1	CV	5x10	H	L	20	73	75	74	74
45765N4	8410S-2-1	1	CV	5x10	H	L	20	85	89	80	85

Supplementary Information (C99)
Position: (C01) 1 = surface, 2 = middle, 3 = 1/3 of thickness, 4 = 1/4 of thickness
Notch: (C40) CU = Charpy U-notch, CV = Charpy V-notch, CVA = Charpy V-notch (ASTM)
Loc.: (C01) H = head, T = tail
Dir.: (C02) T = transversal, L = longitudinal

Lloyd's Register EMEA
Copenhagen Office
Lloyd's Register

(A04)

Third party inspection (Z03)
LR

Inspection representative NLMK DanSteel A/S (A05)
Simeon Tulip

NLMK **DanSteel A/S**
Havnevej 33
(A01) DK-3300 Frederiksværk

Inspection Certificate (A02)

EN 10204:2004/3.2

Page 6 of 6
Date of creation: (Z02) 16.04.2014
Certificate No.: (A03) **018337**

Our order No.: (A08) 4132031 **Your order No.:** (A07) 1670900 **Order registration date:** 14.03.2014 **Date of dispatch:** 15.04.2014 B

Ship Steel or Steel for Ships, Boiler, Pressure Vessel and for welded Machinery Structures. We hereby certify that the Plates have been made by an approved process in accordance with, the rules of the stated Classification Society and the stated Steel Grade. Testing of the hereby certified materials has been carried out with satisfactory results in the presence of the Classification Society's Surveyor.

Lloyd's Register EMEA
Copenhagen Office
Lloyd's Register

(A04)

Third party inspection (Z03)
LR

Inspection representative NLMK DanSteel A/S (A05)
Simeon Tulip

Appendix C

Specimen Geometries

In this part of the appendix the geometries of the different specimens associated with the small scale experiments are presented.

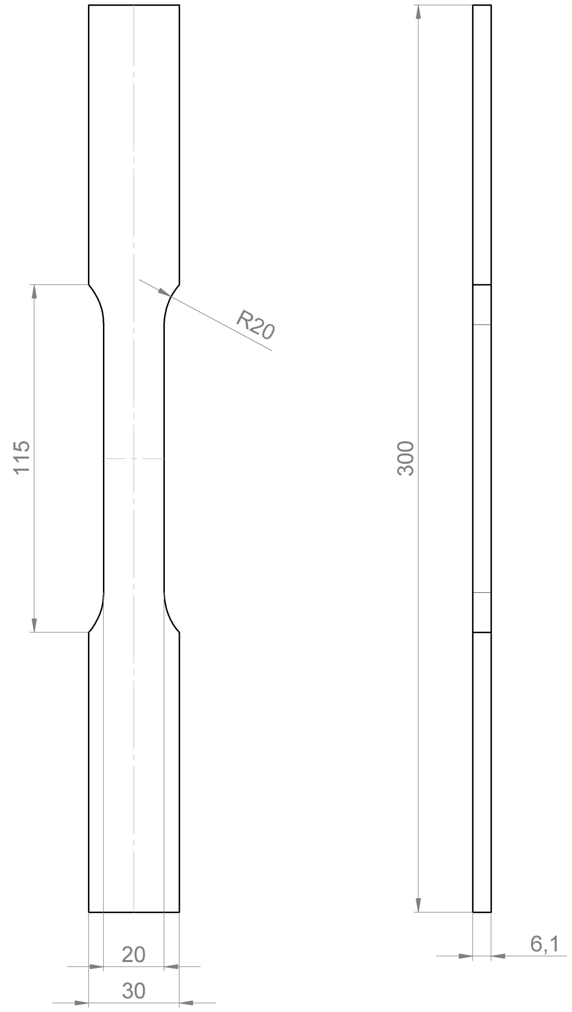

Figure C.1: Flat bar tensile specimen geometry

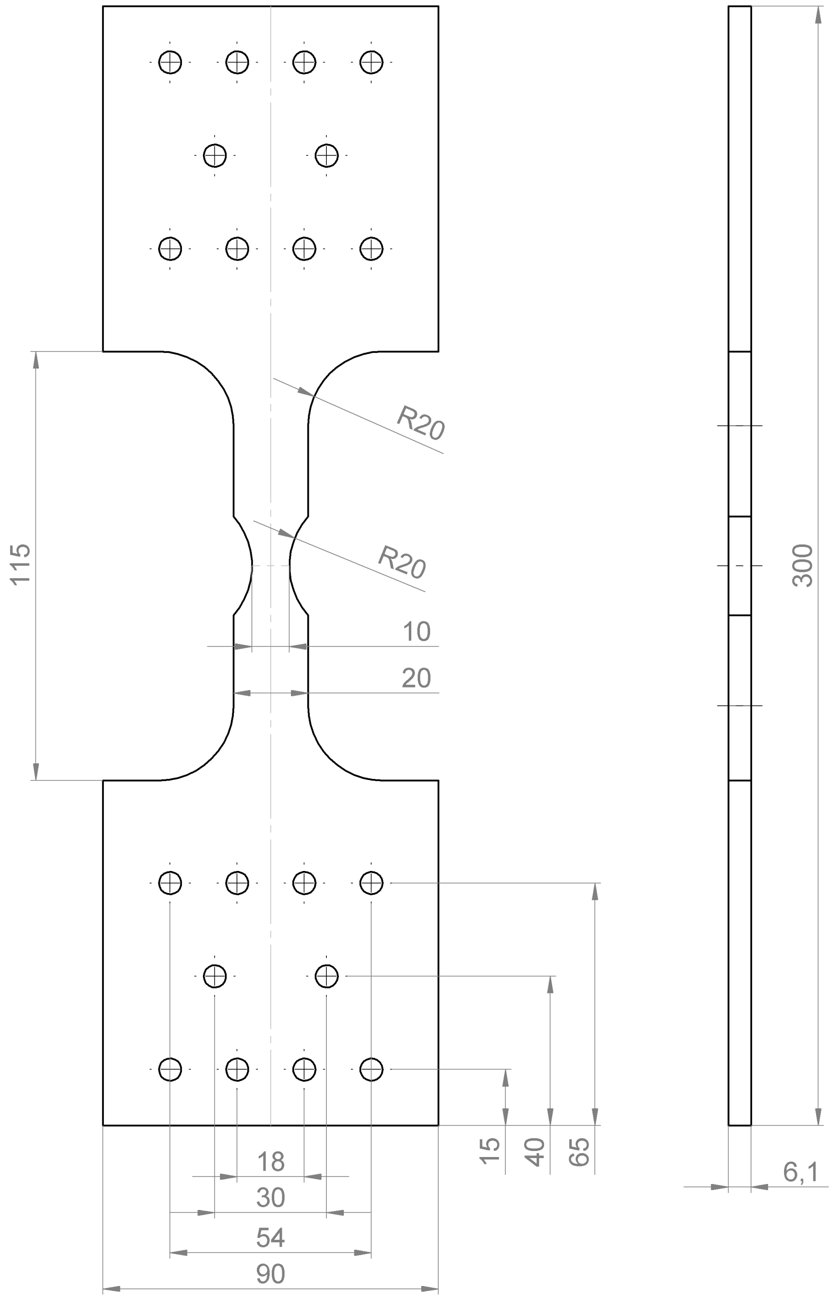

Figure C.2: Circular punch specimen geometry

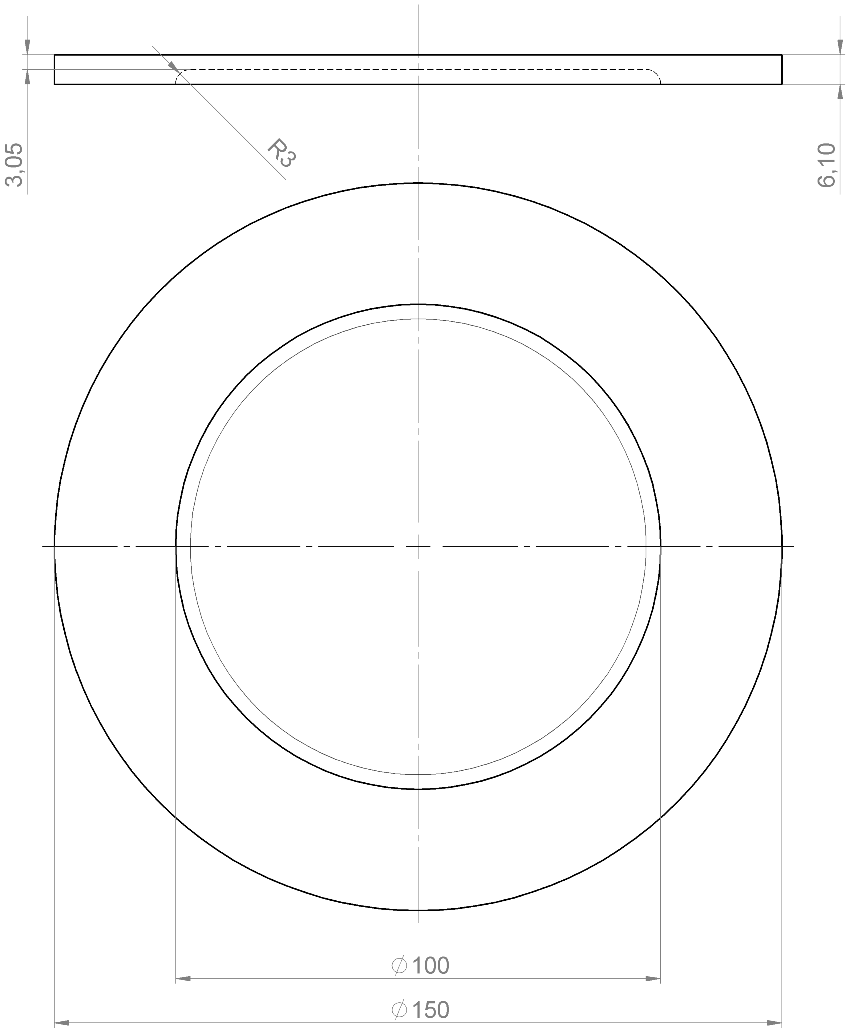

Figure C.3: Circular punch specimen geometry

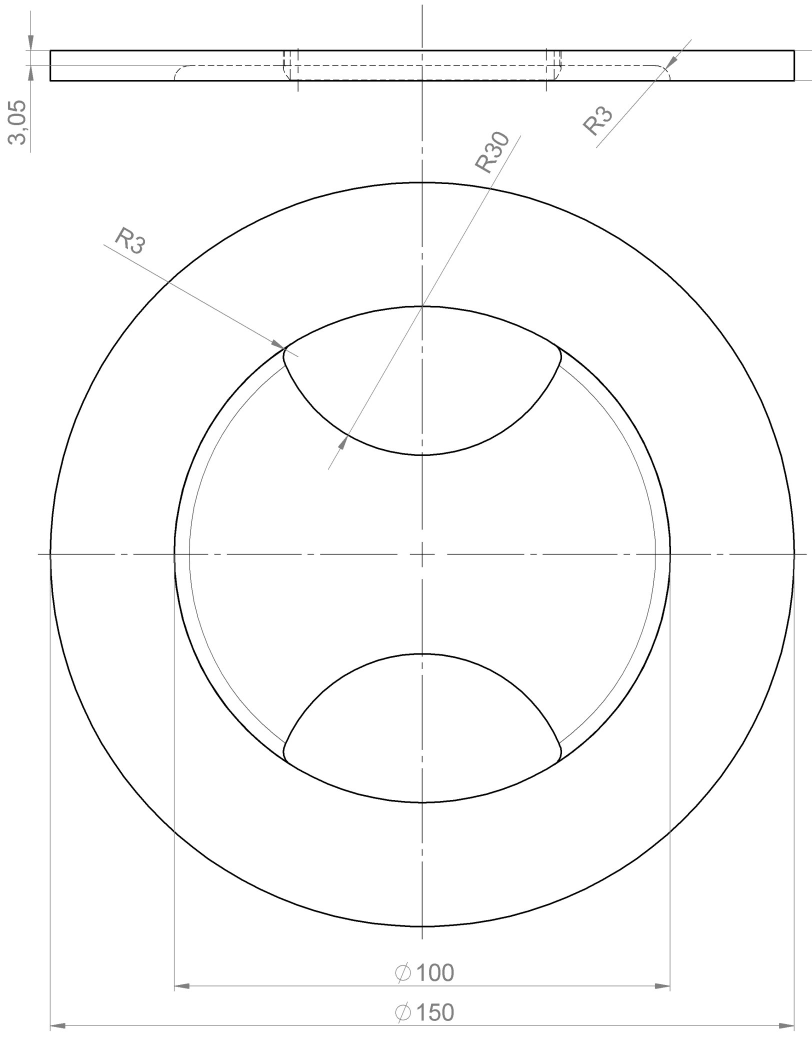

Figure C.4: Notched punch specimen geometry

Appendix D

Small Scale Experiment Finite Element Models

This part of the appendix presents the finite element models associated with the small scale experiments that were conducted in the course of this research. In Section 4.2 several modelling parameters were determined based on sensitivity analyses of the flat bar tensile model. The obtained parameters apply to the models associated with the small-scale experiments:

Table D.1: Parameters determined in sensitivity analyses

Parameter	Symbol	Value	Unit
Element Size	l_e	0.5	mm
Hourglassing coefficient	q_h	0.005	-
Initial defect	-	0	%

Only two types of elements are used across all models, their specifications are listed in Table D.2. The material model for the specimens was derived using the iterative procedure as presented in Section 4.3. This material model is implemented into LS-DYNA using the *MAT_PIECEWISE _LINEAR_PLASTICITY keyword. For all peripheral parts, such as supports and indenters, a rigid material formulation is used based on the *MAT_RIGID keyword in LS-DYNA. The exact specifications for each part are listed in the description of each model.

Table D.2: Specifications of elements

Type	Formulation	# nodes	# integration points
Shell	Belytschko-Tsay	4	5
Solid	Constant stress	8	1

Flat Bar Tensile Finite Element Model

In the flat bar tensile model two rows of nodes are located at exactly 30 mm from the center in both longitudinal directions. This total distance between the rows of 60 mm corresponds to the gauge length of the extensometer as used in the experiment. The nodes at one end of the specimen are fully clamped, while the nodes at the other end undergo a linear displacement in longitudinal direction.

Table D.3: Part information

Part	Element Type	Number of elements	Material
Specimen	Solid	75299	Piecewise linear plasticity

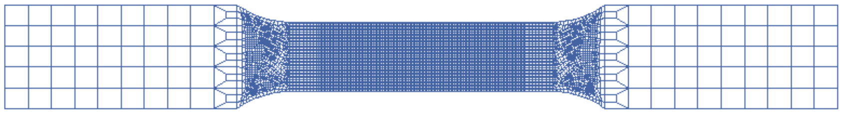

(a) Front view

(b) Side view

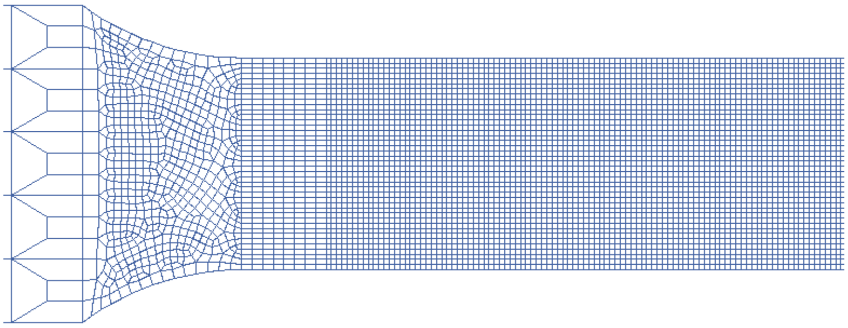

(c) Front view detail

Figure D.1: Flat bar tensile specimen model

Notched Flat Bar Tensile Finite Element Model

In the notched flat bar tensile model two rows of nodes are located at exactly 21.7 mm from the center in both longitudinal directions. This total distance between the rows of 43.4 mm corresponds to the gauge length of the extensometer as used in the experiment. The nodes at one end of the specimen are fully clamped, while the nodes at the other end undergo a linear displacement in longitudinal direction.

Table D.4: Part information

Part	Element Type	Number of elements	Material
Specimen	Solid	28397	Piecewise linear plasticity

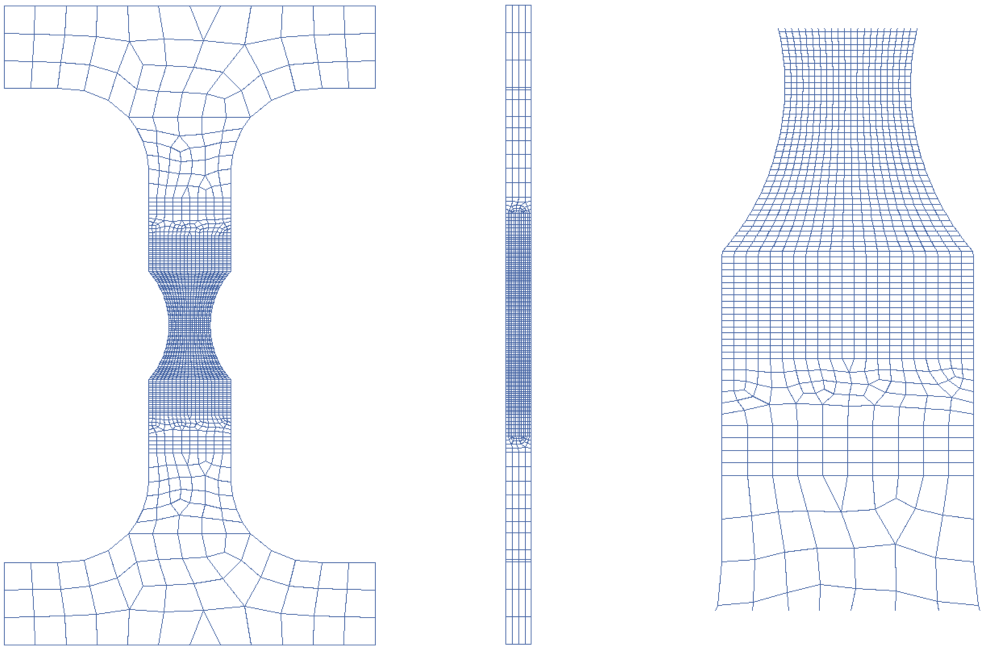
(a) Front view (b) Side view (c) Front view detail

Figure D.2: Notched flat bar tensile specimen model

Circular Punch Finite Element Model

The finite element model of the circular punch test consists of four parts (Fig D.3a): the specimen (blue), the indenter (green), and the upper and lower supports (yellow). The supports are fully clamped rigid bodies. The indenter is also a rigid body and has been constrained in all directions except the vertical direction. Contact definitions are applied between the thick part of the specimen and the supports, and between the top of the thinned part of the specimen and the indenter. All rigid body parts are meshed with shell elements, whose size is in agreement with the element size of the opposite contact surfaces (Fig. D.3c).

The vertical displacement of the indenter was prescribed: Similar to the experiments, the indenter moved downwards with a constant velocity of 1.0 mm/s until a depth of indentation that matches with the mean experimental indentation at fracture. After one second the indenter is raised again until there was no more contact with the specimen to allow spring-back.

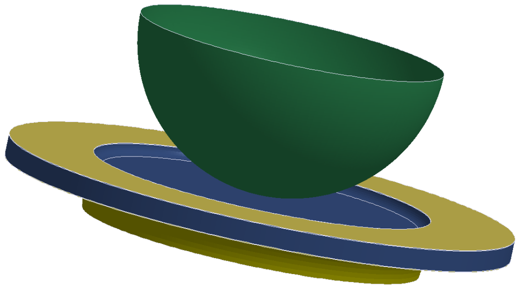

(a) Overview

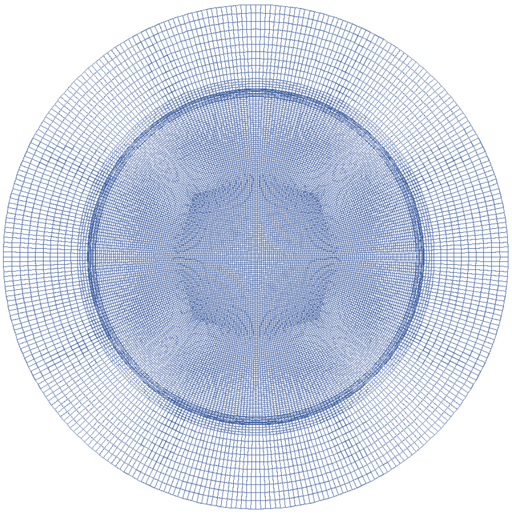

(b) Meshed specimen mid-plane section view

(c) Meshed specimen top view

Figure D.3: Circular punch finite element model

Table D.5: Part information

Part	Element Type	Number of elements	Material
Specimen	Solid	194240	Piecewise linear plasticity
Indenter	Shell	19200	Rigid
Upper support	Shell	4480	Rigid
Lower support	Shell	6400	Rigid

Hašek Punch Finite Element Model

The model of the Hašek punch test is very similar to the circular punch: the parts for the indenter and the supports are identical (Fig. D.4a and Table D.6) in terms of meshes, but also in contact areas and constraints.

The only difference between the Hašek and the circular punch models is the maximum depth of indentation: logically, for the current model, it is set to the mean indentation at fracture of the Hašek specimens.

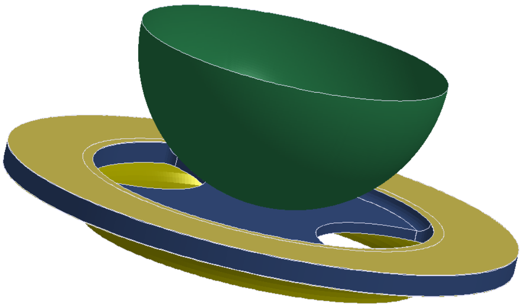

(a) Overview

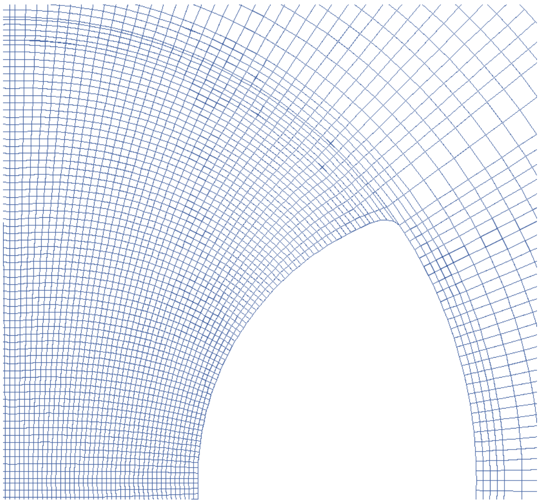

(b) Meshed specimen mid-plane section view

(c) Meshed specimen top view (detail)

Figure D.4: Hašek punch finite element model

Table D.6: Part information

Part	Element Type	Number of elements	Material
Specimen	Solid	78408	Piecewise linear plasticity
Indenter	Shell	19200	Rigid
Upper support	Shell	4480	Rigid
Lower support	Shell	6400	Rigid

Appendix E

Tensile Test Report

In this part of the appendix the engineering stress-strain curves obtained from the flat bar tensile tests conducted by Element Material Technologies are presented. The associated test report is included. The tests were conducted according to the NEN-EN-ISO-6892-1:2016 standard.

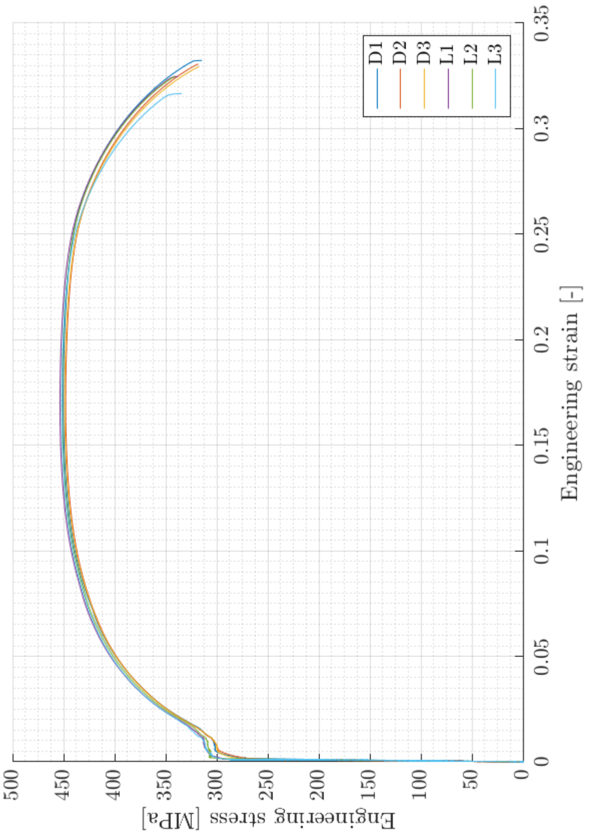

Figure E.1: Engineering stress-strain results from tensile testing

element™

Element Materials Technology
Zekeringstraat 33
1014 BV Amsterdam NL

P +31 (0)20 556 35 55
F +31 (0)20 556 35 56
Info.amsterdam@element.com
element.com

Bank ABN AMRO, Amsterdam
Acct 52.99.93.821
BTW NL0086.06.754.B01
KvK 33194077

TNO
Postbus 96846
2509 JE 's-Gravenhage

Date : 13-01-2017
Element report number : EAM020354
Customer reference : -

TEST REPORT

DESTRUCTIVE TESTING OF WELDED PRINTED PLATE

WPS number	:
Item description	: 6 Tensile samples
Material	: S235 (according EN 10025-2)
Condition	: As delivered
Testing in accordance with	: Customer

DESTRUCTIVE TEST

TENSILE TEST

Test method: ISO 6892-1 Orientation: Transverse Test temperature: R.T.

Specimen	Size [mm]	Cross section [mm²]	Yield strength [MPa] ReH	[MPa] Rp0,2	Tensile strength [MPa] Rm	Elongation [%] After fracture A5	E-modulus [GPa]
F20354-1	20.06x6.08	122.0		299	456	33.0	174
F20354-2	20.02x6.10	122.1		291	453	33.0	237
F20354-3	20.06x6.10	122.4		297	454	33.0	273
F20354-4	19.96x6.11	122.0		310	459	32.5	215
F20354-5	20.02x6.12	122.5		312	457	31.5	243
F20354-6	20.05x6.13	122.9		311	456	32.5	190

CONCLUSIONS/REMARKS

No requirements available

Element Materials Technology

Authorised: W.H. Mooij

element™
Element Materials
Technology Amsterdam B.V.

Appendix F

Extensometer

To measure the displacement of the notched flat bar tensile tests an extensometer was applied to the specimens. Considering the expected elongation of the specimens, an extensometer was selected based on its maximum measurable deformation. The selected extensometer is produced by Epsilon Technology, model 3542-025M-050-LT, having a maximum measurable deformation of 12.5 mm. Unfortunately the gauge length of this model is only 25.0 mm, which was insufficient to span the area of localized straining (i.e. the length of the notch, 27 mm). To overcome this problem the gauge length was extended using custom made PMMA spacer blocks with a thickness of 6.13 mm. Stacking three spacer blocks resulted in a gauge length of 43.4 mm (Fig. F.1).

Figure F.1: Modified Epsilon 3542-025M-050-LT extensometer mounted on notched tensile specimen R1N1

To determine whether or not the geometrical modification has influence on the measured results, a simple model was constructed as depicted in Fig. F.2. Points **A** and **B** indicate the unmodified clamping locations of the extensometer. Point **C** indicates the shift of **B** due to the introduction of the custom spacer blocks. The exact hinge location is unknown, as it is undocumented and hidden from the eye by the extensometer's casing. The hinge was assumed to be in the corner.

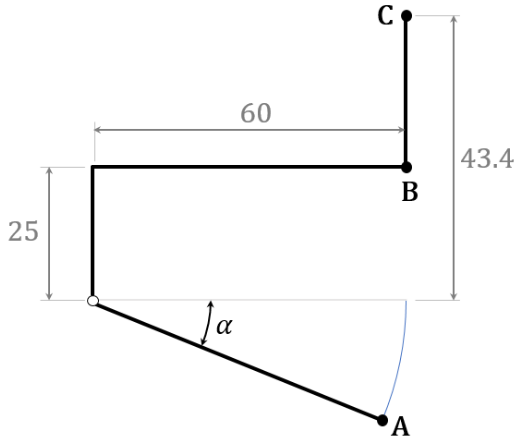

Figure F.2: Model to determine the effect of the modification

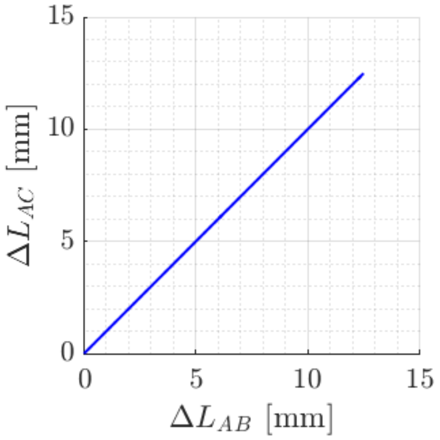

Figure F.3: Relation between original elongation and modified elongation

Taking the hinge as the origin, the coordinates of the points are described by:

$$x_A = 60\cos\alpha \qquad y_A = -60\sin\alpha$$
$$x_B = 60 \qquad y_B = 25$$
$$x_B = 60 \qquad y_B = 43.4$$

The maximum angular rotation α_{max} can be determined by setting the distance between points **A** and **B** to its maximum value:

$$\Delta L_{AB}^{max} = \sqrt{(x_A - x_B)^2 + (y_A - y_B)^2} - 25 = 12.5 \rightarrow \alpha_{max} = 12.00^\circ \tag{F.1}$$

Subsequently the elongations ΔL_{AB} and ΔL_{AC} were determined for the range $\alpha = [0, \alpha_{max}]$. The results are depicted in Fig. F.3. Visually no distinction between the elongations can be made. A closer numerical inspection shows a maximum error of ΔL_{AC} to ΔL_{AB} of 0.06%. Therefore the geometrical error introduced by the modification is neglected.

MODEL 3542 Axial Extensometers

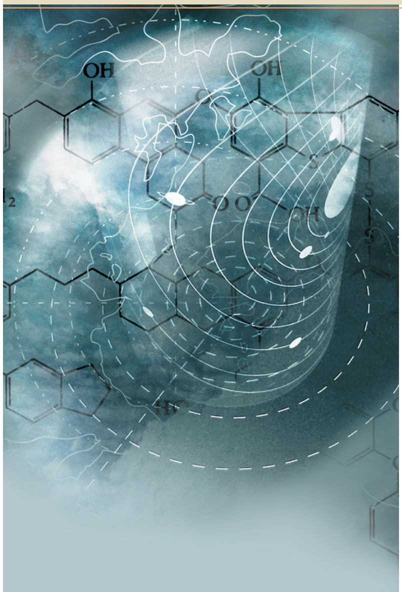

General purpose extensometers for axial tensile, compression, and cyclic testing. Gauge lengths from 10 to 80 mm (and 0.5 to 2 inches) and full scale measuring ranges from 5% to 100% strain.

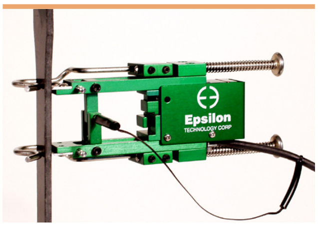

Model 3542 with 25 mm gauge length and ±10% measuring range

These extensometers are designed for testing a wide range of materials, including metals, plastics, composites and ceramics. All will perform both tension and compression strain measurement. The dual flexure design makes them very rugged and insensitive to vibrations, which permits higher frequency operation.

They come standard with Epsilon's quick attach kit, making it possible to mount the extensometer on the test specimen quickly and easily with one hand. The quick attach kit can be removed, allowing mounting of the extensometer with springs or rubber bands.

The Model 3542 extensometers are strain gaged devices, making them compatible with any electronics designed for strain gaged transducers. Most often they are connected to a test machine controller. The signal conditioning electronics for the extensometer is typically included with the test machine controller or may often be added. In this case the extensometer is shipped with the proper connector and wiring to plug directly into the electronics. For systems lacking the required electronics, Epsilon can provide a variety of solutions, allowing the extensometer output to be connected to data acquisition boards, chart recorders or other equipment.

For gauge lengths 100 mm (4 inches) or greater see Model 3542L.

See the electronics section of this catalog for available signal conditioners and strain meters.

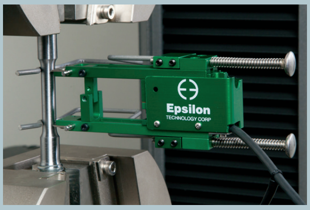

Model 3542 with 25 mm gauge length

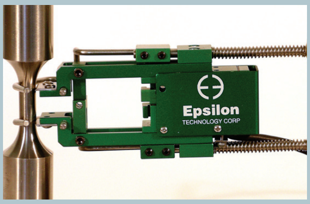

Model 3542 with 0.5 inch gauge length and ±25% measuring range

Model 3542 configured for a very large specimen diameter

▶ See the Model 3542 extensometer videos

Extensometers for Composites Compression Testing

Models 3542 and 3442 extensometers can be furnished to clip directly onto composites compression fixtures, such as for ASTM D695. These use specially made quick attach kit wire forms for the test fixture. Consult the factory for specifics.

Also see the Model 3442 miniature extensometer.

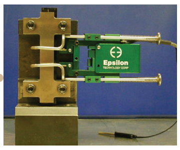

Model 3542 mounted on a D695 compression fixture for composite materials

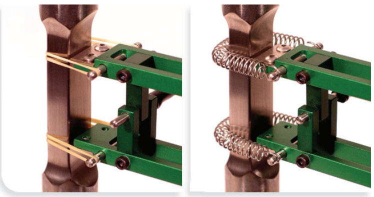

Rubber band and spring attachment options included with Models 3542 and 3442

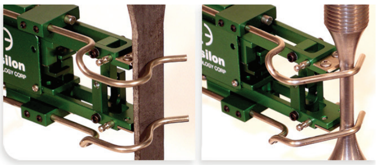

Standard quick attach wire forms included for round and flat samples

Features

- **May be left on through specimen failure.**
- All models can measure in both tension and compression and can be used for cyclic testing.
- Standard quick attach kit allows one hand mounting to specimens.
- Applicable for testing to:
  - ISO 6892-1, 527-2, 527-4, 527-5, 10113
  - ASTM E8, E9, D3039, D638, A370, D3552, E517, E646
- Standard units meet ASTM class B-1 requirements for accuracy. A test certificate is included. ISO 9513 class 0,5 test certificates are available upon request.
- Rugged, dual flexure design for strength and improved performance. Much stronger than single flexure designs, this also allows cyclic testing at higher frequencies.
- All models have mechanical overtravel stops in both directions. Cable stops are used for overtravel protection where required. Epsilon's cable stops are fully contained between the arms of the extensometer and do not hang below where they can interfere with fixturing – especially during compression testing.
- Hardened tool steel knife edges are easily replaced. A spare set comes with every extensometer.
- Replaceable arms and spacers for ease of repair. This also allows changing the gauge length for different test requirements.
- High and low temperature options extend operation from as low as -270 °C to +200 °C (-454 °F to +400 °F).
- Full bridge, 350 ohm strain gaged design for compatibility with nearly any test system.
- Includes high quality foam lined case.

SPECIFICATIONS

Excitation:	5 to 10 VDC recommended, 12 VDC or VAC max.
Output:	2 to 4 mV/V, nominal, depending on model
Linearity:	≤0.15% of full scale measuring range
Temperature Range:	Standard (-ST) is -40 °C to +100 °C (-40 °F to 210 °F) Optional (-LHT) is -270 °C to +200 °C (-454°F to 400 °F)
Cable:	Integral, ultra-flexible cable, 2.5 m (8 ft) standard
Standard Quick Attach Kit:	Fits round samples up to 25 mm diameter (1.0 inch) and flats to 12 mm thick by 31 mm wide (0.5 inch by 1.25 inch)
Operating Force:	30 g typical

OPTIONS

Quick attach kit wire forms for large specimens
Adapter kits to change gauge lengths
Connectors to interface to nearly any brand test equipment
Special coatings and stainless steel knife edges available for biomedical tests
Shunt calibration module (see page 120)
Specialty knife edges (see page 100)

CE CERTIFIED

ORDERING INFORMATION

Model 3542 Available Versions: ANY combination of gauge length, measuring range and temperature range listed below is available, except as noted. *Other configurations may be available with special order; please contact Epsilon to discuss your requirements.*

Gauge Length

METRIC	
-010M	10.0 mm
-012M	12.0 mm
-0125M	12.5 mm
-025M	25.0 mm
-050M	50.0 mm
-080M	80.0 mm
U.S.A.	
-0050	0.500”
-0064	0.640”
-0100	1.000”
-0140	1.400”
-0200	2.000”

Measuring Range[1]

DESIGNATION	% STRAIN
-005[2]	±5%
-010	±10%
-020	+20%/-10%
-025	+25%/-10%
-050	+50%/-10%
-100	+100%/-10%

Model Number 3542- __ __ __ __ - __ __ __ - __ __

Temperature Range

-LT	-270 °C to 100 °C (-454 °F to 210 °F)
-ST	-40 °C to 100 °C (-40 °F to 210 °F)
-HT1	-40 °C to 150 °C (-40 °F to 300 °F)
-HT2	-40 °C to 200 °C (-40 °F to 400 °F)
-LHT	-270 °C to 200 °C (-454 °F to 400 °F)

[1] *Compressive ranges can be adjusted to higher values if required. Please contact Epsilon for your specific testing requirement.*

[2] *Not available in 10 mm, 12.5 mm, or 0.50 inch gauge lengths.*

Example: 3542-0100-020-LT: 1.000 inch gauge length, ±20% measuring range, low temperature option (-454 °F to 210 °F)

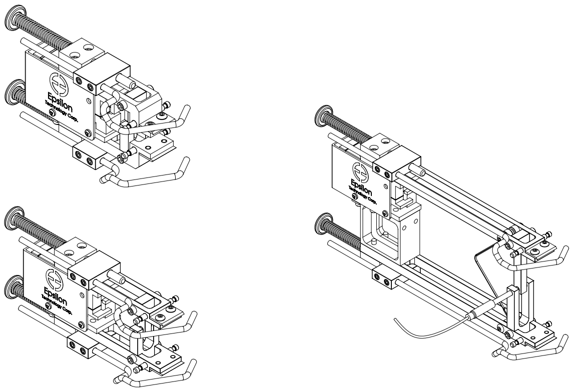

MODEL 3542 EXAMPLES

Appendix G

Erosion Keyword File

In this appendix, an example LS-DYNA input file is presented. The code is generated in MatLab and is interpreted by LS-DYNA as a fracture locus in the space of triaxiality, Lode parameter and equivalent strain to fracture. For the sake of brevity, the presented code holds only five Lode- and nine triaxiality datapoints. By default, the MatLab file uses a grid of 51 by 101 datapoints (Lode by triaxiality). Note that the triaxiality distribution is linear in respect to $\bar{\theta}$ and not to ξ, since the presented failure model (Modified Mohr-Coulomb) uses $\bar{\theta}$, while LS-DYNA requires ξ as Lode parameter input formulation. A linear $\bar{\theta}$-distribution is beneficial, as it ensures a higher grid density towards the boundaries of the ξ-domain where fracture loci are generally steeper. This reduces the interpolation error in LS-DYNA.

```
$# Failure model: Modified Mohr-Coulomb
$# File created on: 14-Aug-2017 13:51:30
$# Calibration parameters:
$# A = 740000000   n = 0.16667   c1 = 0.1   c2 = 330000000   cs = 1   cc = 1   ceta = 0   eta0 = 0   m = 1
*DATABASE_EXTENT_BINARY
$#   neiph     neips    maxint    strflg    sigflg    epsflg    rltflg    engflg
         0         1         3         1         1         1         1         1
$#  cmpflf    ieverp    beamip     dcomp      shge     stssz    n3thdt   ialemat
         0         0         0         1         1         1         1         0
*MAT_ADD_EROSION
$#     mid      excl    mxpres     mneps    effeps    voleps    numfip       ncs
         2         0         0         0         0         0         1         1
$#  mnpres     sigp1     sigvm     mxeps     epssh     sigth   impulse    failtm
         0         0         0         0         0         0         0         0
$#    idam    dmgtyp     lcsdg     ecrit    dmgexp     dcrit    fadexp    lcregd
         1        01      1001         0         1         1         1         0
$#  sizflg     refsz     nahsv     lcsrs    regshr    rgbiax
         0         0         1         0         0         0
$#   lcfld             epsthin    engcrt    radcrt
         0         0         0         0         0
*DEFINE_TABLE
$#    tbid       sfa      offa
      1001         1         0
$#             value      lcid
           -1.000000      1002
           -0.707107      1003
            0.000000      1004
            0.707107      1005
            1.000000      1006
*DEFINE_CURVE
$#    lcid      sidr       sfa       sfo      offa      offo    dattyp     lcint
```

```
      1002         0         1         1         0         0         0         0
$#                a1                  o1
           -0.666667            1.450135
           -0.500000            1.147643
           -0.333333            0.916259
           -0.166667            0.737509
            0.000000            0.598146
            0.166667            0.488557
            0.333333            0.401691
            0.500000            0.332319
            0.666667            0.276529
*DEFINE_CURVE
$#    lcid      sidr       sfa       sfo      offa      offo    dattyp     lcint
      1003         0         1         1         0         0         0         0
$#                a1                  o1
           -0.666667            0.603060
           -0.500000            0.492437
           -0.333333            0.404778
           -0.166667            0.334793
            0.000000            0.278525
            0.166667            0.232986
            0.333333            0.195901
            0.500000            0.165523
            0.666667            0.140501
*DEFINE_CURVE
$#    lcid      sidr       sfa       sfo      offa      offo    dattyp     lcint
      1004         0         1         1         0         0         0         0
$#                a1                  o1
           -0.666667            0.428684
           -0.500000            0.353930
           -0.333333            0.293950
           -0.166667            0.245499
            0.000000            0.206114
            0.166667            0.173906
            0.333333            0.147419
            0.500000            0.125521
            0.666667            0.107326
*DEFINE_CURVE
$#    lcid      sidr       sfa       sfo      offa      offo    dattyp     lcint
      1005         0         1         1         0         0         0         0
$#                a1                  o1
           -0.666667            0.488990
           -0.500000            0.402035
           -0.333333            0.332595
           -0.166667            0.276751
            0.000000            0.231546
            0.166667            0.194725
            0.333333            0.164556
            0.500000            0.139702
            0.666667            0.119119
*DEFINE_CURVE
$#    lcid      sidr       sfa       sfo      offa      offo    dattyp     lcint
      1006         0         1         1         0         0         0         0
$#                a1                  o1
           -0.666667            0.916259
           -0.500000            0.737509
           -0.333333            0.598146
           -0.166667            0.488557
            0.000000            0.401691
            0.166667            0.332319
            0.333333            0.276529
            0.500000            0.231365
            0.666667            0.194577
```

Appendix H

Validation of Implementation

In this part of the appendix the validation procedures for the implementation of the failure models are presented. Implementing a failure model using the keywords discussed in the previous section is quite complicated due to the abundance of options of *MAT_ADD_EROSION. This section is dedicated to describing the procedure that was performed to ensure that the implementation was done correctly.

An LS-DYNA input file, holding the formatted fracture locus data, was created for six different fracture loci:

1. Constant Equivalent Failure Strain (No dependency on triaxiality and Lode)
2. Test model 1 (Linear Lode dependency only)
3. Test model 2 (Linear triaxiality dependency only)
4. Test model 3 (Linear triaxiality and Lode dependency)
5. Modified Mohr-Coulomb (Triaxiality and Lode dependency)
6. Xue model (Triaxiality and Lode dependency)

With this particular set of failure models it was made possible to test either triaxiality or Lode dependence, or neither, or both. In the case of the test models, the dependency on triaxiality and/or Lode is linear. The associated arbitrary calibration parameters ensure positive equivalent fracture strains on the plane stress Lode and triaxiality domain. The test models are given by the following relations.

$$\text{Test model 1:} \qquad \bar{\varepsilon}_f = 0.2 + 0.05\,\bar{\theta} \tag{H.1a}$$

$$\text{Test model 2:} \qquad \bar{\varepsilon}_f = 0.2 - 0.1\,\eta \tag{H.1b}$$

$$\text{Test model 3:} \qquad \bar{\varepsilon}_f = 0.2 + 0.05\,\bar{\theta} - 0.1\,\eta \tag{H.1c}$$

The functions for the actual fracture models are presented in Section 3.1. These were calibrated to for which the calibration parameters are listed in Table H.1.

Table H.1: Calibration parameters

Failure Model	Parameter	Value	Unit
Constant Equivalent Failure Strain	$\bar{\varepsilon}_f$	0.2	-
Modified Mohr-Coulomb	c_1	0.1	-
	c_2	330	MPa
	c_s	1	-
	c_c	1	-
	c_η	0	-
	η_0	0	-
Xue	σ_{f0}	760	MPa
	k_p	$4.2 \cdot 10^{-4}$	MPa^{-1}

Figure H.1 gives a visual representation of the used failure models. Note that states of stress at fracture of the single element deformation cases have been projected on the fracture locus. Therefore the presented fracture points do not represent actual fracture. The actual fracture points are only coincident with the represented fracture points in the case of constant stress path (i.e. constant triaxiality and Lode parameter during deformation).

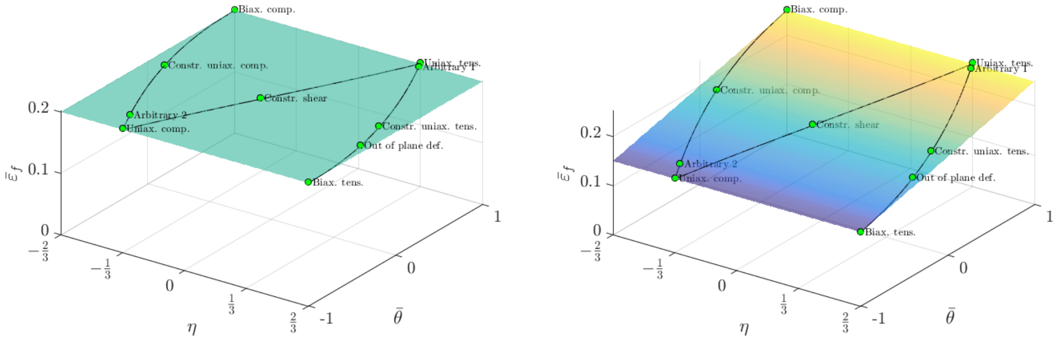

(a) Constant Equivalent Failure Strain

(b) Test model 1

Since the current objective is to validate the implementation, rather than predicting actual fracture, the calibration parameters for the MMC models can freely be chosen.

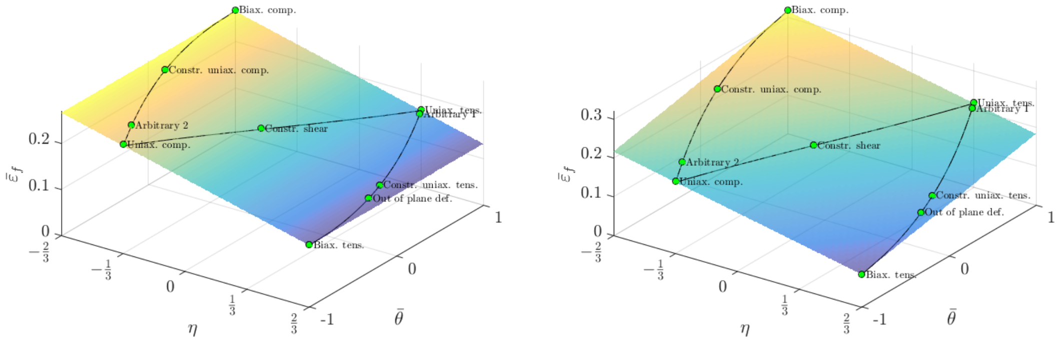

(c) Test model 2

(d) Test model 3

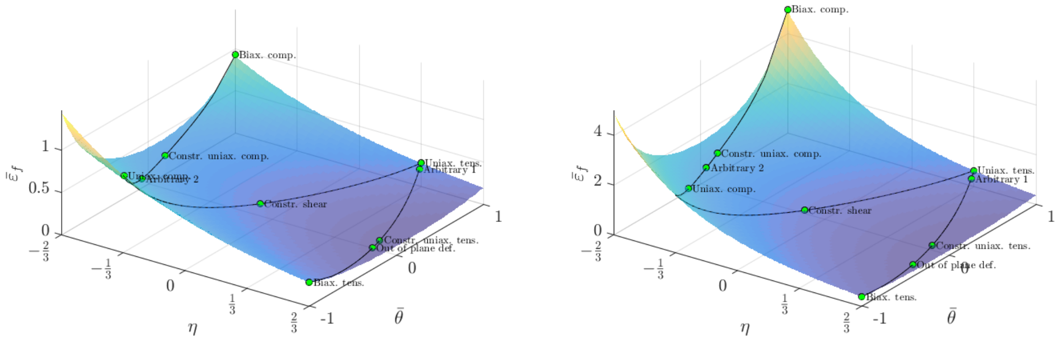

(e) Modified Mohr-Coulomb

(f) Xue model

Figure H.1: Triaxiality & Lode dependent validation fracture loci

The parameter values were obtained from Bai and Wierzbicki [2010], reducing the material model to a power law plasticity model. Therefore no user defined material model is required, thus greatly serving the current objective. The values of the power law parameters are $K = 740$ MPa and $n = 0.167$. The yield point is defined by the intersection of the power law and the linear elastic relation with a Young's Modulus $E = 207$ GPa.

Several different sets of prescribed displacements and boundary conditions were applied to the nodes of a single shell element. These sets were composed with the intend to study the behaviour of the implemented failure model for different combinations of triaxiality. The Lode parameter is dependent on the stress triaxiality due to the shell element's inherent plane stress assumption. The nodal displacements in the different deformation sets are all linearly increasing in time. The relative magnitudes of displacement are presented in Table H.2 and the resulting deformations are depicted in

Fig. H.2. To each node displacement factors are applied, these are listed in the rightmost three columns of the table. An entry equal to one therefore indicates a motion in the positive direction of the associated degree of freedom. A negative entry indicates a nodal displacement in the opposite direction. A factor of zero constrains the node to its initial position. The absence of a displacement factor means a non-prescribed displacement and therefore results in free motion of the node in the associated degree of freedom.

The shell element dimensions were arbitrarily chosen as they are of no influence on the failure models' behaviour. The square 4-noded shell element lies in the xy-plane with sides of length 20 and a thickness of 1. Five integration points are located through thickness at the center of the element. Element deletion occurs if the critical value of the damage parameter is exceeded in three or more integration points.

From LS-DYNA the time-traces of the equivalent plastic strain, the principal stresses, and the damage variable were extracted. Evidently, the strains and stresses are independent of the failure model. The triaxiality and Lode parameter were determined from the extracted principal stresses, and used as input in the continuous failure model function in MATLAB to determine the equivalent fracture strain (EFS). Subsequently the damage time-trace was computed using the EFS and the EPS. Ultimately, the calculated damage was compared to the damage output variable from LS-DYNA. This process is depicted in Fig. H.3.

The maximum error between the two damages has been obtained for all prescribed deformations and all failure models listed above. The results are presented in Fig. H.4a.

An important remark on the results in Fig. H.4 is that the damage difference always increases in time, and therefore has a maximum just before element deletion occurs, i.e. just before the damage variable reaches its critical value of one.

The maximum damage difference of all deformation cases and failure models is approximately 1%, while the bulk of the results is far lower. The errors for the CEFS-model are of the smallest magnitude and close to identical. However, for the other models, which do account for stress path dependent failure strain, no clear relation between the deformation cases and the associated damage differences exists. Introducing Lode and/or triaxiality dependency enlarges the error. Further increasing the grid density is of negligible effect. Therefore it is stated that a slight discrepancy exists between the damage calculations done in LS-DYNA and those presented in this report. Due to the small effect on the results of this discrepancy, it is concluded that the failure models in the form of $\bar{\varepsilon}_f(\eta,\theta)$ were properly implemented in LS-DYNA using the keyword *MAT_ADD_EROSION.

Table H.2: Single element deformations

Deformation case	node	Degree of freedom		
		x	y	z
Uniaxial tension	1	0		0
	2	1		0
	3	0		0
	4	1		0
Constrained uniaxial tension	1	0	0	0
	2	1	0	0
	3	0	0	0
	4	1	0	0
Constrained shear	1	0	0	0
	2	0	-1	0
	3	0	0	0
	4	0	-1	0
Uniaxial compression	1		0	0
	2		0	0
	3		1	0
	4		1	0
Constrained uniaxial compression	1	0	0	0
	2	0	0	0
	3	0	1	0
	4	0	1	0
Out of plane deformation	1	0	0	0
	2	0	0	1
	3	0	0	0
	4	1	0	-1
Biaxial tension	1	0	0	0
	2	1	0	0
	3	0	-1	0
	4	1	-1	0
Biaxial compression	1	0	0	0
	2	-1	0	0
	3	0	1	0
	4	-1	1	0
Arbitrary deformation 1	1	0	0	0
	2	1	1	0
	3	0	-1	0
	4			0
Arbitrary deformation 2	1	0	0	0
	2	0	0	0
	3	-1	0	0
	4	-1	1	0

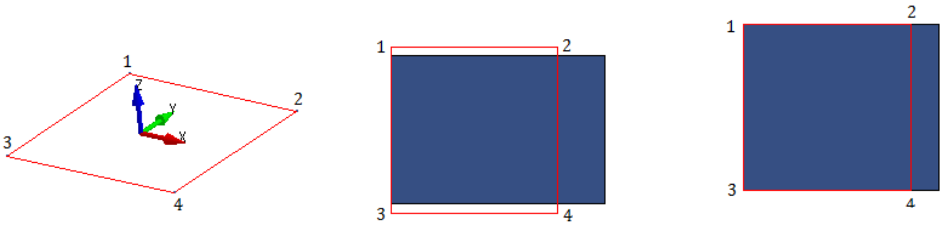

(a) Initial oriëntation (b) Uniaxial tension (c) Constrained uniaxial tension

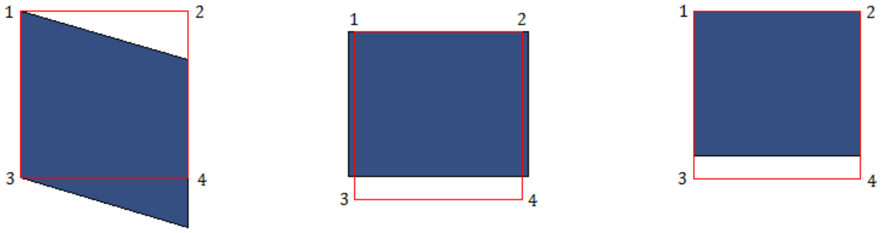

(d) Constrained shear (e) Uniaxial compression (f) Constr. uniaxial compression

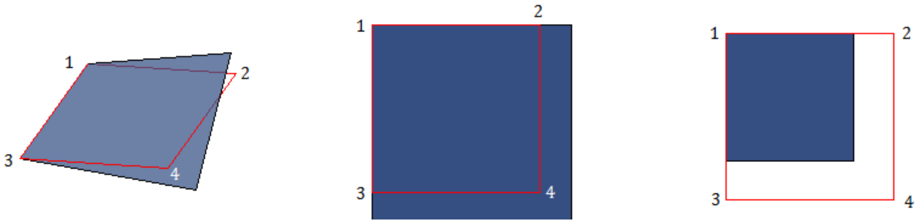

(g) Out of plane deformation (h) Biaxial tension (i) Biaxial compression

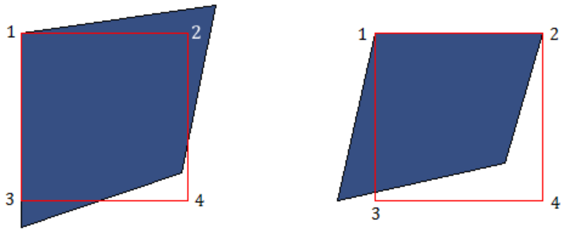

(j) Arbitrary deformation 1 (k) Arbitrary deformation 2

Figure H.2: Single element deformations

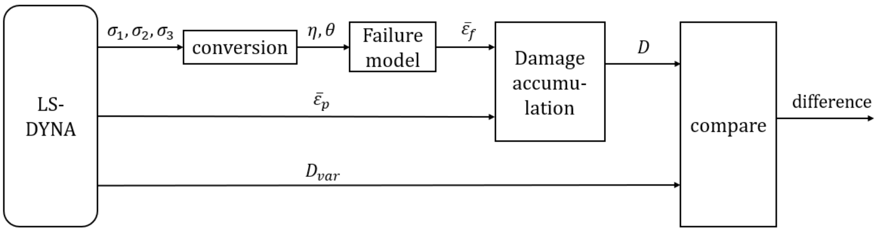

Figure H.3: Damage difference (error) calculation flowchart

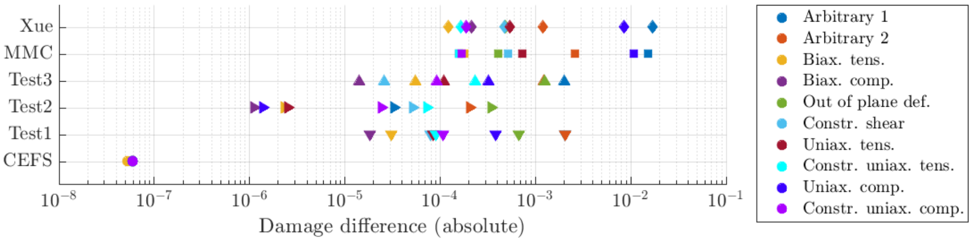

(a) Per failure model

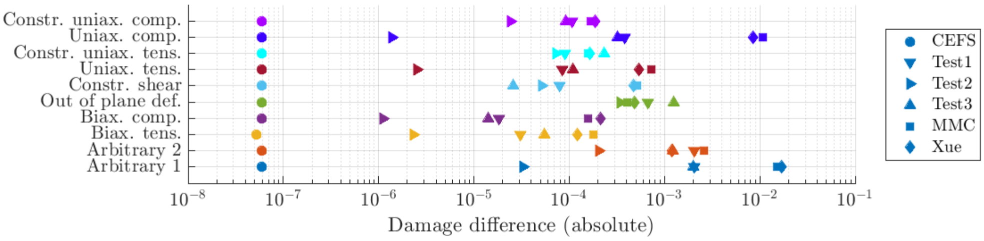

(b) Per prescribed deformation

Figure H.4: Maximum difference between calculated damage and damage output variable for triaxiality and Lode dependent models

Appendix I

Validation of Calibration Procedure

The implementation of the Variable Load Path Calibration procedure as described in Chapter 5 required validation. The procedure of this validation is herein presented.

First, a fracture locus defined by a set of calibration parameters was assumed (Fig. I.1a) and data sets of fictitious experiments are generated: These data represent time traces of equivalent plastic strain, triaxiality and Lode parameter. The EPS trace starts from zero and increases linearly. Both the triaxiality and Lode parameter traces are generated by selecting a shape function randomly from a set of four. The starting and ending values of their traces are randomly generated on a certain domain. For triaxiality this domain is $[\frac{1}{3},\frac{2}{3}]$. The full Lode parameter domain has been used. Four different time traces have been depicted in Fig. I.1b.

Subsequently the time traces have been truncated to the point where fracture is predicted. This point is determined using damage accumulation and are indicated by red stars in Fig. I.1c. The next step is to omit the original fracture locus that was used to truncate the traces (Fig. I.1d). The obtained fictitious data is inserted into the damage calculation of the VLPC procedure (Eq. 5.7) and the system of equations (Eq. 5.8) is minimized to find the calibrated fracture locus (Fig. I.1f).

Ideally, the obtained calibration parameters are equal to those associated with the originally assumed fracture locus. However, uncertainty is introduced by the randomized load paths and the discrete nature of the traces causes a slight numerical error. The latter can be restricted by ensuring sufficient datapoints in the load path histories obtained from FEA. The calibration parameters associated with the originally assumed fracture loci are presented in Table I.1 and are used throughout this section.

The least squares approach that is used to obtain the calibrated fracture locus requires an initial guess of the calibration parameters. The influence of the initial guess on the calibrated parameters is discussed in Section I. The domain where the initial guess should be chosen to obtain proper results is established in Section I.

Table I.1: Original calibration parameter values

Failure Model	Parameter	Value	Unit
Xue	σ_{f0}	640	MPa
	k_p	$4.2 \cdot 10^{-4}$	MPa^{-1}
Modified Mohr-Coulomb	c_1	0.1	-
	c_2	330	MPa
Hosford-Coulomb	a	1.4	-
	b	650	MPa
	c	0.1	-

Accuracy

To study the effect of the VLPC procedure on the obtained calibration parameters, a comparison is made between the originally assumed locus and the calibrated locus. To this goal, the height of both the original and the calibrated fracture locus is evaluated at 25 locations across the domain, evenly spaced in a five-by-five grid (Fig. I.2). Subsequently, the normalized root mean square error of these data points is computed according to Eq. I.1.

$$\mathrm{RMSE} = \sqrt{\frac{1}{N_p}\sum_{i=1}^{N_p}\left(\frac{Y_i^{\mathrm{cal}}}{Y_i^{\mathrm{ini}}} - 1\right)^2} \tag{I.1}$$

Where Y^{ini} and Y^{cal} are the arrays of datapoints on respectively the original and the calibrated locus. The constant N_p is the length of these arrays and is therefore equal to 25. The accuracy of the VLPC is characterized by the probability distribution of the RMSE. This distribution has been depicted for the case where the initial guess is equal to the original calibration parameters in Fig. I.3a and for an arbitrary initial guess in Fig. I.3b. The distributions were obtained from the results of one thousand samples per number of experiments. In other words: The RMSE is computed for thousand sets of N_{exp} fictitious experiments. This was repeated for all numbers of experiments and for all fracture models.

Barely any distinction can be made between the results from using arbitrary initial values and using the original parameters as initial values. The least squares approach converges to the same points, irrespective of the initial values. This suggests the absence of local minima, but will be studied more extensively in the subsequent section. A worse initial guess results in an increase in required iterations until a minimum is found and therefore slightly increases the computational time.

Although the fracture models are inherently different, their fracture loci are similar to the degree that the RMSE's are also barely influenced by a properly chosen initial guess. The results for the remaining fracture models using the original calibration parameters as initial values are presented in Fig. I.4. Results similar to Figs. I.3a & I.3b are readily obtained when properly chosen arbitrary initial values are used.

For computational purposes, the iterative step size tolerances for the least squares approach have been set to a sufficiently small, yet finite value. Setting these tolerances to zero might further decrease the RMSE, but is not feasible for the current goal of validation. For the calibration on experiments the tolerances are set to zero.

A clear trend can be observed from the amount of experiments that were used to calibrate on: Increasing the amount of experiments generally results in a higher accuracy of the calibrated fracture locus, i.e. the probability of exceeding error x converges to zero faster. This is attributed to the random nature of the fictitious experiments. Each experiment yields a damage function f_i (Eq. 5.8), a theoretical solution of $f_i = 0$ exists in a N-dimensional shape, where N is the amount of calibration parameters of the associated failure model. Thus $f_i = 0$ yields a line for models holding two calibration parameters, or a surface for three calibration parameter models. The least squares approach attempts to find the minimum distance between these N-dimensional shapes. A slight numerical error is introduced in these shapes by the discrete nature of the randomly generated traces. The obtained calibration parameters are affected more by this numerical error if the generated experiments are similar to each other. Over-determination of the system of equations $f_i = 0$ reduces the probability of similarity and therefore reduces the effect of the numerical error on the RMSE.

Robustness

In this section, the effect of the initial guess on the calibrated parameters is studied. A domain study of the initial guess is performed to obtain a guideline for the selection of the initial parameters. The robustness of the VLPC procedure is defined by the size of the domain: The procedure is deemed to be very robust if the initial guess is of little influence on the obtained calibration parameters.

In the previous section it has been discussed that a properly chosen initial guess has barely any effect on the calibrated parameters if the damage functions from the experiments sufficiently differ from each other. Now one set of sufficiently different fictitious experiments has been created to determine how much the initial guess may deviate from the original parameters. This set contains four experiments with constant triaxiality and Lode parameter, arbitrarily chosen across the domain (Fig. I.5). The point of fracture is therefore coincident with the original fracture locus. These four experiments yield four sufficiently different damage functions. The least squares approach was used to obtain the calibrated parameters while varying the initial guess. The RMSE was then computed analogous to the previous chapter. If the RMSE is smaller than 0.01 the calibration is deemed successful.

Two calibration parameter models

The Xue and MMC models depend on two calibration parameters. The *initial guess domain for successful calibration* is numerically determined and indicated in green in Fig. I.6 for both models. The initial guess is normalized using the original fracture locus parameters according to Eq. I.2.

$$X_C = \log_{10}\left(\frac{C}{C^{\text{orig}}}\right) \tag{I.2}$$

Where C indicates any calibration parameter and the subscript ”orig” indicates the originally assumed locus parameters. A value of $X_C = 0$ therefore means that the initial calibration parameter is equal to the value in Table I.1. For the two-parameter models the initial guess was varied between one thousandth of the original values to thousand times the original value, i.e. $-3 < X_C < 3$.

For both models, the domain of successful calibration covers most of the tested initial guess range. In some cases of very poor initial guesses, calibration is unsuccessful. To understand why this is the case, it is important to realize that the least squares approach makes use of the derivatives of the damage functions to the calibration parameters in the form of a Jacobian matrix. For the poor initial guesses associated with unsuccessful calibration, the damage functions D_i are close to zero and their derivatives are smaller than the numerical precision of MATLAB. As a result, the least squares approach identifies the initial guess as a local minimum.

Towards the opposite side of the initial guess spectrum, the damage functions increase exponentially. This results in finite non-zero derivatives and therefore a local minimum can be found by the least squares approach. Very poor initial guesses beyond the tested domain result in the damage function derivatives above numerical infinity, which also results in unsuccessful calibration.

Using a resolution of $\Delta X_C = 0.1$ for both the Xue and MMC model, no indication of the presence of local minima on the tested domain exists. Therefore the domain of successful calibration is deemed to be continuous.

The tested range for the initial guess is exorbitantly large and stretches far beyond realistic values for the calibrations parameters. The VLPC procedure is successful for any $|X_C| \leq 1$. For example, in the case of $X_{\bar{\sigma}_{f0}}$ or X_{c_2} equal to one, the predicted failure strain would never exceed 0.01, which is highly unrealistic for any ductile material. Moreover, values of $X_{c_1} > 1$ also result in unrealistically low strains at fracture. For $X_{k_p} > 1$ the predicted equivalent fracture strains in a biaxial stress state are negative, which is obviously not physically possible.

Three calibration parameter models

For the Hosford-Coulomb fracture model, which holds three calibration parameters, a similar approach is used. However, this requires adding a third dimension to the initial guess domain of successful calibration. Since this requires more computational resources, the tested ranges for the calibration parameters have been narrowed. The domain now spans a volume and is depicted in Fig. I.7a. This unclear representation is however less suitable to yield any decisive information about the initial guess. To overcome this problem, a cuboid inside of the volume is sought for, which represents the domain of successful calibration. This is achieved by arbitrarily varying the boundary planes of the cuboid while two conditions are taken into consideration:

1. All combinations of initial guess parameters inside the cuboid must result in successful calibration.
2. The opposite cuboid boundaries must be sufficiently distant to each other.

The obtained cuboid is defined by the boundaries as presented in Table I.2 and its vertices are indicated by the black lines in Fig. I.7. In each of the two-dimensional subfigures (Figs. I.7b, I.7c & I.7d) the amount of successful calibrations between the boundaries in the third direction is depicted. The dark and even color inside the cuboid indicate the absence of inadequate initial guesses within the domain. Closer numerical inspection also shows no evidence of unsuccessful calibration within this cuboid.

Table I.2: Hosford-Coulomb initial guess domain

	Lower limit	Upper limit
X_a	-1.2	0.1
X_b	-2	0.4
X_c	-2	0.6

The effect of the initial guess of X_b and X_c on the success of calibration is similar to two-parameter models: High values cause the damage functions D_i and their derivatives to approach zero, resulting in the dysfunctionality of the least squares approach. On the other hand, the damage functions show exponential behaviour towards the lower initial values of the two parameters, resulting in the least squares approach being able to find the global minimum. Similar behaviour is observed for the parameter a, but the Hosford-Coulomb shape function is more sensitive and therefore the upper and lower bounds of X_a are closer to zero: Low values of a result in extremely low predicted fracture strains, and therefore the damage functions approach numerical infinity faster than for the other models, therefore the lower bound of X_a is relatively high. Oppositely, for moderately high values of a the derivative of the damage functions to a becomes smaller than the numerical precision faster than for the other parameters.

Observations

Generally, the RMSE between the calibrated and original fracture loci is small for properly chosen initial values. This indicates that the VLPC procedure has been implemented correctly. However, it was assumed that the true fracture locus can be represented by the shape functions of the failure models. In reality this is obviously not true since the failure models differ from each other and are mainly approximations based on observations. Therefore no statement can yet be made on the performance of the VLPC procedure using real experiments.

The experiments used to calibrate the fracture loci should be properly chosen. Similarity between experiments results in similar damage functions, and therefore the least squares approach may yield poor results in terms of calibration parameters. The VLPC procedure benefits from over-determination of the system of equations by using more experiments than calibration parameters.

The domain on which the initial guess of the calibration parameters should be chosen is large. Especially for two-parameter models, the domain of successful calibration greatly exceeds any realistic parameter values. Selecting an initial guess for the three-parameter model requires more carefulness as it is less robust. However, it still holds that any realistic initial values will most likely result in a successful calibration. Slight underestimation of the initial guess is generally beneficial since, for all parameters, the domain of successful calibration reaches further for $X_C < 0$ than for $X_C > 0$. Based on the results from the previous section and the notion of realistic values, suggested initial guess boundaries were created and presented in Table I.3. In this table the boundaries that were determined from the domain study are indicated by a gray asterisk. The remaining values are established by a conservative estimate of realistic values: values beyond these limits result in predicted equivalent plastic strains at fracture either larger than 10 [-] or smaller than 0.01 [-].

Table I.3: Proposed initial guess domain

Failure Model	Parameter	Lower limit	Upper limit	Unit
Xue	σ_{f0}	350	1500	MPa
	k_p	$4.2 \cdot 10^{-6}$ *	10^{-3}	MPa^{-1}
Modified Mohr-Coulomb	c_1	10^{-4} *	0.2	-
	c_2	150	600	MPa
Hosford-Coulomb	a	0.3	1.76 *	-
	b	100	1500	MPa
	c	10^{-3} *	0.2	-

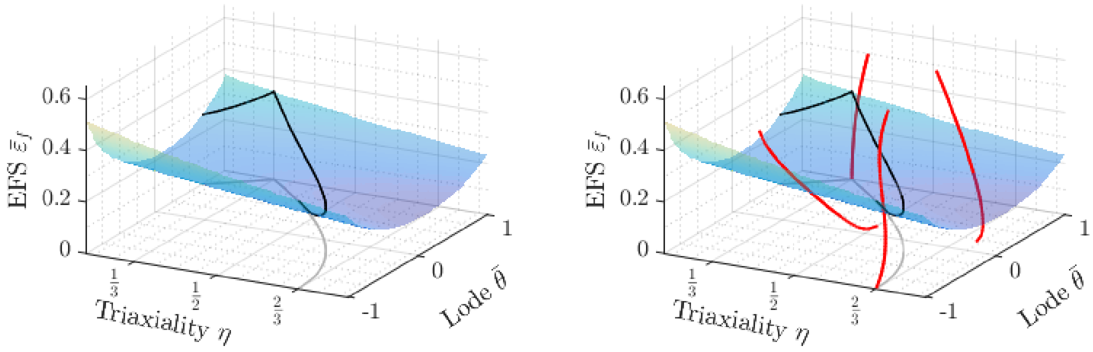

(a) Assumed fracture locus

(b) Randomly generated traces

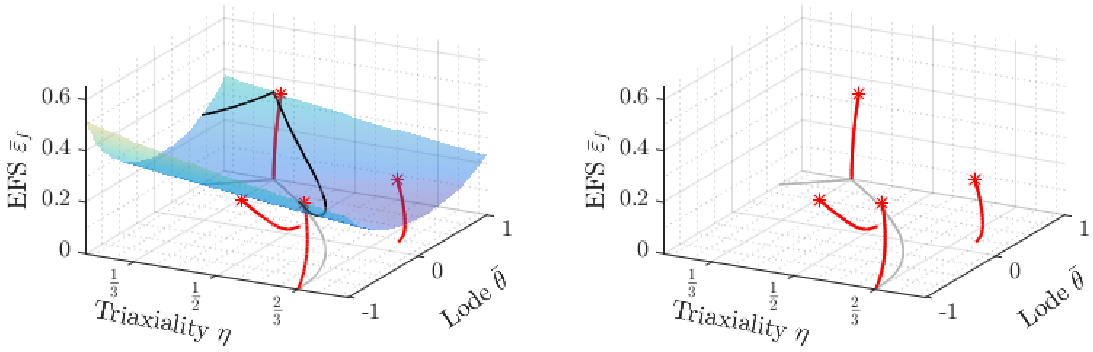

(c) Truncated traces

(d) Omission of initial locus

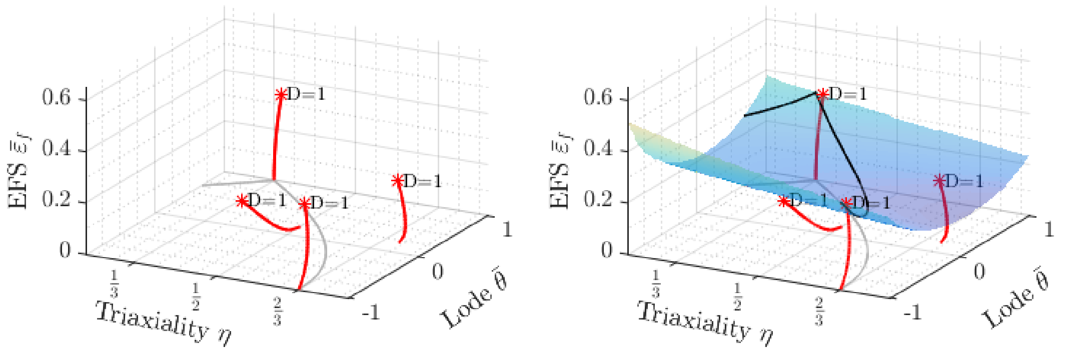

(e) VLPC procedure

(f) Calibrated locus

Figure I.1: Validation procedure for triaxiality & Lode dependent failure model calibration

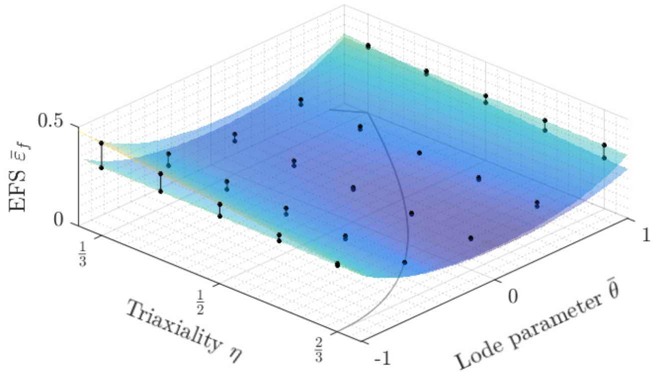

Figure I.2: Example comparison of initially assumed locus and calibrated locus. The root mean square is evaluated using the 25 sets of vertically aligned dots.

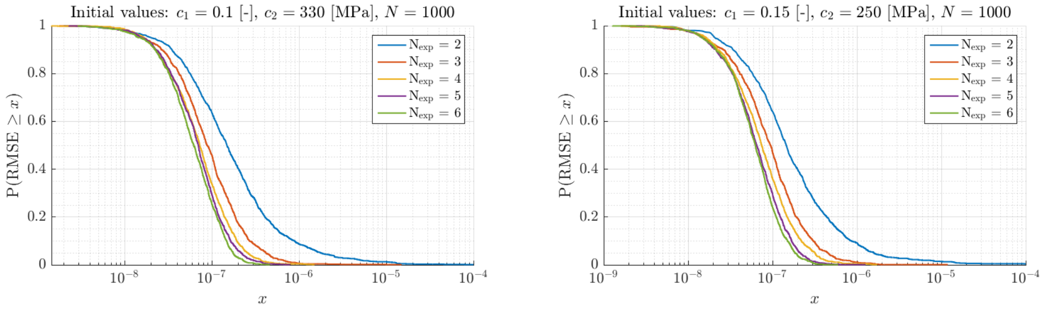

(a) Original calibration parameters

(b) Arbitrary initial guess

Figure I.3: Modified-Mohr Coulomb RMSE probability distributions

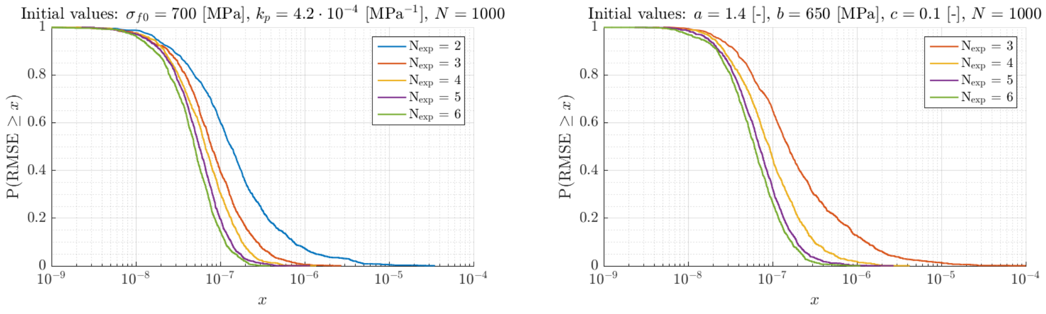

(a) Xue

(b) Hosford-Coulomb

Figure I.4: RMSE distributions

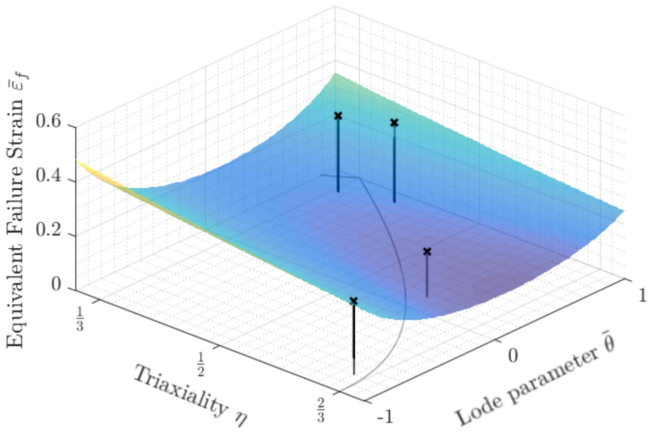

Figure I.5: Fixed arbitrary experiments used to determine the robustness

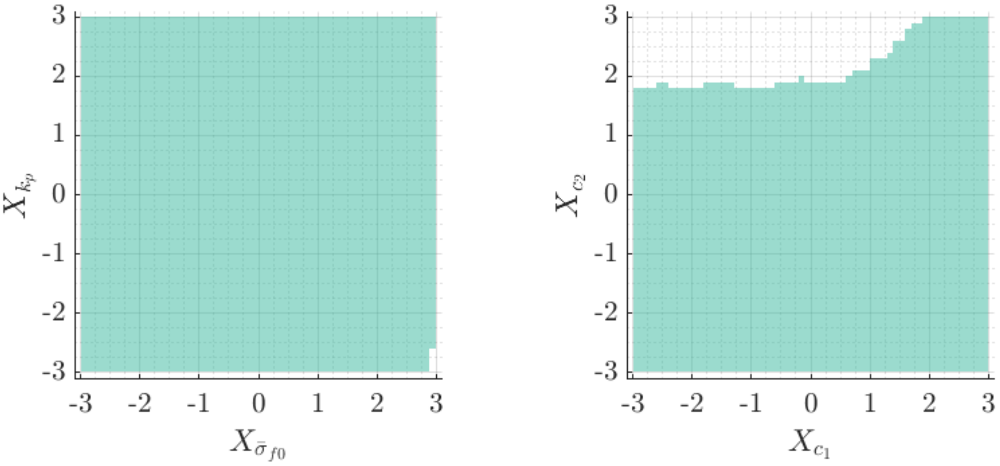

(a) Xue

(b) Modified Mohr-Coulomb

Figure I.6: Two parameter initial guess domain

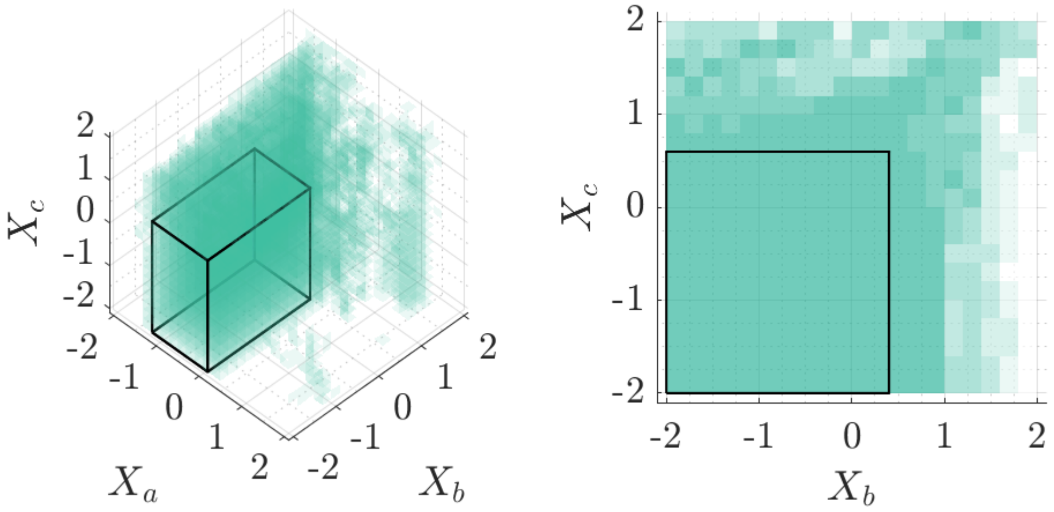

(a) Overview

(b) X_a-direction

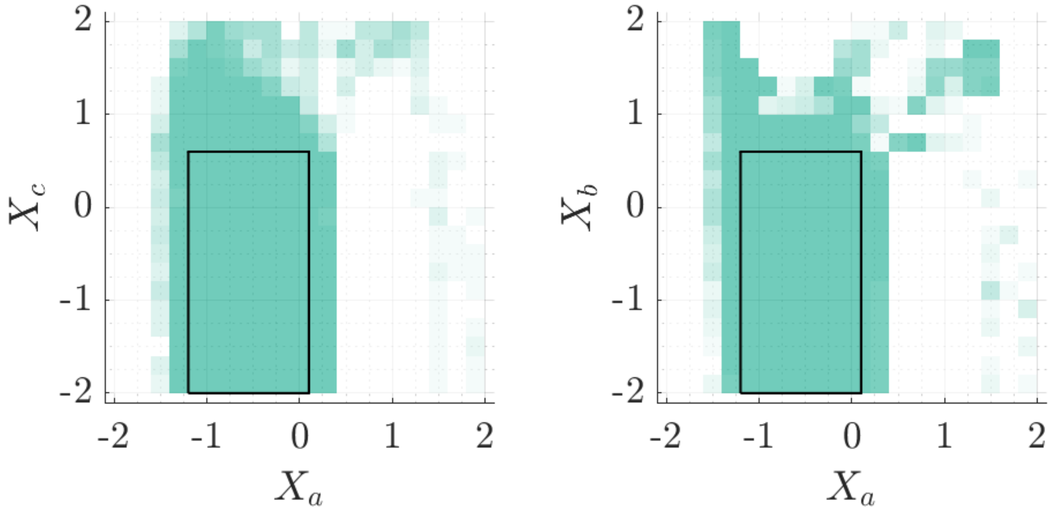

(c) X_b-direction

(d) X_c-direction

Figure I.7: Hosford-Coulomb initial guess domain

Appendix J

Raking Damage Experiment Parts

The CAD drawings of the important parts of raking damage experimental setup are presented in this part of the appendix for reference. The dimensions presented in these drawing were used in the creation of the finite element model of the drop tower experiment.

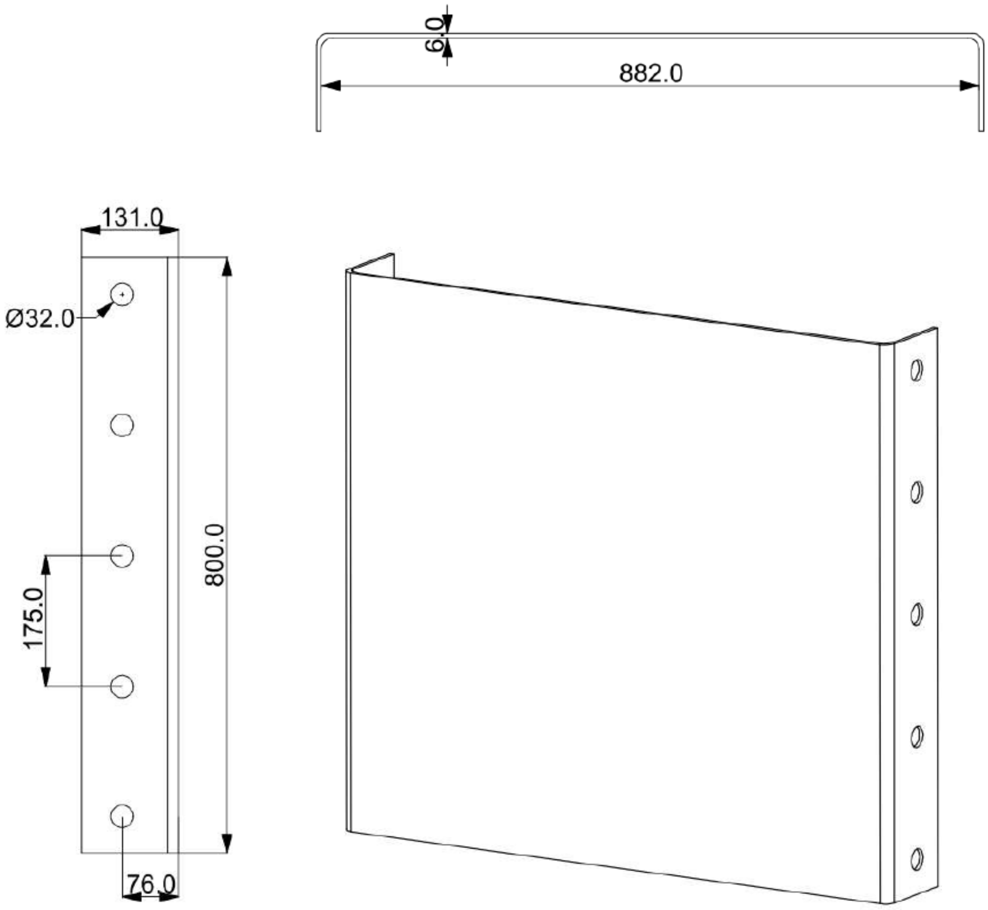

Figure J.1: Plate specimen geometry

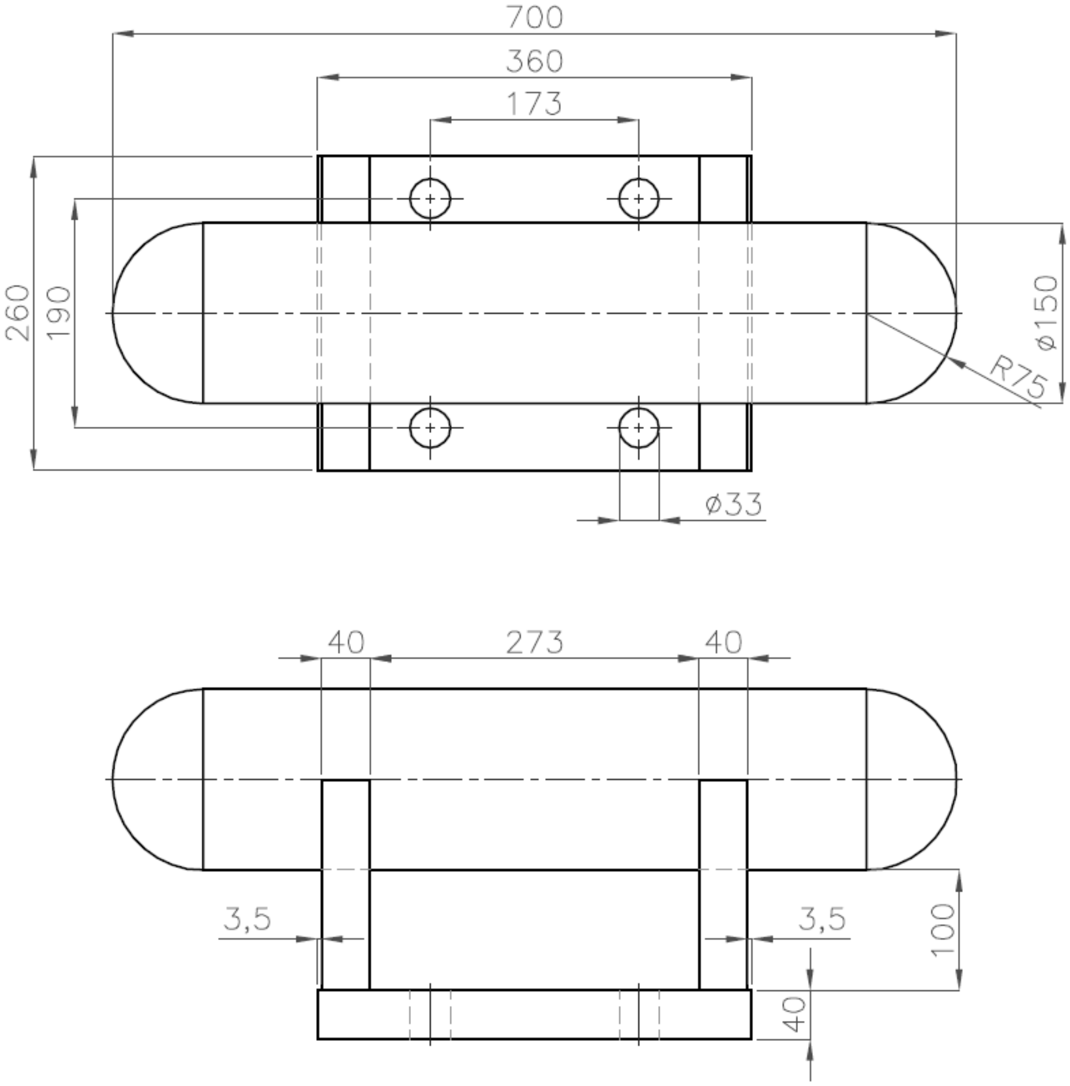

Figure J.2: Indenter geometry

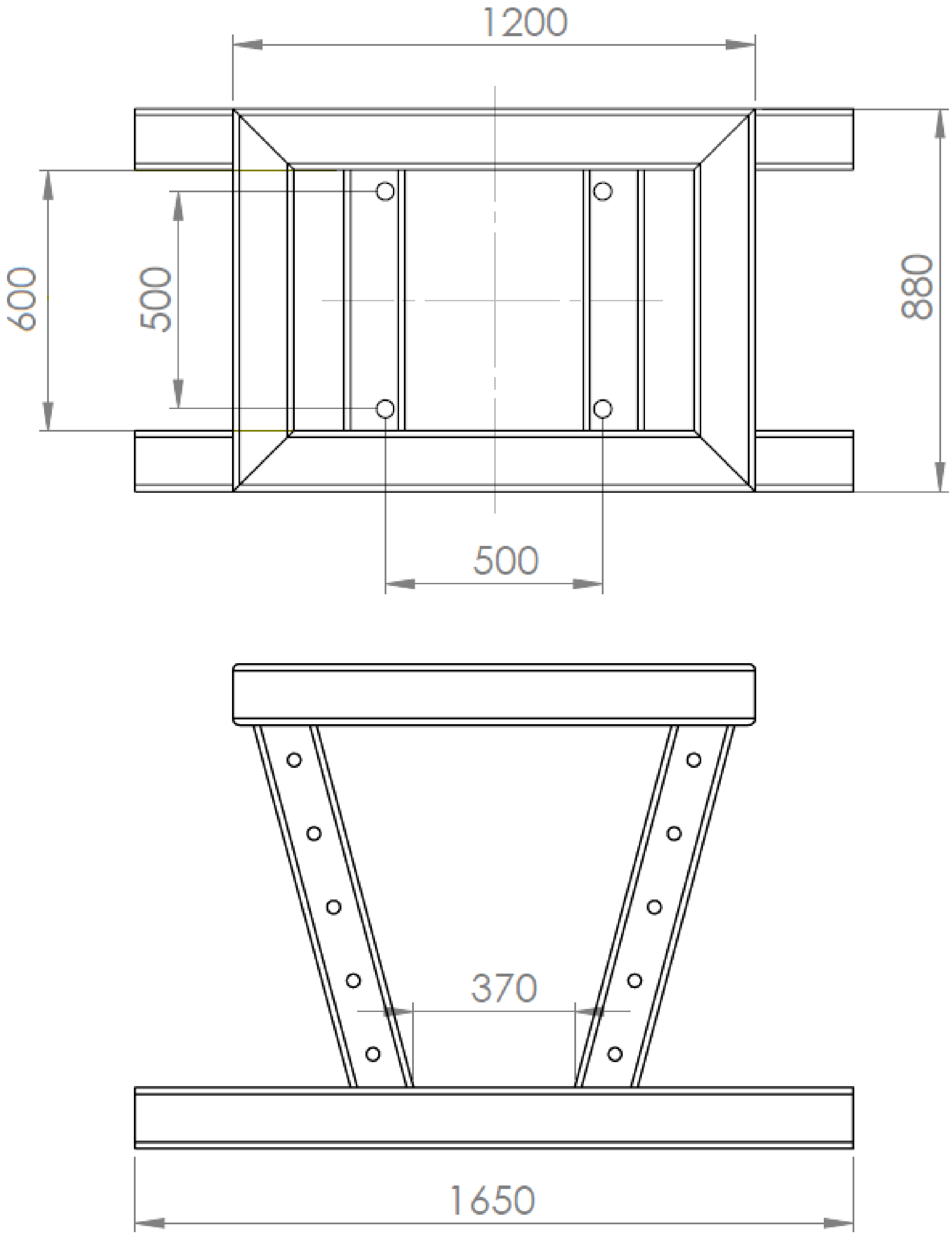

Figure J.3: Frame geometry